708 | April 2018

SCHRIFTENREIHE SCHIFFBAU

Anne Christine Marie Gerdes

Fluid Dynamic Optimization of HVAC-Components with Adjoint Methods

TUHH
Technische Universität Hamburg

Fluid Dynamic Optimization of HVAC-Components with Adjoint Methods

Vom Promotionsausschuss der
Technischen Universität Hamburg-Harburg
zur Erlangung des akademischen Grades
Doktor-Ingenieurin (Dr.-Ing.)

genehmigte Dissertation

von
Anne Christine Marie Gerdes

aus
Bremerhaven

2018

Vorsitzender des Prüfungsausschusses
Prof. Dr.-Ing. Gerhard Schmitz

Gutachter
Prof. Dr.-Ing. Thomas Rung
Prof. Dr. rer. nat. Michael Hinze

Tag der mündlichen Prüfung
22. Februar 2018

Fluid Dynamic Optimization of HVAC-Components with Adjoint Methods, Anne Christine Marie Gerdes, 1. Auflage, Hamburg, Technische Universität Hamburg, 2018, ISBN 978-3-89220-708-5

Schriftenreihe Schiffbau
Am Schwarzenberg – Campus 4
D-21073 Hamburg

http://www.tuhh.de/vss

Abstract

The theory and application of continuous adjoint methods for the optimization of heating, ventilation and air-conditioning components is surveyed in this thesis. The cost functions to be optimized are related to comfort and efficiency criteria. Shape and porosity modifications are the means of control, in a CFD-based framework. The underlying physics are the incompressible, steady state Reynolds-averaged Navier-Stokes-Fourier equations. Porosity is modeled by a Darcy term. Using the adjoint method, the sensitivity is computed from the numerical solution of the primal and adjoint equation systems. The cost of the computation is independent of the number of degrees of freedom which makes the method attractive for the application to complex industrial settings.

Of particular note are some specific problems related to the adjoint optimization. An essential aspect is the computation of the gradient from the sensitivity. The sensitivity is a directional derivative and for this reason not feasible for the gradient-based optimization strategy. Therefore, the gradient is computed from the Laplace-Beltrami equation, demanding the numerical solution of an additional partial differential equation of second order on the surface of the geometry. Subsequently, it is used for the design update using gradient descent in conjunction with a proper step size. The computation of the step size for the gradient method is a crucial point. It should unify efficiency *and* feasibility. But, established methods such as line-search based on the Armijo-rule are rather computationally expensive. Hence, a reduced Armijo approach is presented where part of the algorithm is outsourced to a coarse mesh, making the computation less expensive. Using this approach, the intensity of design modification per update step is increased and thus, the whole design cycle accelerated. However, design modifications are often limited by constraints essential for the industrial realization. Accordingly, constraints related to the porosity modification are investigated. The insertion of an approximated regularization term into the cost functional promotes a sparse distributed control which is in some cases preferred.

The approaches are implemented and validated by fluid dynamic test cases. The arising framework is applied to heating, ventilation and air-conditioning components. It is shown that the adjoint method is a powerful and efficient technique to optimize heating, ventilation and air-conditioning components. However, the application to industrial cases often requires adaptations necessary for the individual requirements, making know-how and manual adjustments by the user irremissible. Therefore, future developments in the automation of the process chain offer room for improvement.

Acknowledgements

First of all I deeply acknowledge my supervisors Prof. Thomas Rung and Prof. Michael Hinze for giving me the opportunity to do my doctoral degree in Hamburg. The discussions, influenced by engineering and mathematical points of view, were always constructive and helpful. Furthermore, I thank Prof. Gerhard Schmitz for kindly chairing the examination board.

Several people from university and industry inspired my work. I thank Carsten Othmer from Volkswagen for his support in the numerical computations when I started and for his prompt and competent answers to my questions. My gratitude goes to Jan Philipp Heners, whose student projects at the university gave me a lot of input, especially concerning the numerical solution of the Laplace-Beltrami equation. I thank my former colleague Christian Kahle for his honest interest in my work and valuable input.

I gratefully acknowledge the funding received from the German Ministry of Economy and Technology (BMWi) in the project PROTEG under the aegis of LUFO4 framework program. This project offered me the chance to directly apply the numerical developments to industrial applications. In this context my gratitude goes to Claus Wagner and Gerrit Lauenroth from German Aerospace Center (DLR) Göttingen for the collaboration on a joint article, connecting their experimental measurements with my numerical computations.

Funding received from the Lothar Collatz School for Computing in Science is gratefully acknowledged. Furthermore, I thankfully appreciate the opportunity to work at Universität Hamburg as a research associate.

I thank my colleagues from Hamburg University of Technology and Universität Hamburg for the pleasant working atmosphere. Particularly, my thanks goes to Maria Gaschler and Marzia Leonardi, with whom I shared good and challenging phases of the doctoral studies. I thank Daria Jakubek for the great time we had when she visited Hamburg for research.

I thank my friends for their support beyond the work, which helped me to relax and recover. Finally, my deep gratitude goes to my family. My parents for making my studies possible. My son Till for enriching my life and our future family member, who – if all goes well – will be born in May, for being there. I thank my husband Sebastian, on whom I can always count, for motivating me to go on. Without this unconditional support I would hardly have finished.

Contents

Glossary

Lower-case Roman

a_1	constant in SST $k-\omega$ model
c_p	specific heat capacity
c_v	isochore heat capacity
d	descent direction
$e(y, \mathfrak{u})$	state equation
e	relative error
f	face
f_i	body force
g_i	acceleration of gravity
g_0	standard acceleration due to gravity
j_Γ	boundary-declared cost functional integrand
j_Ω	volume-declared cost functional integrand
k	turbulent kinetic energy
k_f	permeability constant
l	reference length
ℓ	mixing length
m	matrix coefficient
$\dot{m}_f$	mass flux
n	outward normal direction
n_i	outward pointing normal vector
$\underline{o}_n$	vector for orthogonal part of diffusion discretization
$\underline{o}_t$	vector for non-orthogonal part of diffusion discretization
p	primal modified mean pressure
p_*	primal pressure
$\hat{p}$	adjoint pressure
$\mathfrak{p}$	adjoint state
q_i	heat flux density
q^w	wall heat flux
r	radius

u	velocity compontent tangential to the wall
u_i	primal velocity
$\hat{u}_i$	adjoint velocity
u_B	bulk velocity
$\mathfrak{u}$	control
x_i	Cartesian coordinate vector
y	wall distance
y^+	dimensionless wall distance
$\mathfrak{y}$	state
$\tilde{u}_i$	preliminary velocity
u_τ	friction velocity
$\rho\overline{u_i' u_j'}$	Reynolds stress tensor

Upper-case Roman

A	area
$A_i{}^{(f)}$	face area vector
$\mathcal{C}^k$	space of k-times continuously differentiable functions
C_p	pressure coefficient
C_μ	constant in turbulence model
E	embedding function
$\mathtt{E}$	constant in law of the wall
$\mathcal{E}$	internal energy
F_i	flux of momentum
$F_i{}^c$	convective flux
$F_i{}^d$	diffusive flux
$F_i{}^p$	pressure induced flux
F^q	heat flux
F_1	first blending function in SST $k-\omega$ model
F_2	second blending function in SST $k-\omega$ model
$\mathcal{F}$	function space
G	gradient of the control
G_L	surface sensitivity
Gr	Grashof number
H	residual internal energy equation
H^p	Sobolev space of p-times weakly differentiable functions
$H(u)$	matrix in pressure correction scheme
I	turbulence intensity
J	cost functional
$\hat{J}$	reduced cost functional

$\hat{J}'$	Fréchet derivative of $\hat{J}$
K	von Kármán constant
$\mathcal{K}(\beta)$	integrand of surface sensitivity
L	Lagrangian function
L^j	porous zone
L^1	Lebesgue space of integrable functions
L^2	Lebesgue space of square integrable functions
$\mathcal{L}$	set of porous zones
$\mathcal{L}(X, Y)$	bounded, linear functionals mapping from X to Y
M	discretization matrix
N	neighbor cell
P	owner cell
P_k	production term in SST $k-\omega$ model
Pr	Prandtl number
Pr_t	turbulent Prandtl number
$\mathtt{P}$	Jayatilleke wall function
Q	residual continuity equation
Re	turbulent Reynolds number
R_i	residual momentum equations
$\mathcal{R}$	residual state equations
$\mathfrak{R}$	Riesz isomorphism
S	magnitude of rate-of-strain tensor
S_{ij}	symmetric rate-of-strain tensor
$\hat{S_{ij}}$	adjoint rate-of-strain tensor
S_C	explicit part of source term
S_P	implicit part of source term
S_ϕ	source term
T	temperature
$\hat{T}$	adjoint temperature
T^+	dimensionless temperature
U	control space
U_{ad}	admissible control space
U_h	discrete counterpart to U
U^+	dimensionless velocity
V	control volume
$\dot{V}_i$	total discharge
W_{ad}	admissible set
W_{ad}^h	discrete counterpart to W_{ad}

W_{ij}	vorticity tensor
Y	state space
Y_h	discrete counterpart to Y

Lower-case Greek

α	Darcy porosity term
α_ϕ	under-relaxation factor
α_Ω	porosity function on Ω
$\alpha_\mathcal{L}$	porosity function on $\mathcal{L}$
β	surface normal shape control
β_T	thermal expansion coefficient
β_1	constant in the dissipation boundary condition
β_*	parameter for Armijo step size selection rule
β^*	constant in SST $k-\omega$ model
γ	parameter for Armijo step size selection rule
δ	total variation
δ_p	variation with respect to pressure
δ_u	variation with respect to velocity
δ_T	variation with respect to temperature
δ_α	variation with respect to porosity
$\delta_{\alpha_\mathcal{L}}$	variation with respect to modified porosity
δ_β	variation with respect to surface normal displacement
ϵ	weighting factor for regularization
ζ	parameter in Huber function
θ	angle in polar coordinate system
κ	thermal heat conductivity
κ_e	effective thermal heat conductivity
κ_t	turbulent thermal heat conductivity
λ	step size
μ	dynamic viscosity
μ_e	effective viscosity
μ_t	turbulent dynamic eddy viscosity
ν	kinematic viscosity
ν_t	turbulent kinematic eddy viscosity
ξ	linear interpolation weighting factor
ρ	density
σ	scale factor in Armijo algorithm
τ^w	wall shear stress magnitude
${\tau_i}^w$	wall shear stress

χ characteristic function
ω dissipation rate

Upper-case Greek

Γ boundary of flow domain
Γ_{dsg} part of boundary subject to design modification
Γ_{obj} part of boundary carrying the objective functional
Φ_{ζ} Huber function
Ω computational domain
Ω_{dsg} part of computational domain subject to design modification
Ω_{obj} part of computational domain subject to the objective functional

Superscripts

$*$ dual counterpart
(f) value at face f
k value at k-th iteration
new value from latest iteration
old value from previous iteration
(N) value at computational cell N
(P) value at computational cell P

Subscripts

d desired state
in property associated to inlet
max maximal value
$mean$ mean value
min minimal value
n normal component
out property associated to outlet
ref reference state
sym property associated to symmetry plane
t tangential component
w property associated to wall
0 initial state

Symbols

∇ gradient operator

∇^2	Hessian operator
∇_Γ	tangential gradient operator
Δ_Γ	Laplace-Beltrami operator
$(\ ,\ )$	scalar product
$\langle\ ,\ \rangle$	dual product
$\overline{(\cdot)}$	Reynolds-average operator
$\vec{(\cdot)}$	connecting vector

1. Introduction

1.1. Background and Motivation

This thesis is concerned with the theory and application of continuous adjoint shape and topology optimization for heating, ventilation and air-conditioning (HVAC) components of aircrafts.
During the recent decades, aircraft manufacturing processes, related to safety and economy issues, significantly improved. Up to now, the number of passengers has grown. Flying is progressively becoming a more commonly used means of transport. If the level of cabin comfort is high, the value of the whole aircraft increases. To distinguish from competitors, cabin comfort has gained a lot in importance. Nevertheless, there is still a need for improvement of the systems efficiency, leading to a saving of the operating costs. To be able to predict the properties of the aircraft components, the computation of the internal and external aerodynamic flows is irremissible. Computational fluid dynamics has become a powerful discipline to design fluid dynamic devices since the development of high-performance computers and efficient algorithms [40]. Numerical simulations circumvent the need for time-consuming and expensive experiments and greatly simplify parameter studies.
An optimization of the aircraft components involves not only the physical description of the flow, but also the prescription and accomplishment of suitable design modifications to improve a cost functional. An efficient way to determine proper design modifications is the adjoint method. Optimal control, basically the superordinate concept behind adjoint methods, combines the physics, the design and the cost functional in one problem. Dating back to the 17th century [83], it became famous again in the 1960's (Bryson, [10]) when modern computer hardware rapidly developed. According to Lions [51], an optimal control problem consists of the control, which is modified, a state, which depends on the control, and a cost functional, which depends on the state and the control. From the optimal control theory, adjoint fluid dynamic methods evolved when, in 1973 Pironneau developed the adjoint Stokes equations [66] and Jameson derived the adjoint Euler equations in 1988 [39] and later the adjoint Navier-Stokes equations in 1998 [44]. Since then, the adjoint method has been widely used for different kinds of fluid dynamic applications, for example for the optimization of train head cars [38], in automotive industry [27], [14] or for the hydrodynamic optimization of ship hull-design [79].
Contrary to direct methods, which require the modification of the control to compute the derivative of the cost functional, adjoint methods assess the modification of the control by solving a dual, so called *adjoint* problem, which yields a computational effort comparable to the solution of the primal problem. The method is independent of the number of

design parameters but scales with the amount of cost functionals. Hence, if many design parameters and only few objectives are present, the adjoint method is preferable. Optimization of heating, ventilation and air-conditioning components is based upon the solution of the incompressible Navier-Stokes-Fourier equations, consisting of the buoyancy-driven momentum equations, the continuity equation and the energy equation, and adequate cost functionals involving comfort related issues in a ducted setting. Basically, there are two branches of adjoint methods; for continuous adjoint methods, the principle of *first optimize then discretize* is followed. First the optimal control problem and the adjoint equations are derived, then a discretization follows. The advantage lies in the simple way of deducing the continuous adjoint equations and the analogy to the primal ones. In this way, big portions of the numerical solver can be reused. Contrary to this, the discrete method [21], [9] follows the principle of *first discretize then optimize*. The dual problem is derived from the discretized primal problem. The deduction is very time-consuming, in favor of the resulting equations to be exactly dual to the discretized primal equations. To yield duality for the continuous adjoint approach, the discretization has to be adapted properly [80]. The result of both methods is the derivative of the cost functional, which facilitates the computation of the gradient. Computing the gradient is a crucial point. To perform a gradient method, it is irremissible. However, it is still common practice to use the sensitivity directly for the design update which is untenable. Solving the Laplace-Beltrami equation results in the Riesz representative of the sensitivity in Sobolev spaces [73], exactly corresponding to the gradient. Other approaches approximate the gradient by using filter operations [81], [40]. A local minimum is achieved by application of gradient methods, such as steepest descent. The modification of the design parameters is accomplished, according to the gradient's prescription. In this context, the computation of a proper step size in an efficient way is an important point.

1.2. Starting Point and Direction

In this thesis, a continuous adjoint framework in conjunction with shape and porosity modifications is employed. For the physical description of the flow, the incompressible Navier-Stokes-Fourier equations are simplified to the steady state incompressible Reynolds-averaged Navier-Stokes-Fourier (RANS-F) equations. Turbulence is modeled by a two-equation model. Darcy's law [13] accounts for modeling the porosity.
The continuous adjoint Navier-Stokes-Fourier equations and the sensitivity are derived by a variational approach. The turbulence is not part of the derivation of adjoint formulations, thus, treated as frozen. An algebraic equation system is derived via the finite volume method and solved by a semi-implicit pressure linked equation solver, implemented in the software package OpenFOAM®[23]. Solving the Laplace-Beltrami equation results in the gradient, leading to a local minimum by application of gradient methods (line search strategies) and the accomplishment of appropriate design modifications. For the shape optimization, each CFD-parameter on the boundary serves as design parameter and is thus enabled for surface-normal displacements. This requires the computation of a modi-

fied mesh, obtained from a commercial software (automatic net-generation for structural analysis (ANSA™) [4]). In topology optimization, the design space consists of all CFD parameters inside the computational domain. By modification of the porosity parameter, cells with a negative effect on the cost functional turn solid by an iterative one shot approach [84], whereas cells with positive impact stay fluid [6], [60]. For both control modes, design requirements are irremissible in the practical application.
This thesis outlines the demands concerning the applicability of adjoint theory to industrial practice. The goal is to combine both theory and practice in a robust, yet mathematically correct manner. This mainly applies to adaptation of the adjoint method to ducted flows inside heating, ventilation and air-conditioning components. Design constraints referring to requirements for the porosity distribution inside the computational domain, arising from industrial feasibility, are investigated. With regard to the direct application of the sensitivity to the design optimization, it is emphasized that the only way is to compute the gradient. In this thesis, this goal is achieved by solution of the Laplace-Beltrami equation. With respect to gradient methods, it is investigated how to compute a proper step size in an efficient manner. To meet the demands for the industrial design process, pragmatism *and* mathematical correctness are required, leading to a balancing act. The approaches are implemented, validated and verified via simulation of proper fluid dynamic test-cases. The arising framework is applied to industrial cases of aircraft components, related to heating, ventilation and air-conditioning.

1.3. Present Contributions

The specific contributions conducted in this thesis are stated in the following:

- Implementation of an adjoint internal energy equation: A solver for the adjoint Reynolds-averaged Navier-Stokes (RANS) equations has already been present in the framework of OpenFOAM®. The solver is extended to the adjoint Reynolds-averaged Navier-Stokes-Fourier equations. Concurrently, cost functionals related to comfort criteria are derived and implemented.

- Implementation of Laplace-Beltrami solver: The solver for the Laplace-Beltrami equation has been implemented in OpenFOAM® in the context of a master's thesis [29], supervised, amongst others, by the author.

- Derivation and implementation of reduced Armijo approach: The Armijo rule [2] is an efficient and reliable, though rather expensive means, to compute a proper step size. Therefore, the method is transformed to a reduced approach, such that the time-consuming evaluation of the Armijo rule is only performed on a coarse mesh level.

- Derivation and implementation of an approximated regularization term for promotion of sparsity: For problems, where sparse control distributions are preferred, a remedy

consists of the insertion of an L^1-regularization term [76] into the cost functional. As the non-differentiability of this term may lead to problems, related to the computation of the derivative, the regularization term may be approximated by a smooth variant.

- Verification of the sensitivity: The sensitivities are compared to derivatives obtained from finite differentiation. A simple test case, related to heat transfer in a ducted setting, serves as validation case.
- Verification of the gradient obtained from Laplace-Beltrami equation: The numerical solution of the Laplace-Beltrami equation is compared to the exact solution of an analytic test case.
- Validation of limits for mesh coarsening: To justify the reduced Armijo approach, a mesh study is performed for different levels of grid coarseness. It is determined up to which level of coarseness a still reliable numerical solution is possible and from what point on the numerical solution deteriorates.
- Validation of sparsity approach: The effect of the inserted regularization term on the sparsity is validated by two simple test cases. The level of sparsity is related to the quantity of the additional regularization term and compared to the cost functional improvement.
- Shape optimization of aircraft components: The adjoint shape optimization is applied to the cabin air outlet of a passenger aircraft. Two designs corresponding to distinct iteration loops are created to improve the cost functional. Furthermore, experiments have been conducted by the German Aerospace Center in Göttingen to substantiate the numerical results. To validate the extended adjoint solver, the shape optimization is applied to a mixing chamber of an aircraft, considering buoyancy-driven flows. Four designs are created focusing upon the cost functional mixing efficiency.
- Application of step size computation to aircraft component: The reduced Armijo approach is applied to the cabin air outlet of a passenger aircraft. The approach is evaluated by comparison of the computational time and the cost functional improvement to the results of the steepest descent optimization and the full Armijo approach.
- Sparsity promotion via regularization term for aircraft component: The optimization involving the sparsity promoting regularization term is applied to the cabin air outlet of a cockpit. The level of sparsity and the cost functional improvement are evaluated for different parameters.

1.4. Plan of this Thesis

The structure of this thesis is as follows: In Chapter 2 the theory of optimal control is described, also involving the adjoint approach and appropriate line search techniques. In

Chapter 3 the system of the governing fluid dynamic equations is given, namely the incompressible Reynolds-averaged Navier-Stokes-Fourier equations. At the end of Chapter 3 the considered cost functionals are described. In Chapter 4 the adjoint incompressible Reynolds-averaged Navier-Stokes-Fourier equations are derived with appropriate boundary conditions and the related sensitivity. Additionally, the gradient computation from shape and topology sensitivities is described. In Chapter 5 the numerical framework is given, namely the finite volume method, involving primal and adjoint discretization schemes for the fluid dynamic equations, and the solution of the arising algebraic equation system. Chapter 6 presents the results of the verification and validation studies. In Chapter 7 the results for the application to aircraft components are given. The thesis closes with conclusions and an outlook in Chapter 8. Furthermore, a list of notations is provided in the glossary. The theory of functional analysis and parts of the derivation are confined in the appendix. Note that Einstein's sum convention applies to small-type Latin subscripts, referring to Cartesian coordinates, unless declared differently. In symbolic notation, the number of underlines corresponds to the order of a tensor.

2. Optimal Control of Partial Differential Equations

This chapter presents the mathematical framework for the optimization technique, namely the optimal control of partial differential equations. The approach is subsequently specified to optimization with fluid dynamic equations. Moreover, the gradient method for the optimization is presented.

2.1. Optimal Control Problem

The definition of an optimal control problem is based on Hinze et al. [32]. The starting point is Equation (2.1)

$$\min_{\mathfrak{y}\in Y,\mathfrak{u}\in U} J(\mathfrak{y},\mathfrak{u}) \;\text{ subject to }\; e(\mathfrak{y},\mathfrak{u})=0,\;\; (\mathfrak{y},\mathfrak{u})\in W_{ad}\,, \tag{2.1}$$

where $J : Y \times U \to \mathbb{R}$ is the objective functional, $e : Y \times U \to Z$ is an operator, $W_{ad} \subset W := Y \times U$ the admissible space, a nonempty and closed set, with Banach spaces U, Y, Z (see Appendix A). The set U defines the control space, Y denotes the state space and $e(\mathfrak{y},\mathfrak{u}) = 0$ the state equation (system of partial differential equations). The goal is to find a control $\mathfrak{u}$ which minimizes the cost functional $J(\mathfrak{y},\mathfrak{u})$ with respect to the state equation $e(\mathfrak{y},\mathfrak{u}) = 0$ and under consideration of the admissible set W_{ad}. Problems of this structure are called *optimal control problems*. Supposing that the state equation $e(\mathfrak{y},\mathfrak{u}) = 0$ leads to a unique solution of the state $\mathfrak{y} \in Y$ for each control $\mathfrak{u} \in U$, $\mathfrak{y}$ is written as a function of $\mathfrak{u}$, $\mathfrak{y}(\mathfrak{u})$. Inserting $\mathfrak{y}(\mathfrak{u})$ in (2.1) results in the reduced problem,

$$\min_{\mathfrak{u}\in U} \hat{J}(\mathfrak{u}) := J(\mathfrak{y}(\mathfrak{u}),\mathfrak{u}) \;\text{ subject to }\; \mathfrak{u}\in U_{ad} := \{\mathfrak{u}\in U : (\mathfrak{y}(\mathfrak{u}),\mathfrak{u})\in W_{ad}\}\,. \tag{2.2}$$

It is supposed that J and e are continuously Fréchet differentiable (see Appendix A) and the derivative of the state equation with respect to $\mathfrak{y}$, denoted as $e_{\mathfrak{y}}$, is a bounded, linear operator, $e_{\mathfrak{y}}(\mathfrak{y}(\mathfrak{u}),\mathfrak{u}) \in \mathcal{L}(Y,Z)$ (see Appendix A), which is continuously invertible. Thus, it holds from the implicit function theorem (compare [32]) that $\mathfrak{y}(\mathfrak{u})$ is continuously differentiable. The computation of the derivative $\mathfrak{y}'(\mathfrak{u})$ is conducted by differentiation of the state equation $e(\mathfrak{y}(\mathfrak{u}),\mathfrak{u}) = 0$ with respect to $\mathfrak{u}$ and application of the chain rule

$$e_{\mathfrak{y}}\left(\mathfrak{y}(\mathfrak{u}),\mathfrak{u}\right)\mathfrak{y}'(\mathfrak{u}) + e_{\mathfrak{u}}(\mathfrak{y}(\mathfrak{u}),\mathfrak{u}) = 0\,. \tag{2.3}$$

2.2. Adjoint Approach

This section describes the efficient computation of the cost functional derivative from the adjoint approach. The directional derivative of the reduced cost functional $\hat{J}(u)$ in a direction $s \in U$ denotes $d\hat{J}(\mathfrak{u}, s)$ (see Appendix A). In the regarded case, $\mathfrak{y}$ is a function depending on $\mathfrak{u}$, thus requires to apply the chain rule

$$d\hat{J}(\mathfrak{u}, s) = \langle \hat{J}'(\mathfrak{u}), s \rangle_{U^*,U} = \langle J_{\mathfrak{y}}(\mathfrak{y}(\mathfrak{u}), \mathfrak{u}), \mathfrak{y}'(\mathfrak{u})s \rangle_{Y^*,Y} + \langle J_{\mathfrak{u}}(\mathfrak{y}(\mathfrak{u}), \mathfrak{u}), s \rangle_{U^*,U} \,, \tag{2.4}$$

where $\hat{J}'(\mathfrak{u})$ denotes the Fréchet derivative of $\hat{J}$ with the dual spaces U^*, Y^* and related dual pairing (see Appendix A). In this expression, the sensitivity $d\mathfrak{y}(\mathfrak{u}, s) = \mathfrak{y}'(\mathfrak{u})s$ appears, possibly computed by solving the linearized state equation (2.3),

$$e_{\mathfrak{y}}(\mathfrak{y}(\mathfrak{u}), \mathfrak{u})\mathfrak{y}'(\mathfrak{u})s + e_{\mathfrak{u}}(\mathfrak{y}(\mathfrak{u}), \mathfrak{u})s = 0 \,. \tag{2.5}$$

If the whole derivative $\hat{J}'(\mathfrak{u})$ is required, the computation is expensive as Equation (2.5) has to be solved for each basis vector $s \in U$. Thus, the effort grows with the dimension of the control space U. However, by using the adjoint of the operator $\mathfrak{y}'(\mathfrak{u})$, the derivative $\hat{J}'(\mathfrak{u})$ can also be derived by (see Appendix A)

$$\begin{aligned} \langle \hat{J}'(\mathfrak{u}), s \rangle_{U^*,U} =& \langle J_{\mathfrak{y}}(\mathfrak{y}(u), \mathfrak{u}), \mathfrak{y}'(\mathfrak{u})s \rangle_{Y^*,Y} + \langle J_{\mathfrak{u}}(\mathfrak{y}(\mathfrak{u}), \mathfrak{u}), s \rangle_{U^*,U} \\ =& \langle \mathfrak{y}'(\mathfrak{u})^* J_{\mathfrak{y}}(\mathfrak{y}(\mathfrak{u}), \mathfrak{u}), s \rangle_{U^*,U} + \langle J_{\mathfrak{u}}(\mathfrak{y}(\mathfrak{u}), \mathfrak{u}), s \rangle_{U^*,U} \,. \end{aligned} \tag{2.6}$$

Consequently, $\hat{J}'(\mathfrak{u}) \in U^*$ is given by

$$\hat{J}'(\mathfrak{u}) = \mathfrak{y}'(\mathfrak{u})^* J_{\mathfrak{y}}(\mathfrak{y}(\mathfrak{u}), \mathfrak{u}) + J_{\mathfrak{u}}(\mathfrak{y}(\mathfrak{u}), \mathfrak{u}) \,. \tag{2.7}$$

Hence, in comparison to the first approach, only the vector $\mathfrak{y}'(\mathfrak{u})^* J_{\mathfrak{y}}(\mathfrak{y}(\mathfrak{u}), \mathfrak{u}) \in U^*$ instead of the whole operator $\mathfrak{y}'(\mathfrak{u}) \in \mathcal{L}(U, Y)$ is required to compute the derivative of the cost functional. From the linearized state equation (2.3), it follows

$$\mathfrak{y}'(\mathfrak{u}) = -e_{\mathfrak{u}}(\mathfrak{y}(\mathfrak{u}), \mathfrak{u}) e_{\mathfrak{y}}(\mathfrak{y}(\mathfrak{u}), \mathfrak{u})^{-1} \,, \tag{2.8}$$

and, by duality, respectively,

$$\mathfrak{y}'(\mathfrak{u})^* = -e_{\mathfrak{u}}(\mathfrak{y}(\mathfrak{u}), \mathfrak{u})^* e_{\mathfrak{y}}(\mathfrak{y}(\mathfrak{u}), \mathfrak{u})^{-*} \,. \tag{2.9}$$

Multiplication with the derivative of the cost functional with respect to the state leads to

$$\mathfrak{y}'(\mathfrak{u})^* J_{\mathfrak{y}}(\mathfrak{y}(\mathfrak{u}), \mathfrak{u}) = -e_{\mathfrak{u}}(\mathfrak{y}(\mathfrak{u}), \mathfrak{u})^* e_{\mathfrak{y}}(\mathfrak{y}(\mathfrak{u}), \mathfrak{u})^{-*} J_{\mathfrak{y}}(\mathfrak{y}(\mathfrak{u}), \mathfrak{u}) \,. \tag{2.10}$$

It follows

$$\mathfrak{y}'(\mathfrak{u})^* J_{\mathfrak{y}}(\mathfrak{y}(\mathfrak{u}), \mathfrak{u}) = e_{\mathfrak{u}}(\mathfrak{y}(\mathfrak{u}), \mathfrak{u})^* \mathfrak{p}(\mathfrak{u}) \,, \tag{2.11}$$

with the *adjoint state* $\mathfrak{p} = \mathfrak{p}(\mathfrak{u}) \in Z^*$ solving the *adjoint equation*

$$e_{\mathfrak{y}}(\mathfrak{y}(\mathfrak{u}), \mathfrak{u})^* \mathfrak{p} = -J_{\mathfrak{y}}(\mathfrak{y}(\mathfrak{u}), \mathfrak{u})\,. \tag{2.12}$$

Combining (2.7) and (2.11), the derivative of $\hat{J}$ can be expressed as

$$\hat{J}'(\mathfrak{u}) = e_{\mathfrak{u}}(\mathfrak{y}(\mathfrak{u}), \mathfrak{u})^* \mathfrak{p} + J_{\mathfrak{u}}(\mathfrak{y}(\mathfrak{u}), \mathfrak{u})\,. \tag{2.13}$$

The adjoint equation (2.12) may also be derived from the *Lagrangian function* $L : Y \times U \times Z^* \to \mathbb{R}$,

$$L(\mathfrak{y}, \mathfrak{u}, \mathfrak{p}) = J(\mathfrak{y}, \mathfrak{u}) + \langle \mathfrak{p}, e(\mathfrak{y}, \mathfrak{u}) \rangle_{Z^*,Z}\,, \tag{2.14}$$

where $\mathfrak{p} \in Z^*$ is at first arbitrary and is specified later on. Using $\mathfrak{y} = \mathfrak{y}(\mathfrak{u})$ and $e(\mathfrak{y}, \mathfrak{u}) = 0$, results in

$$\hat{J}(\mathfrak{u}) = J(\mathfrak{y}(\mathfrak{u}), \mathfrak{u}) = J(\mathfrak{y}(\mathfrak{u}), \mathfrak{u}) + \langle \mathfrak{p}, e(\mathfrak{y}(\mathfrak{u}), \mathfrak{u}) \rangle_{Z^*,Z} = L(\mathfrak{y}(\mathfrak{u}), \mathfrak{u}, \mathfrak{p})\,. \tag{2.15}$$

To obtain the derivative $\hat{J}'(\mathfrak{u})$, Equation (2.15) is differentiated,

$$\langle \hat{J}'(\mathfrak{u}), s \rangle_{U^*,U} = \langle L_{\mathfrak{y}}(\mathfrak{y}(\mathfrak{u}), \mathfrak{u}, \mathfrak{p}), \mathfrak{y}'(\mathfrak{u}) s \rangle_{Y^*,Y} + \langle L_{\mathfrak{u}}(\mathfrak{y}(\mathfrak{u}), \mathfrak{u}, \mathfrak{p}), s \rangle_{U^*,U}\,, \tag{2.16}$$

for all $s \in U$. A special $\mathfrak{p} = \mathfrak{p}(\mathfrak{u})$ is selected, such that

$$L_{\mathfrak{y}}(\mathfrak{y}(\mathfrak{u}), \mathfrak{u}, \mathfrak{p}) = 0\,, \tag{2.17}$$

resulting in

$$\begin{aligned} \langle L_{\mathfrak{y}}(\mathfrak{y}(\mathfrak{u}), \mathfrak{u}, \mathfrak{p}), v \rangle_{Y^*,Y} &= \langle J_{\mathfrak{y}}(\mathfrak{y}, \mathfrak{u}), v \rangle_{Y^*,Y} + \langle \mathfrak{p}, e_{\mathfrak{y}}(\mathfrak{y}, \mathfrak{u}) v \rangle_{Z^*,Z} \\ &= \langle J_{\mathfrak{y}}(\mathfrak{y}, \mathfrak{u}) + e_{\mathfrak{y}}(\mathfrak{y}, \mathfrak{u})^* \mathfrak{p}, v \rangle_{Y^*,Y}\,, \end{aligned} \tag{2.18}$$

for all $v \in Y$. It follows the adjoint equation from the Lagrangian function,

$$L_{\mathfrak{y}}(\mathfrak{y}(\mathfrak{u}), \mathfrak{u}, \mathfrak{p}) = J_{\mathfrak{y}}(\mathfrak{y}(\mathfrak{u}), \mathfrak{u}) + e_{\mathfrak{y}}(\mathfrak{y}(\mathfrak{u}), \mathfrak{u})^* \mathfrak{p} = 0\,, \tag{2.19}$$

exactly as in (2.12). Accordingly, the derivative may be computed from Equation (2.16), using Equation (2.14) and Equation (2.17),

$$\langle \hat{J}'(\mathfrak{u}), s \rangle_{U^*,U} = \langle L_{\mathfrak{u}}(\mathfrak{y}(\mathfrak{u}), \mathfrak{u}, \mathfrak{p}), s \rangle_{U^*,U} = \langle J_{\mathfrak{u}}(\mathfrak{y}(\mathfrak{u}), \mathfrak{u}) + e_{\mathfrak{u}}(\mathfrak{y}(\mathfrak{u}), \mathfrak{u})^* \mathfrak{p}, s \rangle_{U^*,U}\,, \tag{2.20}$$

for all $s \in U$.
Consequently, it holds for the derivative of the cost functional from the Lagrangian function

$$\hat{J}'(\mathfrak{u}) = L_{\mathfrak{u}}(\mathfrak{y}(\mathfrak{u}), \mathfrak{u}, \mathfrak{p}) = J_{\mathfrak{u}}(\mathfrak{y}(\mathfrak{u}), \mathfrak{u}) + e_{\mathfrak{u}}(\mathfrak{y}(\mathfrak{u}), \mathfrak{u})^* \mathfrak{p}(\mathfrak{u})\,, \tag{2.21}$$

exactly corresponding to Equation (2.13). The following steps lead to the computation of the derivative from the Lagrangian function.

- Derive the adjoint equation (2.19) from the variation of the Lagrangian function,

$$L_{\mathrm{y}}(\mathrm{y}(\mathrm{u}), \mathrm{u}, \mathrm{p}) = 0\,. \tag{2.22}$$

- By solving Equation (2.22) for $\mathrm{p} = \mathrm{p}(\mathrm{u})$, the derivative is computed from Equation (2.21),

$$\hat{J}'(\mathrm{u}) = L_{\mathrm{u}}(\mathrm{y}(\mathrm{u}), \mathrm{u}, \mathrm{p}). \tag{2.23}$$

Contrary to the computation via the linearized state equation (2.3), the cost does not grow with the dimension of the control space. In the following, the optimal control theory is applied to fluid dynamic equations.

2.3. Optimization with Fluid Dynamic Equations

After introducing the mathematical background of the adjoint approach, the above stated theory is applied to a set of fluid dynamic partial differential equations. The state y corresponds to the physical properties, i.e. velocity, pressure and temperature, depending on the state equations $e(\mathrm{y}, \mathrm{u})$, namely the fluid dynamic partial differential equations, fulfilled on a bounded domain Ω. The goal is to minimize a cost functional $J(\mathrm{y}, \mathrm{u})$ on a subdomain $\Omega_{obj} \subset \Omega$ by application of a control u onto the design space Ω_{dsg}. To improve the cost functional via modification of the design space, the derivative of the cost functional, $\hat{J}'(\mathrm{u})$, w.r.t. the control is required. From the preceding section it is evident that the basic ingredients for computing the derivative is to solve the adjoint equation (2.19) and to compute the derivative, i.e. the sensitivity, from Equation (2.21). The variations $L_{\mathrm{y}}(\mathrm{y}(\mathrm{u}), \mathrm{u}, \mathrm{p})$ and $L_{\mathrm{u}}(\mathrm{y}(\mathrm{u}), \mathrm{u}, \mathrm{p})$ of the Lagrangian function have to be derived with respect to the state y and the control u. The state equations $\mathcal{R}$ (exemplarily the Reynolds-averaged Navier-Stokes equations, see Section 3.1) are denoted in residual form as $\mathcal{R} = (R_1, R_2, R_3, Q)$, where R_1, R_2, R_3 mark the residual momentum equations and Q the residual continuity equation. The Lagrangian function is represented by

$$L := J + \int_{\Omega} \left[\hat{u}_i R_i + \hat{p} Q\right] \, d\Omega\,, \tag{2.24}$$

where $(\hat{u}_i, \hat{p})$ denote the Lagrange multipliers for momentum and continuity equation, respectively. The adjoint equation (2.22) is derived by a variational approach, viz.

$$\delta_u L + \delta_p L = \delta_u J + \int_{\Omega} (\hat{u}_i, \hat{p}) \delta_u \mathcal{R} \, d\Omega + \delta_p J + \int_{\Omega} (\hat{u}_i, \hat{p}) \delta_p \mathcal{R} \, d\Omega = 0\,, \tag{2.25}$$

where δ_u and δ_p mark the variation w.r.t. the state, velocity u_i and pressure p. For state equations including the temperature (e.g. Navier-Stokes-Fourier equations (Section 3.2)), the variation w.r.t. the temperature is included, accordingly. The variation of the Lagrangian function with respect to β, denoted as δ_β,

$$\delta_\beta L = \delta_\beta J + \int_\Omega (\hat{u}_i, \hat{p}) \delta_\beta \mathcal{R} \; d\Omega \,, \tag{2.26}$$

leads to the sensitivity (2.23), involving the control β, here, the continuous surface normal displacement of the design boundary. The first term of Equation (2.26) represents the explicit dependence of the cost functional on the control. The related computation is performed in a straightforward manner by purely geometric considerations on the primal flow field [60]. The second term of Equation (2.26), $\int_\Omega (\hat{u}_i, \hat{p}) \delta_\beta \mathcal{R} \; d\Omega$, can be recast into a boundary integral as shown by Soto and Löhner [74]. One utilizes the fact that the residual flow equations are also fulfilled under the total variation, denoted as δ, such that

$$\delta \mathcal{R} = \delta_\beta \mathcal{R} + \delta_u \mathcal{R} + \delta_p \mathcal{R} = 0 \,. \tag{2.27}$$

Therefore, the variation w.r.t. the control transforms to

$$\delta_\beta \mathcal{R} = -\delta_u \mathcal{R} - \delta_p \mathcal{R} \,, \tag{2.28}$$

and Equation (2.26) becomes

$$\delta_\beta L = \delta_\beta J - \int_\Omega (\hat{u}_i, \hat{p}) \delta_u \mathcal{R} d\Omega - \int_\Omega (\hat{u}_i, \hat{p}) \delta_p \mathcal{R} d\Omega \,. \tag{2.29}$$

The integrals on the right-hand side correspond to the adjoint equation (2.25) without the contributions of the cost functional, $\delta_u J$ and $\delta_p J$. Integration by parts results in boundary and volume integrals. If the cost functional is independent from the domain interior, the volume terms cancel by virtue of $\hat{u}_i$ and $\hat{p}$ satisfying the adjoint equation (2.25). In this case, the integrals of Equation (2.29) reduce to boundary integrals depending on the flow variations δu_i and δp. As the surface deformations are in normal direction only, a Taylor series expansion is utilized to approximate the variations with respect to the state u_i and p, according to [74], using

$$\delta u_i = \frac{\partial u_i}{\partial n} \delta\beta + O\left((\delta\beta)^2\right) \,, \tag{2.30}$$

$$\delta p = \frac{\partial p}{\partial n} \delta\beta + O\left((\delta\beta)^2\right) \,, \tag{2.31}$$

where n denotes the outward normal direction. Due to the termination after the linear term, this approach can only recover linear changes of the flow. Changes due to nonlinear flow phenomena, often related to separation, can not be predicted by the performed approximation. For that reason, the approximation is only reliable for small changes of

the design which do not cause substantial changes of the flow. The following strategy is pursued to derive the adjoint equations and the sensitivity.

- Derive via a variational approach the adjoint equation from Equation (2.25)

$$\delta_u L + \delta_p L = \delta_u J + \int_\Omega (\hat{u}_i, \hat{p}) \delta_u \mathcal{R} \; d\Omega + \delta_p J + \int_\Omega (\hat{u}_i, \hat{p}) \delta_p \mathcal{R} \; d\Omega = 0 \,, \tag{2.32}$$

  by choosing the Lagrange multipliers properly.

- The sensitivity is computed from Equation (2.26)

$$\delta_\beta L = \delta_\beta J + \delta_\beta \int_\Omega (\hat{u}_i, \hat{p}) \mathcal{R} d\Omega \,. \tag{2.33}$$

  Using Equation (2.28), the variation w.r.t. the control (2.33) can be recast into

$$\delta_\beta L = \delta_\beta J - \int_\Omega (\hat{u}_i, \hat{p}) \delta_u \mathcal{R} d\Omega - \int_\Omega (\hat{u}_i, \hat{p}) \delta_p \mathcal{R} d\Omega \,. \tag{2.34}$$

  In case of no cost functional contributions on the interior domain, the volume integrals reduce to boundary integrals. In this case, the variations δ are obtained from the Taylor series expansion (2.30), (2.31).

2.4. Continuous vs. Discrete Adjoint Approach

Two main approaches exist in the adjoint theory, namely continuous adjoint and discrete adjoint approaches. The continuous adjoint approach, considered in this thesis, is constructed under the aspect *first optimize, then discretize*. The adjoint equations are derived from the continuous primal partial differential equations by multiplication with Lagrange multipliers (see Equation (2.24)) and variation with respect to the state. To solve the adjoint system numerically, the equations have to be discretized subsequently. The simply performed derivation of the adjoint system is advantageous. Associated therewith, the solver for the numerical equations may be reused as the type of the equations is similar. A physical interpretation of the equations is possible, thus, boundary and initial conditions are set more easily, discretization schemes are flexibly chosen and the equations are solved individually. Contrariwise, the discretization of the continuous adjoint equations leads to schemes that are in general not dual to the primal discretization. Hereby, duality means that the adjoint discretization matrices are obtained from the primal discretization matrices by transposition. The discrete adjoint approach is obtained from the principle of *first discretize, then optimize*. All quantities in the optimal control problem (2.1) are discretized, leading to

$$\min_{\mathtt{y}_h \in Y_h, \mathtt{u}_h \in U_h} J(\mathtt{y}_h, \mathtt{u}_h) \;\text{ subject to }\; e(\mathtt{y}_h, \mathtt{u}_h) = 0 \,, \;\; (\mathtt{y}_h, \mathtt{u}_h) \in W_{ad}^h \,, \tag{2.35}$$

where Y and U are replaced by finite dimensional spaces Y_h, U_h and W_{ad} by an discrete counterpart W_{ad}^h. In this manner, the problem (2.35) converts to

$$\min_{\mathtt{y}_h \in Y_h, \mathtt{u}_h \in U_h} J(\mathtt{y}_h, \mathtt{u}_h) \text{ subject to } M\mathtt{y}_h = s\,, s \in S\,, \tag{2.36}$$

with discretization matrix M, representing the solution operator of $e(\mathtt{y}_h, \mathtt{u}_h)$, and $S \subset \mathbb{R}^m$. The transposition of the discretization matrix M leads to the adjoint solution operator. As the adjoint equations are derived from the discretized primal equations, the discrete adjoint approach comprises duality between both, primal and adjoint, discrete equation systems. The disadvantage of the cumbersome derivation of the discretization matrix may be circumvented by automatic differentiation [25, 20], where the differentiation is carried out on code level. However, the system is inflexible, as the discretization schemes cannot be chosen individually. Ideally, both approaches should lead to the same discretization. Nadarajah and Jameson [42, 43] performed a detailed gradient comparison study of the continuous and discrete adjoint approaches, using the Euler equations and the Navier-Stokes equations, and found that the difference between the continuous and discrete gradients decreases as the mesh size increases. In typical shape optimization problems, the differences are small enough that they have no significant effect on the final result [41]. Additionally, as shown in [82], hybrids of discrete and continuous adjoint methods can be pursued such that the discretization of the continuous adjoint system is dual to the primal one. In this way, the disadvantage of the continuous adjoint approach is avoided. An overview for both approaches is given, for example, in [22].

2.5. Optimization with Gradient Descent

This section considers the utilization of gradient methods to improve the design. The goal is to modify the control such that

$$\hat{J}(\mathfrak{u}^{k+1}) < \hat{J}(\mathfrak{u}^k)\,, \tag{2.37}$$

where $\mathfrak{u}^k$ denotes the control belonging to the iteration k.
A vector d denotes the *descent direction* of $\hat{J}$, starting from a control $\mathfrak{u}$, if there exists a $\overline{\lambda} > 0$, such that

$$\hat{J}\,(\mathfrak{u} + \lambda d\,) < \hat{J}(\mathfrak{u}) \quad \forall\, \lambda \in (0, \overline{\lambda}\,]\,. \tag{2.38}$$

λ is called *step length*. Theorem 1 characterizes the descent direction (compare [85]).

Theorem 1. *A vector d is a descent direction of a continuously differentiable cost functional $\hat{J}$ for control $\mathfrak{u}$ if*

$$\nabla \hat{J}(\mathfrak{u})^T d < 0\,. \tag{2.39}$$

In the *gradient descent*, also known as *steepest descent*, the descent direction d is determined from the negative gradient,

$$d = -\nabla \hat{J}(\mathfrak{u}) \,. \tag{2.40}$$

With this choice, condition (2.39) is automatically fulfilled. Note that gradient methods are only capable of detecting local minima. If the cost functional contains multiple minima, then the gradient approach generally converges to the nearest local minimum without searching for further minima in the design space [22]. The gradient $\nabla \hat{J}$ is computed from the sensitivity as later discussed in Section 4.5.
For two times continuously differentiable cost functionals $\hat{J}$, the *Newton method* may be utilized for minimization. Applied to the minimization problem, the necessary optimality condition for cost functional $\hat{J}$ results in the computation of zeros for the gradient of the current control $\mathfrak{u}^k$,

$$\nabla \hat{J}(\mathfrak{u}^k) = 0 \,. \tag{2.41}$$

A vector d^k is determined, that fulfills

$$\nabla \hat{J}(\mathfrak{u}^k + d^k) = 0 \tag{2.42}$$

in iteration k. The function is approximated by a linear Taylor series expansion,

$$\nabla \hat{J}(\mathfrak{u}^k + d^k) \approx \nabla \hat{J}(\mathfrak{u}^k) + \nabla^2 \hat{J}(\mathfrak{u}^k) d^k \,. \tag{2.43}$$

By requiring Equation (2.42) to be fulfilled, Newton's method proposes an equation for the direction d^k,

$$\nabla^2 \hat{J}(\mathfrak{u}^k) d^k = -\nabla \hat{J}(\mathfrak{u}^k) \,, \tag{2.44}$$

in iteration k. Here, $\nabla^2 \hat{J}(\mathfrak{u}^k)$ denotes the *Hessian* of the cost functional $\hat{J}$. The computation of the Hessian for the Newton method is a critical point as it is computationally expensive. An alternative is to employ the Quasi-Newton method (see for example [85]). In Section 2.6 a fast and efficient step size strategy based on the *Armijo rule* is pursued.

2.6. Step Size Control via Armijo Rule

The choice of a proper step size λ in Equation (2.38) is a crucial aspect in the gradient method. If the step size is too small, it takes much time to obtain the optimal design. Choosing the step size too large ($\lambda > \overline{\lambda}$) may lead to deterioration of the cost functional. In industrial applications, usually, the computational limitations prohibit the employment of computationally expensive methods for the step size computation. Therefore, a constant step size is often chosen rather too small than too big, making more update steps necessary until a solution near the optimum is achieved. In this section an efficient and computatio-

nally affordable method to compute the step length is described, based on the Armijo step length selection rule [2]. The gradient is scaled with $\sigma > 0$ to obtain the search direction d. The Armijo rule reads: Let $\beta_* \in (0,1)$ and $\gamma \in (0,1)$ be fixed parameters. Determine the largest scalar $\lambda \in \{1, \beta_*, {\beta_*}^2, \cdots\}$, such that Equation (2.45) is fulfilled,

$$\hat{J}\left(\mathfrak{u} + \lambda d\right) - \hat{J}(\mathfrak{u}) \leq \lambda\gamma\nabla\hat{J}(\mathfrak{u})^T d\,. \tag{2.45}$$

Figure 2.6 illustrates the Armijo rule.

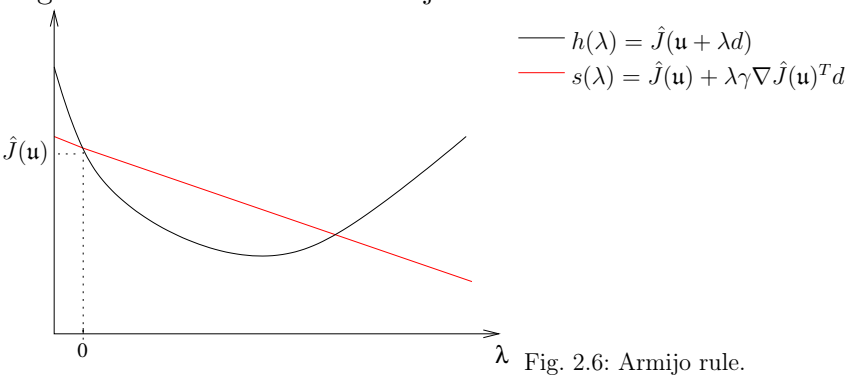

Fig. 2.6: Armijo rule.

The inequality (2.45) is fulfilled for all λ at which the corresponding graph $h(\lambda) := \hat{J}\left(\mathfrak{u} + \lambda d\right)$ is on or below the line $s(\lambda) := \hat{J}(\mathfrak{u}) + \lambda\gamma\nabla\hat{J}(\mathfrak{u})^T d$. From the Armijo rule the globally convergent Algorithm 1 is formulated [85].

Algorithm 1: The Armijo Rule Algorithm.
Input: $\beta_* \in (0,1)$, $\gamma \in (0,1)$, $\sigma > 0$, $k = 0$.
While $|\nabla\hat{J}(\mathfrak{u}^k)| > TOL$,

1. $d^k = -\sigma\nabla\hat{J}(\mathfrak{u}^k)$.
2. Determine the largest $\lambda \in \{1, \beta_*, {\beta_*}^2, \cdots,\}$ such that $\hat{J}(\mathfrak{u}^k + \lambda d^k) - \hat{J}(\mathfrak{u}^k) \leq \lambda\gamma\nabla\hat{J}(\mathfrak{u}^k)^T d^k$.
3. Set $\mathfrak{u}^{k+1} = \mathfrak{u}^k + \lambda d^k$, $k = k + 1$.

Reduced Armijo Algorithm

The challenge in the Armijo algorithm lies in the computation of $\hat{J}(\mathfrak{u}^k + \lambda d^k)$, representing the cost functional value for the *future* control $\mathfrak{u}^k + \lambda d^k$. To compute this value, the solution of the state equations is necessary. As each step length evaluation thus requires to solve the state equations, the computational effort is deemed to be unfeasible for industrial applications. Therefore, a *reduced* Armijo approach [18] is used, that lowers the computational costs of the Armijo rule evaluation. A similar approach is already presented in [87], applied to the quality optimization of crystal breeding. For the purpose of checking the Armijo condition, the state equations are solved on a coarse grid level. To be able to

do so, a coarse mesh is generated for each design update step involving geometrical modifications. The solver switches to the coarse case, solves the state equations for initial and modified design, checks the Armijo condition and states if the gradient step leads to an improvement. If not, the design update is not considered and the step size is reduced. The procedure repeats until a step size is found that fulfills the Armijo condition. Thereafter, the design is updated and the primal and adjoint equations are again solved on the fine mesh level. From the sensitivity, the gradient is computed and the procedure is repeated. The approach is illustrated in Figure 2.1.

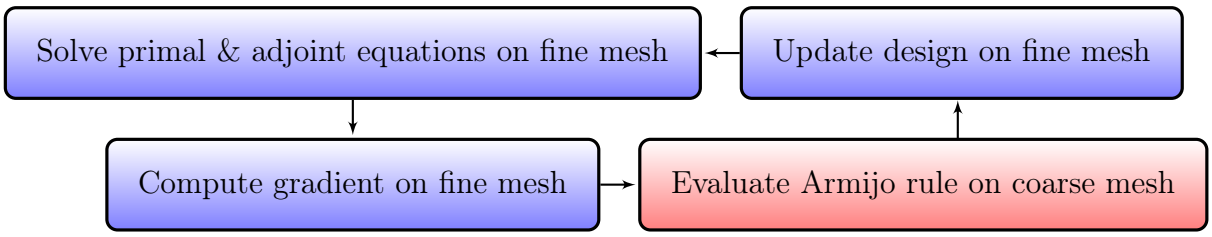

Fig. 2.1.: Reduced Armijo approach.

It is important to ensure that the coarse mesh is able to predict the change of the cost functional credibly. To this end, the mesh coarsening should be performed moderately. By applying this approach, the following targets are pursued in comparison to a non-reduced Armijo algorithm or a gradient method with constant step size:

- Perform bigger steps in the update procedure.
- Reduce the cost of a cost functional evaluation and therewith of the complete computation.
- Obtain a similar result concerning cost functional improvement and design modification.

The reduced Armijo approach may be used for shape and topology optimization, though, in case of shape optimization, the coarse mesh has to be recomputed for each design update step. This process step requires computational time and, advisably, the automation and integration of the mesh computation into the process chain. As, in the framework of this thesis, the prerequisites for an efficient performance of the presented approach for the shape optimization are not given, it is only performed for topology optimization. Here, the coarse mesh is only generated once and can be reused for each iteration step, as the control modification does not affect the mesh configuration.

3. Governing Fluid Dynamic Equations

In this chapter the state equations in the previously defined optimal control problem, namely the primal flow equations are characterized. At first, the RANS/RANS-F equations are described, including the governing equations for momentum, continuity and internal energy. A description of the porosity model for the topology-based optimization follows. The chapter closes with the specification of appropriate boundary conditions and cost functionals.

3.1. Navier-Stokes Equations

The incompressible, steady state Navier-Stokes equations read

$$\rho \frac{\partial}{\partial x_j} u_i u_j = -\frac{\partial p_*}{\partial x_i} + \frac{\partial}{\partial x_j}\left[\mu\left(\frac{\partial u_i}{\partial x_j} + \frac{\partial u_j}{\partial x_i}\right)\right] + f_i\,, \tag{3.1}$$

$$-\frac{\partial u_i}{\partial x_i} = 0\,, \tag{3.2}$$

on the computational domain Ω, with density ρ, dynamic viscosity μ, pressure p_*, and body force f_i. The Reynold-averaged velocity and pressure fields are computed by application of an average operation $\overline{(\cdot)}$, such that – due to the linearity property of the average operation [17] – it holds for the incompressible Reynolds-averaged Navier-Stokes equations

$$\rho \frac{\partial}{\partial x_j}\left(\overline{u_i' u_j'}\right) + \rho \frac{\partial}{\partial x_j}\left(\overline{u_i}\ \overline{u_j}\right) = -\frac{\partial \overline{p_*}}{\partial x_i} + \frac{\partial}{\partial x_j}\left[\mu\left(\frac{\partial \overline{u_i}}{\partial x_j} + \frac{\partial \overline{u_j}}{\partial x_i}\right)\right] + \overline{f_i}\,, \tag{3.3}$$

$$-\frac{\partial \overline{u_i}}{\partial x_i} = 0\,, \tag{3.4}$$

where u_i' denotes the fluctuating part of the velocity. The Reynolds-averaged Navier-Stokes equations are a non-closed system, i.e. there are more unknowns than equations. Merely the Reynolds stress tensor $\rho\overline{u_i' u_j'}$ consists of six unknown entries in 3D. According to the Boussinesq eddy-viscosity hypothesis [7], the deviatoric part of the Reynolds stress tensor is modeled proportional to the mean rate of strain,

$$-\rho\overline{u_i' u_j'} + \frac{2}{3}\rho k \delta_{ij} = 2\mu_t \overline{S_{ij}}\,, \tag{3.5}$$

with turbulent dynamic eddy viscosity μ_t and the Kronecker delta δ_{ij}. Hereby, the turbulent kinetic energy k is defined as half the trace of the Reynolds stress tensor,

$$k = \frac{1}{2}\overline{u_i' u_i'}\,. \tag{3.6}$$

The tensor S_{ij} denotes the rate-of-strain,

$$S_{ij} = \frac{1}{2}\left(\frac{\partial u_i}{\partial x_j} + \frac{\partial u_j}{\partial x_i}\right)\,. \tag{3.7}$$

For the sake of brevity, the notation of the Reynolds-average $\overline{(\cdot)}$ is omitted for the zeroth moments. Hence, under the predefined assumptions, the incompressible Reynolds-averaged Navier-Stokes equations read

$$\rho\frac{\partial}{\partial x_j}u_i u_j = -\frac{\partial p}{\partial x_i} + \frac{\partial}{\partial x_j}\left[\mu_e\left(\frac{\partial u_i}{\partial x_j} + \frac{\partial u_j}{\partial x_i}\right)\right] + f_i\,, \tag{3.8}$$

$$-\frac{\partial u_i}{\partial x_i} = 0\,, \tag{3.9}$$

where $p := p_* + \frac{2}{3}\rho k$ is regarded as modified mean pressure and $\mu_e = \mu + \mu_t$ marks the effective viscosity. A detailed derivation can be found, for example, in [67]. In the shear stress transport (SST) k-ω model, proposed by Menter and Esch in 2001 [56], the turbulent dynamic eddy viscosity μ_t in Equation (3.5) is computed by solving additional transport equations for turbulent kinetic energy k and specific dissipation rate ω,

$$\frac{\partial k}{\partial t} + u_j\frac{\partial k}{\partial x_j} = P_k - \beta^* k\omega + \frac{\partial}{\partial x_j}\left[(\nu + \sigma_k\nu_t)\frac{\partial k}{\partial x_j}\right]\,, \tag{3.10}$$

$$\frac{\partial \omega}{\partial t} + u_j\frac{\partial \omega}{\partial x_j} = \tilde{\alpha}S^2 - \tilde{\beta}\omega^2 + \frac{\partial}{\partial x_j}\left[(\nu + \sigma_\omega\nu_t)\frac{\partial \omega}{\partial x_j}\right] + 2(1-F_1)\sigma_{\omega 2}\frac{1}{\omega}\frac{\partial k}{\partial x_i}\frac{\partial \omega}{\partial x_i}\,, \tag{3.11}$$

with blending function F_1 and production term P_k. The turbulent kinematic eddy viscosity $\nu_t = \frac{\mu_t}{\rho}$ is basically computed from the ratio of k and ω, according to Equation (3.12),

$$\nu_t = \frac{a_1 k}{\max(a_1\omega, SF_2)}\,, \tag{3.12}$$

where S denotes the magnitude of the rate-of-strain tensor, i.e. $S = \sqrt{2S_{ij}S_{ij}}$, a_1 is a constant and F_2 is a second blending function. The coefficients ϕ of the model are functions of F_1, i.e. $\phi = F_1\phi_1 + (1-F_1)\phi_2$, where ϕ_1, ϕ_2 stand for the coefficients of the $k-\omega$ model:

$$\tilde{\alpha}_1 = 0.5532,\ \tilde{\alpha}_2 = 0.4403,\ \tilde{\beta}_1 = 0.075,\ \tilde{\beta}_2 = 0.0828$$
$$\sigma_{k1} = 0.85034,\ \sigma_{k2} = 1.0,\ \sigma_{\omega 1} = 0.5,\ \sigma_{\omega 2} = 0.85616\,.$$

The required constants of Equation (3.10)–(3.12), the definition of the blending functions F_1 and F_2 and production term P_k can be found in [56] and are given in Table 3.1.

Table 3.1.: Closure coefficients and auxiliary relations for SST k-ω model.

Symbol	Description	Value
P_k	production term	$\min\left(\tau_{ij}\frac{\partial u_i}{\partial x_j}, 10\beta^* k\omega\right)$
F_1	first blending function	$\tanh\left\{\left\{\min\left[\max\left(\frac{\sqrt{k}}{\beta^*\omega y}, \frac{500\nu}{y^2\omega}\right), \frac{4\sigma_{\omega 2}k}{CD_{k\omega}y^2}\right]\right\}^4\right\}$
F_2	second blending function	$\tanh\left[\left[\max\left(\frac{2\sqrt{k}}{\beta^*\omega y}, \frac{500\nu}{y^2\omega}\right)\right]^2\right]$
$CD_{k\omega}$	coefficient in blending function	$\max\left(2\sigma_{\omega 2}\frac{1}{\omega}\frac{\partial k}{\partial x_i}\frac{\partial \omega}{\partial x_i}, 10^{-10}\right)$
a_1	coefficient in eddy viscosity	0.31
β^*	coefficient in production term	0.09

Hereby, y denotes the wall distance.

3.2. Navier-Stokes-Fourier Equations

This section characterizes the internal energy equation, from which an equation for the temperature is derived. Later on, the internal energy equation is coupled to the momentum equation via the temperature-depending buoyancy term, which is inserted as a source term into the momentum equation.
The steady state transport equation for the internal energy $\mathcal{E}$ denotes

$$\frac{\partial}{\partial x_k}\left[\rho u_k \mathcal{E}\right] = -\frac{\partial q_i}{\partial x_i} - p\frac{\partial u_i}{\partial x_i} + 2\mu S_{ij}\frac{\partial u_i}{\partial x_j}\,, \tag{3.13}$$

with dissipation function $2\mu S_{ij}\frac{\partial u_i}{\partial x_j}$ and heat flux density q_i. Fourier's equation of state for an isotropic material with temperature T states

$$q_i = -\kappa\frac{\partial T}{\partial x_i}\,, \tag{3.14}$$

at which the thermal heat conductivity κ is employed to describe the heat flux density based upon a scalar heat conductivity. For incompressible fluids, the term $p\frac{\partial u_i}{\partial x_i}$ in Equation (3.13) vanishes. The relation $\mathcal{E} = c_v T$ is used for incompressible fluids with c_v being the isochore heat capacity, constant for a perfect fluid. By factoring out c_v, an equation for the temperature T is obtained,

$$\frac{\partial}{\partial x_k}\left[\rho u_k T\right] = \frac{\partial}{\partial x_i}\left[\frac{\kappa}{c_v}\frac{\partial T}{\partial x_i}\right] + \frac{2\mu}{c_v} S_{ij}\frac{\partial u_i}{\partial x_j}\,. \tag{3.15}$$

Equation (3.15) is also Reynolds-averaged to derive the governing equations for an averaged temperature $\overline{T}$ and its fluctuating part T', resulting in

$$\frac{\partial}{\partial x_k}\left[\rho\overline{u_k}\overline{T}\right] = \frac{\partial}{\partial x_i}\left[\frac{\kappa}{c_v}\frac{\partial \overline{T}}{\partial x_i}\right] + \frac{2\mu}{c_v}\overline{S_{ij}\frac{\partial u_i}{\partial x_j}} - \frac{\partial}{\partial x_k}\left[\rho\overline{u_k' T'}\right]\,. \tag{3.16}$$

The term $\rho\overline{u_k' T'}$ is interpreted as turbulent heat flux density and modeled analogously to the mean heat flux density,

$$\rho\overline{u_k' T'} = -\frac{\kappa_t}{c_v}\frac{\partial \overline{T}}{\partial x_k}\,, \tag{3.17}$$

with the turbulent thermal heat conductivity κ_t. The turbulent heat conductivity, κ_t, is computed from the ratio of μ_t, turbulent Prandtl number Pr_t and specific heat capacity c_p, viz.

$$\kappa_t = \frac{\mu_t c_p}{Pr_t}\,. \tag{3.18}$$

Equation (3.16) transforms to

$$\frac{\partial}{\partial x_k}\left[\rho\overline{u_k}\overline{T}\right] = \frac{\partial}{\partial x_i}\left[\kappa_e\frac{\partial \overline{T}}{\partial x_i}\right] + \frac{2\mu}{c_v}\overline{S_{ij}\frac{\partial u_i}{\partial x_j}}\,, \tag{3.19}$$

with effective thermal heat conductivity denoting the sum of turbulent and thermal heat conductivity, $\kappa_e := \frac{\kappa}{c_v} + \frac{\kappa_t}{c_v}$. For the term $S_{ij}\frac{\partial u_i}{\partial x_j}$ holds

$$\begin{aligned} S_{ij}\frac{\partial u_i}{\partial x_j} &= S_{ij}\underbrace{\frac{1}{2}\left(\frac{\partial u_i}{\partial x_j} + \frac{\partial u_j}{\partial x_i}\right)}_{S_{ij}} + S_{ij}\underbrace{\frac{1}{2}\left(\frac{\partial u_i}{\partial x_j} - \frac{\partial u_j}{\partial x_i}\right)}_{W_{ij}} \\ &= S_{ij}S_{ij} + S_{ij}W_{ij} = S_{ij}S_{ij}\,. \end{aligned} \tag{3.20}$$

Since the vorticity tensor W_{ij} is anti-symmetric, i.e. $W_{ij} = -W_{ji}$, and S_{ij} is symmetric, i.e. $S_{ij} = S_{ji}$, it follows $W_{ij}S_{ij} = 0$.

For the averaged dissipation term holds, by using Equation (3.20),

$$2\mu\overline{S_{ij}\frac{\partial u_i}{\partial x_j}} = 2\mu\overline{S_{ij}S_{ij}} = 2\mu\left(\overline{S_{ij}}\,\overline{S_{ij}}\right) + 2\mu\overline{\left(S'_{ij}S'_{ij}\right)}\,. \tag{3.21}$$

The turbulent dissipation rate $2\mu\overline{\left(S'_{ij}S'_{ij}\right)}$ is modeled analogously to the mean dissipation rate $2\mu\left(S_{ij}S_{ij}\right)$. Again, a turbulent eddy viscosity μ_t is employed, such that

$$2\mu\overline{\left(S'_{ij}S'_{ij}\right)} = 2\mu_t\left(\overline{S_{ij}}\,\overline{S_{ij}}\right) = 2\mu_t\overline{S_{ij}}\frac{\partial\overline{u_i}}{\partial x_j} \tag{3.22}$$

is obtained by using Equation (3.20). For the sake of brevity, the notation of the Reynolds-average $\overline{(\cdot)}$ is omitted.
In summary, the Reynolds-averaged internal energy equation denotes

$$\rho u_k\frac{\partial T}{\partial x_k} = \frac{\partial}{\partial x_i}\left[\kappa_e\frac{\partial T}{\partial x_i}\right] + \frac{2\mu_e}{c_v}S_{ij}\frac{\partial u_i}{\partial x_j}\,. \tag{3.23}$$

Hereby, the continuity equation (3.9) has been used. To couple the equations of momentum and energy, the buoyancy term $f_i = \rho\cdot g_i$ is inserted into the momentum equation as a driving force, with acceleration of gravity g_i.
The *Boussinesq approximation* relates the density in the buoyancy term to the change in temperature,

$$f_i = \rho\cdot g_i = \rho_{ref}\cdot\left(1-\beta_T(T-T_{ref})\right)\cdot g_i\,, \tag{3.24}$$

where β_T denotes the thermal expansion coefficient and T_{ref}, ρ_{ref} the reference temperature and density values. The buoyancy term linearly depends on the temperature difference. All other dependencies on the temperature change are of a higher order. Thus, in the sense of a first order approximation [30], all dependencies on the temperature difference, apart from the density in the buoyancy term, are neglected. The accuracy of the approach is only given for small temperature and density changes and differs from a compressible simulation where the density is explicitly computed and contributes to all other terms. Insertion of the buoyancy term (3.24) into the momentum equation (3.8) results in the Reynolds-averaged Navier-Stokes-Fourier equations,

$$\rho\frac{\partial}{\partial x_j}u_iu_j = -\frac{\partial p}{\partial x_i} + \frac{\partial}{\partial x_j}\left[\mu_e\left(\frac{\partial u_i}{\partial x_j}+\frac{\partial u_j}{\partial x_i}\right)\right] + \rho_{ref}\cdot\left(1-\beta_T(T-T_{ref})\right)\cdot g_i\,, \tag{3.25}$$

$$-\frac{\partial u_i}{\partial x_i} = 0, \tag{3.26}$$

$$\rho u_k\frac{\partial T}{\partial x_k} = \frac{\partial}{\partial x_i}\left[\kappa_e\frac{\partial T}{\partial x_i}\right] + \frac{2\mu_e}{c_v}S_{ij}\frac{\partial u_i}{\partial x_j}\,. \tag{3.27}$$

This system of equations governs the fluid flow, driven by the buoyancy force, which itself depends on the internal energy.

3.3. Darcy Porous Media Flow Model

Besides from a surface-normal displacement of the boundary, another control device, considered in this work, is the modification of the permeability of a porous medium. This section describes how the permeability is modeled.
The Darcy law [13] states that the total discharge $\dot{V}_i$, in units of volume per time, e.g. $\frac{\mathrm{m}^3}{\mathrm{s}}$, passing a porous medium of area A, is proportional to the pressure drop and a material specific constant k_f, the permeability,

$$\frac{\dot{V}_i}{A} = -k_f \frac{\partial p}{\partial x_i} \,. \tag{3.28}$$

Per division by the area A, the total discharge turns into a characteristic velocity. Equation (3.28) transforms to

$$u_i = -k_f \frac{\partial p}{\partial x_i} \,. \tag{3.29}$$

The Darcy term is employed by using the inverse of the permeability constant,

$$\alpha := \frac{1}{k_f} \,. \tag{3.30}$$

In conjunction with Equation (3.29), the Darcy law (3.28) is reformulated,

$$\alpha u_i = -\frac{\partial p}{\partial x_i} \,. \tag{3.31}$$

The Darcy law states, that the product of velocity and Darcy porosity term α is proportional to the pressure loss occurring when the fluid passes a porous medium. The larger α, the less fluid traverses the medium. The Darcy porosity term may thus be considered as a resistance coefficient. Controlling the inviscid pressure-driven forces, the Darcy term is inserted as a sink term in the momentum equation (3.8),

$$\rho \frac{\partial}{\partial x_j} u_i u_j = -\frac{\partial p}{\partial x_i} + \frac{\partial}{\partial x_j} \left[\mu_e \left(\frac{\partial u_i}{\partial x_j} + \frac{\partial u_j}{\partial x_i} \right) \right] - \alpha u_i + f_i \,, \tag{3.32}$$

$$-\frac{\partial u_i}{\partial x_i} = 0 \,. \tag{3.33}$$

Analogously, the Darcy term may be inserted into the momentum equations of the RANS-F equations (3.25). Modification of the Darcy term is the control device in the considered

topology optimization.

3.4. Boundary Conditions

To close the system of the RANS/RANS-F model, boundary and initial conditions are required. The section starts with the definition of the general boundary conditions before it concentrates on flows in HVAC systems. Additionally, boundary conditions for symmetry planes are stated.

Dirichlet Boundary Condition

The Dirichlet boundary condition may also be referred to as a fixed boundary condition,

$$\phi = D \quad \text{on} \quad \Gamma\,, \tag{3.34}$$

where ϕ is the flow variable and D a given constant. A homogeneous Dirichlet boundary condition imposes

$$\phi = 0 \quad \text{on} \quad \Gamma\,. \tag{3.35}$$

This boundary condition is also denoted as *no-slip* boundary condition.

Neumann Boundary Condition

The Neumann boundary condition specifies the normal derivative of the flow on the boundary of the domain,

$$\frac{\partial \phi}{\partial n} = D \quad \text{on} \quad \Gamma\,. \tag{3.36}$$

Boundary Conditions for Ducted Flows

The flows passing heating, ventilation and air-conditioning components typically involve ducted settings, bounded by inlet, outlet, and walls. Therefore, the commonly used boundary conditions for these types of flow in (virtually) incompressible fluids are stated.

Inlet

- Dirichlet boundary condition for the velocity, $\underline{u} = \underline{u}_{in}$.
- Homogeneous Neumann boundary condition for the pressure, $\frac{\partial p}{\partial n} = 0$.
- Dirichlet boundary condition for the temperature, $T = T_{in}$.

Outlet

- Homogeneous Neumann boundary condition for the velocity, $\frac{\partial u_i}{\partial n} = 0$.
- Homogeneous Dirichlet boundary condition for the pressure, $p = p_{out}$ (usually 0).
- Homogeneous Neumann boundary condition for the temperature, $\frac{\partial T}{\partial n} = 0$.

Wall

- Homogeneous Dirichlet boundary condition for the velocity, $u_i = 0$.
- Homogeneous Neumann boundary condition for the pressure, $\frac{\partial p}{\partial n} = 0$.
- Dirichlet boundary condition for the temperature, $T = T_w$ or prescribed heat flux, i.e. $-\frac{\partial T}{\partial x_i} = \frac{q_i}{\kappa}$.

Wall functions are used for turbulent flows by taking advantage of the well studied behavior of boundary layer flows [67]. The associated boundary conditions for the turbulence quantities k, ω and ν_t are given in Section 5.4.

Boundary Conditions for Symmetry Planes

The flow is symmetric to the symmetry plane, Γ_{sym}. Accordingly, the flow across symmetry planes is zero. Thus, normal vector flow components are assigned to zero and tangential vector flow components to zero gradient. The scalar flux across symmetry planes is zero, i.e. all scalar variables have zero normal gradients.

3.5. Fluid Dynamic Cost Functionals

This section describes the cost functionals for the optimization of HVAC components.

Desired State

The concerned cost functional models the difference of a flow variable from a desired state ϕ_d,

$$J = \int_\Gamma \frac{1}{2} \left(\phi\left(\underline{x}\right) - \phi_d\left(\underline{x}\right)\right)^2 d\Gamma \,. \tag{3.37}$$

When applied to the velocity at the outlet, Γ_{out}, this cost functional is denoted as *uniformity of the flow* at the outlet w.r.t. a desired velocity $\underline{u}_d$,

$$J = \int_{\Gamma_{out}} \frac{1}{2} \left(\underline{u} - \underline{u}_d\right)^2 d\Gamma \,. \tag{3.38}$$

A homogeneous outflow represents a critical issue in comfort optimization. If the cost functional is minimized, the velocity at the outlet is close to the desired velocity $\underline{u}_d$ and, thus, more homogeneous. To consider the tangential velocity at the outlet in the adjoint calculus, is crucial to detect recirculation zones.
In particular, the desired state may be referred to a desired temperature T_d,

$$J = \int_{\Gamma_{out}} \frac{1}{2}(T - T_d)^2 d\Gamma \,. \tag{3.39}$$

For a small value of the cost functional, the temperature differences become minimal, hence, the homogeneity of the temperature distribution is improved; consequently, the mixing in the domain increases. Therefore, this cost functional is also denoted as *mixing efficiency*.

Dissipated Power

The cost functional dissipated power describes the loss of kinetic energy and pressure through the device boundaries,

$$J = -\int_{\Gamma} \left(\frac{p}{\rho} + \frac{1}{2} u_i u_i \right) u_n d\Gamma \,. \tag{3.40}$$

A low value resembles a high system efficiency, preferred for industrial system devices.

4. Adjoint Fluid Dynamic Equations

The adjoint fluid dynamic equations, namely the incompressible adjoint RANS and the adjoint RANS-F equations, are derived from a variational approach. Furthermore, adjoint topology optimization involving the Darcy porosity term is considered. Additionally, constraints arising in the topology optimization are examined and the computation of the gradient from the sensitivity is described.

4.1. Adjoint Navier-Stokes Equations

In the optimal control theory, the primal state equations serve as constraints, which have to be satisfied. The optimal control problem (see Chapter 2), based on the steady RANS-equations and the surface normal shape control β, is given as

$$\begin{aligned} &\min_{(u_i,p,\beta)} J(u_i,p,\beta) \text{ subject to} \\ &\quad R_i = \frac{\partial}{\partial x_j}\left[\rho u_i u_j + \delta_{ij} p - \mu_e\left(\frac{\partial u_i}{\partial x_j} + \frac{\partial u_j}{\partial x_i}\right)\right] - f_i = 0\,, \\ &\quad Q = -\frac{\partial u_i}{\partial x_i} = 0\,. \end{aligned} \tag{4.1}$$

The Lagrangian function L is derived from the cost functional J and the residual Navier-Stokes equations $\mathcal{R} = (R_1, R_2, R_3, Q)$ by integration over the flow domain Ω and augmentation with Lagrange multipliers $(\hat{u}_i, \hat{p})$, denoting adjoint velocity $\hat{u}_i$ and adjoint pressure $\hat{p}$, respectively,

$$L = J + \int_\Omega (\hat{u}_i, \hat{p})\mathcal{R}\; d\Omega\,. \tag{4.2}$$

Following Chapter 2, the adjoint equations are computed from the variation of the Lagrangian function with respect to the state variables, as

$$\delta_u L + \delta_p L = \delta_u J + \delta_p J + \int_\Omega \left[(\hat{u}_i, \hat{p})\delta_u\mathcal{R} + (\hat{u}_i, \hat{p})\delta_p\mathcal{R}\right] d\Omega = 0\,. \tag{4.3}$$

Expansion of the local variation of the Lagrangian function (4.3) yields

$$\begin{aligned}
&\delta_u J + \delta_p J + \int_\Omega \left[(\hat{u}_i, \hat{p})\delta_u \mathcal{R} + (\hat{u}_i, \hat{p})\delta_p \mathcal{R}\right] d\Omega \\
=&\delta_u J + \delta_p J + \int_\Omega \left[\hat{u}_i \delta_u R_i + \hat{u}_i \delta_p R_i + \hat{p}\delta_u Q + \hat{p}\delta_p Q\right] d\Omega \\
=&\delta_u J + \delta_p J + \int_\Omega \left[\hat{u}_i \left(\rho \frac{\partial[\delta(u_i u_j)]}{\partial x_j} + \frac{\partial}{\partial x_j}\left[\delta_{ij}\delta p - \mu_e \left(\frac{\partial \delta u_i}{\partial x_j} + \frac{\partial \delta u_j}{\partial x_i}\right)\right]\right) - \hat{p}\frac{\partial \delta u_i}{\partial x_i}\right] d\Omega \,.
\end{aligned} \tag{4.4}$$

Each integrand is transformed by using integration by parts. Equation (4.5) can then be derived for the local variation of the Lagrangian function

$$\begin{aligned}
&\oint_\Gamma \left[\rho\left(\delta u_i u_j + \delta u_j u_i\right)\hat{u}_i + (\delta u_i) 2\mu_e \hat{S}_{ij} - \mu_e \left(\frac{\partial \delta u_i}{\partial x_j} + \frac{\partial \delta u_j}{\partial x_i}\right)\hat{u}_i + (\delta p)\,\hat{u}_j - (\delta u_j)\,\hat{p}\right] n_j d\Gamma \\
&+ \int_\Omega \left[\left(-2\rho u_j \hat{S}_{ij} - \frac{\partial}{\partial x_j}\left(2\mu_e \hat{S}_{ij} - \delta_{ij}\hat{p}\right)\right)\delta u_i - \frac{\partial \hat{u}_i}{\partial x_i}\delta p\right] d\Omega \\
&+ \int_\Omega \delta_u j_\Omega d\Omega + \int_\Gamma \delta_u j_\Gamma d\Gamma + \int_\Omega \delta_p j_\Omega d\Omega + \int_\Gamma \delta_p j_\Gamma d\Gamma = 0\,,
\end{aligned} \tag{4.5}$$

with $\hat{S}_{ij}$ representing the adjoint complement to the rate-of-strain tensor S_{ij}, n_j the outward pointing normal vector and j_Ω and j_Γ the cost functional integrands declared on Ω and Γ, respectively. A detailed derivation of Equation (4.5) is given in Appendix B. Note that the *frozen turbulence* approach is used, i.e. $\delta\mu_e = 0$. Approaches to involve variations of this term are found, for example, in [88]. The term, contained in Equation (4.5),

$$\oint_\Gamma \hat{u}_i \rho u_i \delta u_j n_j d\Gamma - \int_\Omega \rho u_j \frac{\partial \hat{u}_j}{\partial x_i}\delta u_i d\Omega\,, \tag{4.6}$$

is called *advection* in this work, analogously to [78], and may be represented in different ways. The additional integration by parts (see Appendix B, Equation (B.3)), followed in this work, is also pursued by Othmer [60] and leads, correspondingly, to the term (4.6), consisting of a volume and a boundary integral. An alternative formulation follows from omitting the additional partial integration, leading to a modified volume term in (4.6) and no boundary term. This approach is pursued, for example, by [31], [11] or [78]. Neglecting the advection term, as suggested by [74] can stabilize the numerical solution as the advection may lead to numerical instabilities in the adjoint computations.
A suitable choice of the Lagrange multipliers cancels the terms in Equation (4.5) that depend on local flow variations and results in the adjoint equations. This approach ensures the independence of local flow variations. Note that the equations are specific to the chosen cost functional, due to the cost functional integrands in Equation (4.5).

Treatment of the Volume Terms

The adjoint volume equations are obtained from the volume integrals in Equation (4.5), by requiring the contributions depending on the local flow variations to vanish, leading to

$$-2\rho u_j \hat{S}_{ij} = \frac{\partial}{\partial x_j}\left(2\mu_e \hat{S}_{ij} - \hat{p}\delta_{ij}\right) - \frac{\partial j_\Omega}{\partial u_i} \qquad \text{in } \Omega_{obj}\,, \tag{4.7}$$

$$-2\rho u_j \hat{S}_{ij} = \frac{\partial}{\partial x_j}\left(2\mu_e \hat{S}_{ij} - \hat{p}\delta_{ij}\right) \qquad \text{in } \Omega \setminus \Omega_{obj}\,, \tag{4.8}$$

$$\frac{\partial \hat{u}_i}{\partial x_i} = \frac{\partial j_\Omega}{\partial p} \qquad \text{in } \Omega_{obj}\,, \tag{4.9}$$

$$\frac{\partial \hat{u}_i}{\partial x_i} = 0 \qquad \text{in } \Omega \setminus \Omega_{obj}\,, \tag{4.10}$$

where Ω_{obj} denotes the part of the volume at which the cost function is defined. Hereby, it is used that for the volume integral containing the cost functional holds

$$\int_\Omega \delta_u j_\Omega d\Omega + \int_\Omega \delta_p j_\Omega d\Omega = \int_\Omega \left(\frac{\partial j_\Omega}{\partial u_i}\delta u_i + \frac{\partial j_\Omega}{\partial p}\delta p\right) d\Omega\,. \tag{4.11}$$

Treatment of the Boundary Terms

The adjoint boundary conditions are obtained from the boundary terms in Equation (4.5), by requiring the contributions depending on local flow variations to vanish, leading to

$$\oint_\Gamma \delta u_i \left[\rho u_j \hat{u}_i n_j + \rho u_j \hat{u}_j n_i + 2\mu_e \hat{S}_{ij} n_j - \hat{p} n_i + \frac{\partial j_\Gamma}{\partial u_i}\right] d\Gamma - \oint_\Gamma \hat{u}_i \mu_e \left(\frac{\partial \delta u_i}{\partial x_j} + \frac{\partial \delta u_j}{\partial x_i}\right) n_j d\Gamma = 0\,, \tag{4.12}$$

$$\oint_\Gamma \delta p \left(\hat{u}_j n_j + \frac{\partial j_\Gamma}{\partial p}\right) d\Gamma = 0\,, \tag{4.13}$$

expressing the local variation of the cost functional as

$$\oint_\Gamma \delta_u j_\Gamma d\Gamma + \oint_\Gamma \delta_p j_\Gamma d\Gamma = \oint_\Gamma \left(\frac{\partial j_\Gamma}{\partial u_i}\delta u_i + \frac{\partial j_\Gamma}{\partial p}\delta p\right) d\Gamma\,. \tag{4.14}$$

This is the general form of the adjoint equation system for the steady state, incompressible Navier- Stokes equations with frozen turbulence. Compared to the primal equation system, the convection term in the adjoint system is linear in nature. The crucial difference between primal and adjoint equations is the minus sign in front of the convective term in Equation (4.12) and the advective contribution. For cost functionals defined on the surface of the domain only, the adjoint flow field is divergence-less. The general form of the adjoint volume and boundary terms is now specialized to ducted flows, the considered setting in this work.

Additionally, symmetry planes and the related adjoint boundary conditions are considered.

Specialization to Ducted Flows

The adjoint volume and boundary equations for ducted flows are deduced, by making the following assumptions [60]:

1. The flow boundary domain Γ is made up of three portions – inlet, outlet and wall – with prescribed velocity and zero pressure gradient at the inlet and along the wall, and zero velocity gradient and prescribed pressure at the outlet.

2. As outlined in Section 3.5, the considered objective functions of ducted flows usually involve integrals over the surface of the flow domain and not in its interior (the only exception in this work appears in Section 7.4). Usually, the surface-declared cost functionals apply to the flow quantities at inlet and outlet and *not* at the wall.

3. The gradient of the effective viscosity μ_e is assumed to be of second order and is therefore neglected.

4. The only portion of Γ subject to shape variations is the wall.

Due to the second assumption, the volume equations in (4.7)–(4.10) reduce to

$$-2\rho u_j \hat{S}_{ij} = \frac{\partial}{\partial x_j}\left(2\mu_e \hat{S}_{ij} - \hat{p}\delta_{ij}\right), \tag{4.15}$$

$$\frac{\partial \hat{u}_i}{\partial x_i} = 0\,, \tag{4.16}$$

on the computational domain Ω. Note that the adjoint volume equations do not directly depend on the cost functional any more. For surface-declared cost functionals, the dependency is shifted to the adjoint boundary conditions.
Elaboration on the terms of the boundary conditions (4.12), involving the rate-of-strain tensor, under consideration of the third assumption, leads to

$$\oint_\Gamma \left(\delta u_j 2\mu_e \hat{S}_{ij} n_i - \hat{u}_j \mu_e \left(\frac{\partial \delta u_i}{\partial x_j} + \frac{\partial \delta u_j}{\partial x_i}\right) n_i\right) d\Gamma = \oint_\Gamma \mu_e n_i \left(\frac{\partial \hat{u}_j}{\partial x_i}\delta u_j - \frac{\partial \delta u_j}{\partial x_i}\hat{u}_j\right) d\Gamma\,. \tag{4.17}$$

A detailed computation of this transformation is confined in the Appendix, (B.11)-(B.13). Therefore, the boundary integrals (4.12) and (4.13) reduce to

$$\oint_\Gamma \delta u_i \left[\rho u_j \hat{u}_i n_j + \rho u_j \hat{u}_j n_i + \mu_e n_j \frac{\partial \hat{u}_i}{\partial x_j} - \hat{p} n_i + \frac{\partial j_\Gamma}{\partial u_i}\right] d\Gamma - \oint_\Gamma \mu_e n_i \frac{\partial \delta u_j}{\partial x_i}\hat{u}_j d\Gamma = 0\,, \tag{4.18}$$

$$\oint_\Gamma \delta p \left(\hat{u}_j n_j + \frac{\partial j_\Gamma}{\partial p}\right) d\Gamma = 0\,. \tag{4.19}$$

These conditions are evaluated for Dirichlet, Neumann and symmetry boundary conditions to deduce the appropriate adjoint boundary conditions.

Dirichlet Boundary Condition

The Dirichlet boundary condition imposes a constant value for the flow variable, viz. $\phi = D$ along the boundary, Γ. As this condition is also imposed for the varied flow,

$$\delta\phi = 0 \tag{4.20}$$

is valid at Dirichlet boundaries concerning the variation with respect to the state.

Neumann Boundary Conditions

For this type of boundary condition, the normal gradient of the flow is assigned to zero or a fixed value. As this condition is also valid for the variation of the flow,

$$\frac{\partial\delta\phi}{\partial n} = 0 \tag{4.21}$$

is valid at Neumann boundaries for the variation with respect to the state.
Inlet and **wall** boundaries have a Dirichlet-type boundary condition for the primal velocity. Thus, according to (4.20) the variation is zero,

$$\delta u_i = 0\,, \tag{4.22}$$

and, therefore, the first integral of (4.18) vanishes. The continuity equation for δu reduces to

$$\frac{\partial\delta u_n}{\partial n} = 0\,. \tag{4.23}$$

So the boundary equations (4.18) and (4.19) reduce to

$$\oint_\Gamma \mu_e \frac{\partial\delta u_{i(t)}}{\partial n}\hat{u}_{i(t)}\; d\Gamma = 0\,, \tag{4.24}$$

$$\oint_\Gamma \delta p\left(\hat{u}_j n_j + \frac{\partial j_\Gamma}{\partial p}\right) d\Gamma = 0\,. \tag{4.25}$$

Hereby, $u_{i(t)}$ and $\hat{u}_{i(t)}$ denote the primal and adjoint tangential velocity, respectively. Out of this, the adjoint boundary conditions for inlet and wall boundaries are deduced, namely

$$\underline{\hat{u}}_t = 0\,, \tag{4.26}$$

$$\hat{u}_n = -\frac{\partial j_\Gamma}{\partial p}\,. \tag{4.27}$$

As the considered objective functions are not declared at the wall, (4.26) and (4.27) are conflated to the adjoint velocity boundary condition at the wall, namely

$$\hat{u}_i = 0 \ . \tag{4.28}$$

There is not yet a condition for the adjoint pressure at wall and inlet. As the adjoint pressure $\hat{p}$ enters the adjoint Navier-Stokes equations similar to its primal counterpart, the zero gradient boundary condition for p at wall and inlet is applied for $\hat{p}$ as well, to assure the well-posedness of the adjoint equation system [60]. Therefore, it holds for the adjoint pressure at wall and inlet

$$\frac{\partial \hat{p}}{\partial n} = 0 \, . \tag{4.29}$$

At the **outlet**, the Dirichlet-type boundary condition is imposed for the primal pressure, i.e. $p = p_{out}$. As this condition is also valid for the local variation of the pressure (4.20), Equation (4.30) is valid along the outlet, Γ_{out},

$$\delta p = 0 \, . \tag{4.30}$$

Consequently, Equation (4.19) is fulfilled. At the outlet the Neumann boundary condition is imposed for the primal velocity. Accordingly, it holds for δu_i,

$$\frac{\partial \delta u_i}{\partial n} = 0 \, , \tag{4.31}$$

and the second integral of (4.18) vanishes. Hence, the integrand of the first integral of Equation (4.18) has to vanish, viz.

$$\rho u_n \hat{u}_i + \rho u_j \hat{u}_j n_i + \mu_e \frac{\partial \hat{u}_i}{\partial n} - \hat{p} n_i + \frac{\partial j_\Gamma}{\partial u_i} = 0 \, . \tag{4.32}$$

Decomposition into tangential and normal parts yields

$$\rho u_n \hat{u}_n + \rho u_i \hat{u}_i + \mu_e \frac{\partial \hat{u}_n}{\partial n} - \hat{p} + \frac{\partial j_\Gamma}{\partial u_n} = 0 \, , \tag{4.33}$$

$$\rho \hat{u}_{i(t)} u_n + \mu_e \frac{\partial \hat{u}_{i(t)}}{\partial n} + \frac{\partial j_\Gamma}{\partial u_{i(t)}} = 0 \, . \tag{4.34}$$

Therefore, the adjoint boundary conditions for the outlet read

$$\hat{p} = \rho u_n \hat{u}_n + \rho u_i \hat{u}_i + \mu_e \frac{\partial \hat{u}_n}{\partial n} + \frac{\partial j_\Gamma}{\partial u_n} \, , \tag{4.35}$$

$$0 = \rho \hat{u}_{i(t)} u_n + \mu_e \frac{\partial \hat{u}_{i(t)}}{\partial n} + \frac{\partial j_\Gamma}{\partial u_{i(t)}} \, . \tag{4.36}$$

The adjoint normal velocity component at the outlet is determined from the adjoint continuity equation, balanced over wall, inlet and outlet. In conjunction with the value of $\hat{u}_n$ from the previous iteration and the values at the other boundary faces, the current value for the normal adjoint velocity component is adjusted such that the mass balance over the boundaries is maintained.

Symmetry Plane

For the tangential flow a zero gradient boundary condition is assumed; the normal flow component is zero. If this holds for the varied flow field at the initial boundary, one can set

$$\frac{\partial \delta\phi_{i(t)}}{\partial n} = 0 \quad \text{and} \quad \delta\phi_n = 0\,, \tag{4.37}$$

on Γ_{sym}. If this boundary condition is imposed for the primal velocity and $j_\Gamma = 0$ holds on the symmetry plane Γ_{sym}, the adjoint boundary conditions (4.18) and (4.19) reduce to

$$\oint_\Gamma \delta u_{i(t)} \mu_e \frac{\partial \hat{u}_{i(t)}}{\partial n} d\Gamma - \oint_\Gamma \mu_e \frac{\partial \delta u_n}{\partial n} \hat{u}_n d\Gamma = 0\,, \tag{4.38}$$

$$\oint_\Gamma \delta p \hat{u}_n d\Gamma = 0\,, \tag{4.39}$$

leading to the adjoint boundary conditions at symmetry planes, equivalent to the primal boundary conditions,

$$\frac{\partial \hat{u}_{i(t)}}{\partial n} = 0\,, \tag{4.40}$$

$$\hat{u}_n = 0\,. \tag{4.41}$$

For the adjoint pressure, a zero gradient boundary condition is imposed.

Adjoint RANS Equations

The adjoint Navier-Stokes equations and boundary conditions for ducted flows are summarized as follows,

$$-2\rho u_j \hat{S}_{ij} = \frac{\partial}{\partial x_j}\left(2\mu_e \hat{S}_{ij} - \hat{p}\delta_{ij}\right) \qquad \text{on} \quad \Omega\,, \tag{4.42}$$

$$\frac{\partial \hat{u}_i}{\partial x_i} = 0 \qquad \text{on} \quad \Omega\,, \tag{4.43}$$

$$\hat{u_i} = 0 \qquad \text{on } \Gamma_w\,, \tag{4.44}$$

$$\frac{\partial \hat{p}}{\partial n} = 0 \qquad \text{on } \Gamma_w\,, \tag{4.45}$$

$$\underline{\hat{u}_t} = 0 \qquad \text{on } \Gamma_{in}\,, \tag{4.46}$$

$$\hat{u_n} = -\frac{\partial j_\Gamma}{\partial p} \qquad \text{on } \Gamma_{in}\,, \tag{4.47}$$

$$\frac{\partial \hat{p}}{\partial n} = 0 \qquad \text{on } \Gamma_{in}\,, \tag{4.48}$$

$$\hat{p} = \rho u_n \hat{u}_n + \rho u_i \hat{u}_i + \mu_e \frac{\partial \hat{u}_n}{\partial n} + \frac{\partial j_\Gamma}{\partial u_n} \qquad \text{on } \Gamma_{out}\,, \tag{4.49}$$

$$0 = \rho \hat{u}_{i(t)} u_n + \mu_e \frac{\partial \hat{u}_{i(t)}}{\partial n} + \frac{\partial j_\Gamma}{\partial u_{i(t)}} \qquad \text{on } \Gamma_{out}\,. \tag{4.50}$$

Computation of Surface Sensitivity

The Lagrangian function leads to the adjoint Navier-Stokes equations (4.42)–(4.50), eliminating the dependency on local flow variations. The sensitivity is computed from the variation w.r.t. the control, according to Equation (2.33),

$$\delta_\beta L = \delta_\beta J + \int_\Omega \left[\hat{u}_i \delta_\beta R_i + \hat{p} \delta_\beta Q\right] d\Omega\,. \tag{4.51}$$

As the only portion of Γ that is subject to shape variations is the wall and the cost functional is assumed to be defined on inlet and outlet, it follows that the variations of the cost function w.r.t. β vanish and, therefore,

$$\delta_\beta J = 0\,. \tag{4.52}$$

The remaining term is computed by using Equation (2.34), namely

$$\delta_\beta L = \int_\Omega \left[\hat{u}_i \delta_\beta R_i + \hat{p} \delta_\beta Q\right] d\Omega = -\int_\Omega \left[\hat{u}_i \delta_u R_i + \hat{p} \delta_u Q + \hat{u}_i \delta_p R_i + \hat{p} \delta_p Q\right] d\Omega\,, \tag{4.53}$$

assuming that the total variation of the residual Navier-Stokes equations vanishes. The right-hand side has already been derived via the variational approach (4.5). Supposing that the cost functional applies to the boundaries only, the volume integrals cancel, satisfying the adjoint volume equations in (4.42) and (4.43). Thus, only the boundary terms of Equation (4.5) are taken over, omitting the cost functional contributions, such that the right-hand side of Equation (4.53) transforms to

$$-\oint_\Gamma \left[\rho \left(\delta u_i u_j + \delta u_j u_i\right) \hat{u}_i + \delta u_i 2\mu_e \hat{S}_{ij} - \mu_e \left(\frac{\partial \delta u_i}{\partial x_j} + \frac{\partial \delta u_j}{\partial x_i}\right) \hat{u}_i + \delta p \hat{u}_j - \delta u_j \hat{p}\right] n_j d\Gamma\,. \tag{4.54}$$

As the shape control β only applies to the wall boundary, Equation (4.54) reduces to the wall. Due to the zero boundary condition for $\hat{u}_i$ (4.44), the majority of Equation (4.54) cancels. The variations δp and δu_i are computed according to Equation (2.30) and (2.31), by a Taylor series expansion. Therefore, Equation (4.54) transforms to

$$\delta_\beta L = -\oint_{\Gamma_w} \delta\beta \frac{\partial u_i}{\partial n} \left[2\mu_e \hat{S}_{ij} n_j - \hat{p} n_i \right] d\Gamma \,. \tag{4.55}$$

Due to the primal and adjoint continuity equation and $\underline{u}_t = 0$ such as $\underline{\hat{u}}_t = 0$ along the wall, Equation (4.23) follows analogously for the primal and adjoint velocity, i.e.

$$\frac{\partial u_n}{\partial n} = 0 \,, \tag{4.56}$$

$$\frac{\partial \hat{u}_n}{\partial n} = 0 \,. \tag{4.57}$$

As $\hat{u}_n = 0$ along the wall,

$$\frac{\partial \hat{u}_n}{\partial t} = 0 \,. \tag{4.58}$$

With these considerations, Equation (4.55) transforms to

$$\delta_\beta L = \oint_{\Gamma_w} \left[-\mu_e \delta\beta \frac{\partial u_{i(t)}}{\partial n} \frac{\partial \hat{u}_{i(t)}}{\partial n} \right] d\Gamma \,. \tag{4.59}$$

The sensitivity, G_L, follows accordingly, viz.

$$G_L = \frac{\partial L}{\partial \beta} = \oint_{\Gamma_w} \left[-\mu_e \frac{\partial u_{i(t)}}{\partial n} \frac{\partial \hat{u}_{i(t)}}{\partial n} \right] d\Gamma = -\mu_e \frac{\partial u_{i(t)}}{\partial n} \frac{\partial \hat{u}_{i(t)}}{\partial n} \Delta\Gamma_w \,, \tag{4.60}$$

in which the area of the considered wall patch is denoted as $\Delta\Gamma_w$. The surface sensitivity is thus obtained from the product of primal and adjoint surface normal gradients. Hence, only the solution of the primal and adjoint equation systems is required irrespective of the number of design parameters.

4.2. Adjoint Navier-Stokes-Fourier Equations

This section is concerned with the coupled system of energy and momentum equations for the adjoint calculus. The derivation is analogous to the adjoint Navier-Stokes equations in the preceding section. Similar approaches can be found, for example, in [53] and [57]. The

optimal control problem for the RANS-F equations (3.25)–(3.27) is formulated as

$$\min_{(u_i,p,T,\beta)} J(u_i,p,T,\beta) \text{ subject to}$$

$$R_i = \frac{\partial}{\partial x_j}\left[\rho u_i u_j + \delta_{ij} p - 2\mu_e S_{ij}\right] - \rho_{ref}\cdot(1-\beta_T(T-T_{ref}))\cdot g_i = 0\,, \tag{4.61}$$

$$Q = -\frac{\partial u_i}{\partial x_i} = 0\,, \tag{4.62}$$

$$H = \rho\frac{\partial}{\partial x_j}(u_j T) - \frac{\partial}{\partial x_j}\left[\kappa_e\frac{\partial T}{\partial x_j}\right] - \frac{2\mu_e}{c_v}S_{ij}\frac{\partial u_i}{\partial x_j} = 0\,, \tag{4.63}$$

where H denotes the residual form of the internal energy equation (3.27). The Lagrangian function L is derived from the cost functional and the residual Navier-Stokes-Fourier equations $\mathcal{R} = (R_1, R_2, R_3, Q, H)$ by multiplication with Lagrange multipliers, $\hat{u}_i$, $\hat{p}$ and $\hat{T}$, in which $\hat{T}$ denotes the adjoint temperature, and integration over the flow domain Ω, such that

$$L := J + \int_\Omega (\hat{u}_i, \hat{p}, \hat{T})\mathcal{R}\; d\Omega\,. \tag{4.64}$$

The adjoint equations are derived from the variation of the Lagrangian function with respect to the state variables,

$$\begin{aligned}&\delta_u L + \delta_p L + \delta_T L = \\ &\delta_u J + \delta_p J + \delta_T J + \int_\Omega \left[(\hat{u}_i,\hat{p},\hat{T})\delta_u\mathcal{R} + (\hat{u}_i,\hat{p},\hat{T})\delta_p\mathcal{R} + (\hat{u}_i,\hat{p},\hat{T})\delta_T\mathcal{R}\right] d\Omega = 0\,.\end{aligned} \tag{4.65}$$

Using integration by parts, the local variation of the Lagrangian function results in

$$\begin{aligned}\delta L = &\oint_\Gamma \left[\rho\left(\delta u_i u_j + \delta u_j u_i\right)\hat{u}_i + \delta u_i 2\mu_e\hat{S}_{ij} - \mu_e\left(\frac{\partial\delta u_i}{\partial x_j} + \frac{\partial\delta u_j}{\partial x_i}\right)\hat{u}_i + \delta p\hat{u}_j - \delta u_j\hat{p}\right] n_j d\Gamma \\ &+ \oint_\Gamma \left[\rho\hat{T}u_j\delta T - \kappa_e\hat{T}\frac{\partial\delta T}{\partial x_j} + \kappa_e\delta T\frac{\partial\hat{T}}{\partial x_j} - \delta u_i\hat{T}\frac{2\mu_e}{c_v}\left(\frac{\partial u_i}{\partial x_j} + \frac{\partial u_j}{\partial x_i}\right)\right] n_j d\Gamma \\ &+ \int_\Omega \left\{\left[-2\rho u_j\hat{S}_{ij} - \frac{\partial}{\partial x_j}\left(2\mu_e\hat{S}_{ij} - \delta_{ij}\hat{p}\right) + \rho\hat{T}\frac{\partial T}{\partial x_i} + \frac{\partial}{\partial x_j}\left(\frac{2\mu_e}{c_v}\left(\frac{\partial u_i}{\partial x_j} + \frac{\partial u_j}{\partial x_i}\right)\hat{T}\right)\right]\delta u_i \right. \\ &\left. + \left[-\rho u_j\frac{\partial\hat{T}}{\partial x_j} - \frac{\partial}{\partial x_j}\left[\kappa_e\frac{\partial\hat{T}}{\partial x_j}\right] + \hat{u}_i\,\rho_{ref}\,g_i\,\beta_T\right]\delta T - \frac{\partial\hat{u}_i}{\partial x_i}\delta p\right\} d\Omega + (\delta_u + \delta_p + \delta_T)J\,,\end{aligned} \tag{4.66}$$

utilizing the results from the preceding section (4.5) for the local variation of the momentum and continuity equations. The detailed computation of the variational formulation of the internal energy equation and the buoyancy term is given in the Appendix B.

Treatment of the Volume Terms

The adjoint field equations are obtained from the volume integrals of Equation (4.66), resulting in the following set of equations

$$-2\rho u_j \hat{S}_{ij} - \frac{\partial}{\partial x_j}\left(2\mu_e \hat{S}_{ij} - \delta_{ij}\hat{p}\right) + \rho\hat{T}\frac{\partial T}{\partial x_i} + \frac{\partial}{\partial x_j}\left(\frac{2\mu_e}{c_v}\left(\frac{\partial u_i}{\partial x_j} + \frac{\partial u_j}{\partial x_i}\right)\hat{T}\right) = -\frac{\partial j_\Omega}{\partial u_i}\,, \tag{4.67}$$

$$\frac{\partial \hat{u}_i}{\partial x_i} = \frac{\partial j_\Omega}{\partial p}\,, \tag{4.68}$$

$$-\rho u_j \frac{\partial \hat{T}}{\partial x_j} - \frac{\partial}{\partial x_j}\left[\kappa_e \frac{\partial \hat{T}}{\partial x_j}\right] + \hat{u}_i \cdot \rho_{ref} \cdot g_i \cdot \beta_T = -\frac{\partial j_\Omega}{\partial T}\,, \tag{4.69}$$

where the cost functional only applies to the part of the domain carrying the objective functional, i.e. $j_\Omega = 0 \quad \text{on} \quad \Omega \setminus \Omega_{obj}$.

Treatment of the Boundary Terms

Analogously to the previous section, the boundary condition for the adjoint temperature is formulated from the corresponding boundary integrals of Equation (4.66), leading to

$$\oint_\Gamma \left(\delta T\left(\rho\hat{T}u_n + \kappa_e\frac{\partial\hat{T}}{\partial n} + \frac{\partial j_\Gamma}{\partial T}\right) - \kappa_e\left(\hat{T}\frac{\partial\delta T}{\partial x_j}\right)n_j - \delta u_i\hat{T}\frac{2\mu_e}{c_v}\left(\frac{\partial u_i}{\partial x_j} + \frac{\partial u_j}{\partial x_i}\right)n_j\right)d\Gamma{=}0\,. \tag{4.70}$$

Consideration of the primal boundary conditions leads to the corresponding boundary conditions for the adjoint temperature.
At **inlet** and **wall** the Dirichlet boundary condition is imposed for the primal temperature, i.e. $T = D$. This condition also applies to the perturbed flow at the initial boundary (cf. (4.20)), therefore,

$$\delta T = 0. \tag{4.71}$$

From the surface integral (4.70) remains

$$-\oint_\Gamma \left(\kappa_e\left(\hat{T}\frac{\partial\delta T}{\partial x_j}\right)n_j - \delta u_i\hat{T}\frac{2\mu_e}{c_v}\left(\frac{\partial u_i}{\partial x_j} + \frac{\partial u_j}{\partial x_i}\right)n_j\right)d\Gamma = 0\,. \tag{4.72}$$

Equation (4.72) requires to choose the boundary condition for $\hat{T}$, viz.

$$\hat{T} = 0\,. \tag{4.73}$$

At the **outlet** the homogeneous Neumann boundary condition is imposed for the temperature. This condition also applies to the disturbed flow at the initial boundary. Therefore,

$$\frac{\partial \delta T}{\partial n} = 0\,. \tag{4.74}$$

So the second term of the surface integrals (4.70) vanishes. Due to the homogeneous Neumann boundary condition for u_i, the third term of Equation (4.70) is rewritten as follows,

$$-\oint_\Gamma \delta u_i \hat{T} \frac{2\mu_e}{c_v} \left(\frac{\partial u_i}{\partial x_j} + \frac{\partial u_j}{\partial x_i} \right) n_j d\Gamma = -\oint_\Gamma \delta u_{i(t)} \hat{T} \frac{2\mu_e}{c_v} \left(\frac{\partial u_n}{\partial t} \right) d\Gamma. \tag{4.75}$$

The term in Equation (4.75) is related to the variation in tangential direction and is thus assumed to be negligible. The remaining integrand of Equation (4.70) is

$$\rho \hat{T} u_n + \kappa_e \frac{\partial \hat{T}}{\partial n} + \frac{\partial j_\Gamma}{\partial T} = 0\,, \tag{4.76}$$

and thus defines the outlet boundary condition for the temperature.

Symmetry Plane

Analogously to the primal temperature, a zero gradient boundary condition holds for the variation of the temperature on Γ_{sym}, namely

$$\frac{\partial \delta T}{\partial n} = 0\,. \tag{4.77}$$

So the second term of the surface integrals (4.70) vanishes. For the term of Equation (4.70) depending on δu, it holds, due to the corresponding zero boundary condition for δu_n, the zero gradient boundary condition for $\underline{u}_t$ and zero value for u_n along Γ_{sym},

$$-\oint_\Gamma \delta u_i \hat{T} \frac{2\mu_e}{c_v} \left(\frac{\partial u_i}{\partial x_j} + \frac{\partial u_j}{\partial x_i} \right) n_j d\Gamma = -\oint_\Gamma \delta u_{i(t)} \hat{T} \frac{2\mu_e}{c_v} \left(\frac{\partial u_{i(t)}}{\partial n} + \frac{\partial u_n}{\partial t} \right) d\Gamma = 0\,. \tag{4.78}$$

The remaining integrand of Equation (4.70) is

$$\rho \hat{T} u_n + \kappa_e \frac{\partial \hat{T}}{\partial n} + \frac{\partial j_\Gamma}{\partial T} = 0\,, \tag{4.79}$$

which reduces to

$$\kappa_e \frac{\partial \hat{T}}{\partial n} = 0\,, \tag{4.80}$$

due to $j_\Gamma = 0$ and $u_n = 0$ on Γ_{sym}. The adjoint boundary condition is derived from Equation (4.80) as

$$\frac{\partial \hat{T}}{\partial n} = 0\,, \tag{4.81}$$

analogous to the primal symmetry boundary condition.

Adjoint RANS-F Equations

The adjoint RANS-F equations are summarized, assuming that $\Omega_{obj} = \emptyset$,

$$-2\rho u_j \hat{S}_{ij} - \frac{\partial}{\partial x_j}\left[2\mu_e \hat{S}_{ij} - \delta_{ij}\hat{p}\right] + \rho\hat{T}\frac{\partial T}{\partial x_i} + \frac{\partial}{\partial x_j}\,\frac{4\mu_e}{c_v}\left(S_{ij}\hat{T}\right) = 0 \qquad \text{on } \Omega\,, \tag{4.82}$$

$$\frac{\partial \hat{u}_i}{\partial x_i} = 0 \qquad \text{on } \Omega\,, \tag{4.83}$$

$$-u_j\rho\frac{\partial \hat{T}}{\partial x_j} - \frac{\partial}{\partial x_j}\left[\kappa_e\frac{\partial \hat{T}}{\partial x_j}\right] + \hat{u}_i \cdot \rho_{ref} \cdot g_i \cdot \beta_T = 0 \qquad \text{on } \Omega\,, \tag{4.84}$$

$$\hat{T} = 0 \qquad \text{on } \Gamma_w\,, \tag{4.85}$$

$$\hat{u}_i = 0 \qquad \text{on } \Gamma_w\,, \tag{4.86}$$

$$\frac{\partial \hat{p}}{\partial n} = 0 \qquad \text{on } \Gamma_w\,, \tag{4.87}$$

$$\hat{T} = 0 \qquad \text{on } \Gamma_{in}\,, \tag{4.88}$$

$$\underline{\hat{u}}_t = 0 \qquad \text{on } \Gamma_{in}\,, \tag{4.89}$$

$$\hat{u}_n + \frac{\partial j_\Gamma}{\partial p} = 0 \qquad \text{on } \Gamma_{in}\,, \tag{4.90}$$

$$\frac{\partial \hat{p}}{\partial n} = 0 \qquad \text{on } \Gamma_{in}\,, \tag{4.91}$$

$$\rho u_i \hat{u}_i + \rho u_n \hat{u}_n + \mu_e\frac{\partial \hat{u}_n}{\partial n} + \frac{\partial j_\Gamma}{\partial u_n} = \hat{p} \qquad \text{on } \Gamma_{out}\,, \tag{4.92}$$

$$\rho\hat{u}_{i(t)}u_n + \mu_e\frac{\partial \hat{u}_{i(t)}}{\partial n} + \frac{\partial j_\Gamma}{\partial u_{i(t)}} = 0 \qquad \text{on } \Gamma_{out}\,, \tag{4.93}$$

$$\rho\hat{T}u_n + \kappa_e\frac{\partial \hat{T}}{\partial n} + \frac{\partial j_\Gamma}{\partial T} = 0 \qquad \text{on } \Gamma_{out}\,. \tag{4.94}$$

Computation of Surface Sensitivity

To obtain the sensitivity equation for the coupled system, the variation of the Lagrangian function with respect to the control is computed analogously to Equation (2.33), namely

$$\delta_\beta L = \delta_\beta J + \int_\Omega \left[\hat{u}_i \delta_\beta R_i + \hat{p} \delta_\beta Q + \hat{T} \delta_\beta H \right] d\Omega \,. \tag{4.95}$$

As before, $\delta_\beta J$ cancels, as the cost functional is not defined on the boundary parts that are subject to shape variations. As in the previous section, the variation δ_β is computed from the local variation, according to (2.34), such that

$$\delta_\beta L = - \int_\Omega \left[(\hat{u}_i, \hat{p}, \hat{T}) \delta_u \mathcal{R} + (\hat{u}_i, \hat{p}, \hat{T}) \delta_p \mathcal{R} + (\hat{u}_i, \hat{p}, \hat{T}) \delta_T \mathcal{R} \right] d\Omega \,. \tag{4.96}$$

The right-hand side is already displayed in Equation (4.66). Assuming that no cost functional contributions exist in the volume, the volume integrals cancel, due to the satisfaction of the adjoint volume equations (4.82)–(4.84). Thus, only the boundary terms of Equation (4.66) are taken over, leaving out the cost functional contributions, such that Equation (4.96) transforms to

$$\begin{aligned} \delta_\beta L = &- \oint_\Gamma \left[\rho \left(\delta u_i u_j + \delta u_j u_i \right) \hat{u}_i + \delta u_i 2 \mu_e \hat{S}_{ij} - \mu_e \left(\frac{\partial \delta u_i}{\partial x_j} + \frac{\partial \delta u_j}{\partial x_i} \right) \hat{u}_i + \delta p \hat{u}_j - \delta u_j \hat{p} \right] n_j d\Gamma \\ &- \oint_\Gamma \left[\rho \hat{T} u_j \delta T - \kappa_e \hat{T} \frac{\partial \delta T}{\partial x_j} + \kappa_e \delta T \frac{\partial \hat{T}}{\partial x_j} - \delta u_i \hat{T} \frac{2 \mu_e}{c_v} \left(\frac{\partial u_i}{\partial x_j} + \frac{\partial u_j}{\partial x_i} \right) \right] n_j d\Gamma \,. \end{aligned} \tag{4.97}$$

The remaining part of (4.97) is confined to the wall, as $\delta\beta = 0$ on inlet and outlet. In conjunction with the homogeneous Dirichlet wall boundary condition for the adjoint velocity (4.86) and temperature (4.85), Equation (4.97) reduces to

$$\delta_\beta L = - \oint_{\Gamma_w} \left[\delta u_i 2 \mu_e \hat{S}_{ij} - \delta u_j \hat{p} \right] n_j d\Gamma - \oint_{\Gamma_w} \kappa_e \delta T \frac{\partial \hat{T}}{\partial x_j} n_j d\Gamma \,. \tag{4.98}$$

The first term has already been considered in the previous section (4.55), therefore the focus is on the second term of Equation (4.98). Again, δT is approximated by using a Taylor series expansion,

$$\delta T = \delta \beta \frac{\partial T}{\partial n} \,. \tag{4.99}$$

In conjunction with the sensitivity from the RANS equations (4.59), the cost functional derivative is expressed, viz.

$$\delta_\beta L = \oint_{\Gamma_w} -\delta\beta \left(\mu_e \frac{\partial u_{i(t)}}{\partial n} \frac{\partial \hat{u}_{i(t)}}{\partial n} + \kappa_e \frac{\partial T}{\partial n} \frac{\partial \hat{T}}{\partial n} \right) d\Gamma \,, \tag{4.100}$$

and, therefore, for the sensitivity

$$\frac{\partial L}{\partial \beta} = \oint_{\Gamma_w} - \left(\mu_e \frac{\partial u_{i(t)}}{\partial n} \frac{\partial \hat{u}_{i(t)}}{\partial n} + \kappa_e \frac{\partial T}{\partial n} \frac{\partial \hat{T}}{\partial n} \right) d\Gamma = - \left(\mu_e \frac{\partial u_{i(t)}}{\partial n} \frac{\partial \hat{u}_{i(t)}}{\partial n} + \kappa_e \frac{\partial T}{\partial n} \frac{\partial \hat{T}}{\partial n} \right) \Delta\Gamma_w \,. \tag{4.101}$$

Just like for the RANS-equations, solving primal and adjoint RANS-F equations leads to the sensitivity without the necessity to modifiy each design parameter.

4.3. Adjoint Navier-Stokes Equations and Darcy Term

Topology optimization is already a well established technique for design optimization in structural mechanics w.r.t. tension or stiffness [3]. However, its transfer to fluid dynamics has just begun in 2003 by Borrvall and Petersson [6]. Since then, the method has experienced a wide range of applications [61], [52], [63]. In the context of topology optimization, it is distinguished between cells supportive and cells counterproductive for the reduction of a cost functional. Cells supportive for the cost functional stay fluid, whereas cells counterproductive for the cost functional turn solid by increasing the porosity which is modeled by a Darcy term 3.3. Again, from the Lagrange function a set of adjoint equations and the sensitivity are derived to judge the effect of each cell on the cost functional. Restricting the interest to fluid dynamic aspects, the governing set of equations consists of the incompressible RANS equations including the Darcy term as a source term (3.32), (3.33). The corresponding optimal control problem denotes

$$\begin{aligned}
&\min_{(u_i,p,\alpha)} \; J(u_i,p,\alpha) \;\text{ subject to} \\
&R_i = \frac{\partial}{\partial x_j}\left[\rho u_i u_j + \delta_{ij} p - \mu_e \left(\frac{\partial u_i}{\partial x_j} + \frac{\partial u_j}{\partial x_i} \right)\right] + \alpha u_i - f_i \;\; = 0 \,, \\
&Q = -\frac{\partial u_i}{\partial x_i} \qquad\qquad\qquad\qquad\qquad\qquad\qquad\qquad\quad = 0 \,, \\
&\alpha_{min} \leq \alpha \leq \alpha_{max} \,,
\end{aligned} \tag{4.102}$$

in which the Darcy porosity term, α, is bounded by α_{min} and α_{max}, and $\mathcal{R} = (R_1, R_2, R_3, Q)$ denote the residual Navier-Stokes equations including the Darcy term. According to Equation (2.25), the adjoint equations are derived from the variation of the Lagrange function

with respect to the state variables, viz.

$$\delta_p L + \delta_u L = \delta_u J + \delta_p J + \int_\Omega \left[(\hat{u}_i, \hat{p})\delta_u \mathcal{R} + (\hat{u}_i, \hat{p})\delta_p \mathcal{R}\right] d\Omega = 0\,. \tag{4.103}$$

In the preceding section, the variational formulation of the Navier-Stokes volume equations (4.5) has already been derived. The only additional term in the variational formulation of the porosity model (3.32) and (3.33) is the Darcy term,

$$\int_\Omega \hat{u}_i \alpha \delta u_i d\Omega\,. \tag{4.104}$$

By factoring out δu_i, one obtains the adjoint Darcy contribution to the adjoint momentum, related to δu_i, (4.42)

$$\int_\Omega \hat{u}_i \alpha d\Omega\,. \tag{4.105}$$

In conjunction with the adjoint momentum (4.42) and continuity equations (4.43), the adjoint system including the Darcy term reads

$$-2\rho u_j \hat{S}_{ij} = \frac{\partial}{\partial x_j}\left(2\mu_e \hat{S}_{ij} - \hat{p}\delta_{ij}\right) - \alpha \hat{u}_i\,, \tag{4.106}$$

$$\frac{\partial \hat{u}_i}{\partial x_i} = 0\,. \tag{4.107}$$

Appropriate boundary conditions complete the set of primal and adjoint equation systems, according to Section 3.4 and Equation (4.44)–(4.50). The sensitivity is computed from the variation w.r.t. the control α, according to Equation (2.26),

$$\delta_\alpha L = \delta_\alpha J + \delta_\alpha \int_\Omega (\hat{u}_i, \hat{p})\mathcal{R}\; d\Omega\,. \tag{4.108}$$

The porosity is just an auxiliary variable to describe a continuous transition from fluid to solid; usually there is no explicit dependence of the cost functional on the porosity, i.e.

$$\frac{\partial J}{\partial \alpha} = 0\,. \tag{4.109}$$

Therefore, Equation (4.108) simplifies to

$$\delta_\alpha L = \delta_\alpha \int_\Omega (\hat{u}_i, \hat{p})\mathcal{R}\; d\Omega = \int_\Omega \hat{u}_i \frac{\partial R_i}{\partial \alpha}\delta\alpha\; d\Omega = \int_\Omega \hat{u}_i u_i \delta\alpha\; d\Omega\,. \tag{4.110}$$

Finally, the desired sensitivity is obtained from

$$\frac{\partial L}{\partial \alpha} = \int_{\Omega} \hat{u}_i u_i d\Omega \,. \tag{4.111}$$

From solving the primal and adjoint equations the volume sensitivity is easily computed as the product of primal and adjoint velocity and the related volume. Algorithm 2 summarizes the required steps of the topology optimization design cycle.

Algorithm 2: Porosity Optimization Design Cycle.

1. Solve the primal RANS equations including the Darcy term (3.32) and (3.33).
2. Solve the adjoint RANS equations including the Darcy term (4.106) and (4.107).
3. Compute the sensitivity from primal and adjoint flow fields (4.111).
4. Update the porosity of each control cell via a gradient descent step (see Section 2.5).

The design update is performed as *one-shot approach* [61, 84]. In this approach, the adjoint iteration and a gradient step for the design variable are integrated into the primal iteration. The approach benefits from less required computational time. Because the optimization process is directly integrated in the simulation, these methods are often called simultaneous analysis and design (SAND) or all-at-once approach [26].

4.4. Constrained Topology Optimization

This section deals with the realization of constraints with regard to the porosity distribution in the topology optimization approach. The modified porosity distribution is the result of the topology optimization and should ideally conform with a specific porous media, representing the realizable or desired porosity distribution. The porous material may for example represent a hole plate which is often used as a flow restrictor in HVAC systems. Therefore, a constant porosity value is often demanded inside a specific zone.
For some applications it has to be decided which parts of the domain turn completely solid and which parts stay fluid. As intermediate porosity values are not realizable for such applications, a digital porosity distribution is preferred, requiring the porosity to be either maximal or minimal. Moreover, if the production of solid material is related to costs, a reduced amount of control, i.e. a sparse porosity distribution, might be preferred. In the following, the constraints, significant for industrial applicability and economy, are summarized:

- Porosity constant within a porous zone

- Digital porosity distribution, i.e. porosity term takes either maximum or minimum value on each porous zone

- Sparse porosity distribution, i.e. a low amount of porosity

Approaches to realize these constraints are described in the following paragraphs.

Constant Porosity Term within a Porous Zone

Related to this constraint, the porosity value is only defined on a disjoint set of porous zones within the domain Ω,

$$\mathcal{L} := \{L^i \subset \Omega\,, i = 1, \cdots, l \mid L^i \cap L^j = \emptyset \quad \text{for} \quad i \neq j\}\,. \tag{4.112}$$

Additionally, the porosity value is required to be constant on each porous zone L^j. Therefore, a mapping $\alpha_{\mathcal{L}}$ is defined (see also [18]),

$$\begin{aligned} &\alpha_{\mathcal{L}} : \mathcal{L} \to \mathbb{R}^l\,, \\ &\alpha_{\mathcal{L}}\left(L^j\right) := \alpha^j\,, \quad \alpha^j \in \mathbb{R}, \quad j = 1, \cdots, l\,, \end{aligned} \tag{4.113}$$

satisfying the demand of constant porosity values within each porous region. The mapping $\alpha_{\mathcal{L}}$ applies to a set of porous zones $\mathcal{L}$, whereas the velocity u_i is defined on each cell of the domain Ω. To combine $\alpha_{\mathcal{L}}$ and u_i to the source term in the momentum equation, it is required to embed $\alpha_{\mathcal{L}}$ in the space of functions defined on Ω via an embedding function E,

$$\begin{aligned} &E : \mathcal{F}(\mathcal{L}, \mathbb{R}^l) \to \mathcal{F}(\Omega, \mathbb{R}^n) \\ &E\left(\alpha_{\mathcal{L}}\right)(x) =: \alpha_\Omega(x) = \sum_{j=1,\cdots,l} \alpha^j \chi_{L^j}(x)\,, \end{aligned} \tag{4.114}$$

in which $\mathcal{F}$ denotes the function space, χ_{L^j} is the characteristic function on the porous zone L^j and $x \in \Omega$. In practice, this means

$$\alpha_\Omega(x) = E(\alpha_{\mathcal{L}})(x) = \begin{cases} \alpha^j & \text{for } x \in L^j\,, \\ 0 & \text{else}\,. \end{cases} \tag{4.115}$$

The term $E(\alpha_{\mathcal{L}})u_i = \alpha_\Omega u_i$ is inserted as a source term into the momentum equation, resulting in the equation system

$$\frac{\partial}{\partial x_j}\rho u_i u_j + \frac{\partial p}{\partial x_i} - \frac{\partial}{\partial x_j}\left[\mu_e\left(\frac{\partial u_i}{\partial x_j} + \frac{\partial u_j}{\partial x_i}\right)\right] + E(\alpha_{\mathcal{L}})u_i - f_i = 0\,, \tag{4.116}$$

$$\frac{\partial u_i}{\partial x_i} = 0\,. \tag{4.117}$$

The adjoint RANS equations, including the embedded Darcy term, read analogously

$$-2\rho u_j \hat{S}_{ij} = \frac{\partial}{\partial x_j}\left(2\mu_e \hat{S}_{ij} - \hat{p}\delta_{ij}\right) - E(\alpha_{\mathcal{L}})\hat{u}_i\,, \tag{4.118}$$

$$\frac{\partial \hat{u}_i}{\partial x_i} = 0\,. \tag{4.119}$$

The sensitivity is computed from

$$\delta_{\alpha_{\mathcal{L}}} L = \delta_{\alpha_{\mathcal{L}}} J + \delta_{\alpha_{\mathcal{L}}} \int_\Omega \left[\hat{u}_i \frac{\partial R_i}{\partial \alpha_{\mathcal{L}}} + \hat{p}\frac{\partial Q}{\partial \alpha_{\mathcal{L}}}\right]\, d\Omega\,. \tag{4.120}$$

As before, no explicit dependence of the cost functional on the porosity is assumed, i.e.

$$\frac{\partial J}{\partial \alpha_{\mathcal{L}}} = 0\,. \tag{4.121}$$

The porosity enters the primal equation only via the embedded Darcy term, $E(\alpha_{\mathcal{L}})u_i$. Therefore, it holds, by using (4.113) and (4.114), for each porous zone L^j,

$$\frac{\partial L}{\partial \alpha_{\mathcal{L}^j}} = \int_{L^j} \hat{u}_i \frac{\partial E(\alpha_{\mathcal{L}}(L^j))u_i}{\partial \alpha_{\mathcal{L}}(L^j)} dL^j = \sum_{P\in L^j} \hat{u}_i^{(P)} \frac{\partial(\alpha^j u_i^{(P)})}{\partial \alpha^j} V^{(P)} = \sum_{P\in L^j} \hat{u}_i^{(P)} u_i^{(P)} V^{(P)}\,. \tag{4.122}$$

From solving the primal and adjoint equations, the topological sensitivity is easily computed for each porous zone L^j as volume weighted average value of the dot product of primal and adjoint velocities.

Sparse/Digital Porosity Distribution

A digital distribution of the control is required to decide whether it is favorable to turn a porous zone solid or to leave it fluid. Therefore, after the optimization, either the porosity value should be minimum, corresponding to fluid media, or maximum, corresponding to solid material. Several approaches apply to the insertion of additional functions into the cost functional to penalize intermediate porosity values, for example, performed in [5]. A strategy to achieve a sparse distribution of the control by insertion of an L^1-regularization term into the cost functional is presented in [76]. Generally, the L^1-regularization term is used to recover nonsmooth data, for example in the context of noise removal from images [69]. In [76] the sparse control distribution, i.e. the optimal controls are identical zero on large parts of the control domain, enables to decide *where* to put control devices for applications, in which one cannot put control devices all over the control domain. In this context, the sparse control distribution can be regarded as a selection of important regions as the control is identically zero in regions, where it is not able to decrease the cost functional significantly. This application resembles the demand of a digital distribution, as the decision where to put control comes close to an on/off-structure. Therefore, the

approach is to obtain a digital porosity distribution out of the sparsity. Additionally, a sparse distribution of the porosity is preferred, as the production of solid material is related to costs. Following [76], an L^1-norm regularization term of the control is added to the optimal control problem,

$$\begin{aligned} &\min_{(u_i,p,\alpha)} \left[J(u_i,p,\alpha) + \epsilon||\alpha||_{L^1(\Omega)}\right] \\ &\mathcal{R} = 0\,, \\ &\alpha_{min} \leq \alpha \leq \alpha_{max}\,, \end{aligned} \tag{4.123}$$

with weighting factor $\epsilon > 0$ and $||\cdot||_{L^1(\Omega)}$, the norm belonging to the Lebesgue space $L^1(\Omega)$ of integrable functions (see Appendix A). The problem with the insertion of the L^1-term,

$$||\alpha||_{L^1(\Omega)} = \int_\Omega |\alpha| \; d\Omega\,, \tag{4.124}$$

is, that the cost functional is no longer differentiable. But, to conduct a steepest descent approach, the gradient of the cost functional has to be computed, making the differentiability of the cost functional indispensable. As a remedy, instead of inserting the L^1-regularization term into the cost functional, a differentiable approximation of this term is utilized. In this way, the absolute value function in the L^1-norm (4.124) is approached by *Huber functions* [34, 8], defined as

$$\begin{aligned} &\Phi_\zeta : \mathbb{R} \to \mathbb{R} \\ &\Phi_\zeta(\alpha) = \begin{cases} \frac{\alpha^2}{2\zeta} & \text{if} \quad |\alpha| < \zeta\,, \\ |\alpha| - \frac{\zeta}{2} & \text{if} \quad |\alpha| \geq \zeta\,, \end{cases} \end{aligned} \tag{4.125}$$

with $\zeta \in \mathbb{R},\ \zeta > 0$, such that the optimal control problem (4.123) becomes

$$\begin{aligned} &\min_{(u_i,p,\alpha)} \left[J(u_i,p,\alpha) + \epsilon \int_\Omega \Phi_\zeta(\alpha) d\Omega\right] \\ &\mathcal{R} = 0\,, \\ &\alpha_{min} \leq \alpha \leq \alpha_{max}\,. \end{aligned} \tag{4.126}$$

The parameter ζ controls the accuracy, viz.

$$|\alpha| - \frac{\zeta}{2} \leq \Phi_\zeta(\alpha) \leq |\alpha|\,. \tag{4.127}$$

Figure 4.1 illustrates how the Huber function approximates the absolute value function for different values of ζ.
Using this approach, the parameters ϵ and ζ have to be determined. The greater ϵ, the more influence lies on the regularization term, leading to a sparser distribution. Ideally, the weighting factor ϵ is chosen such that the cost functional is close to a local minimum while the sparsity is guaranteed. The value of ϵ may be computed as a function of ζ such that

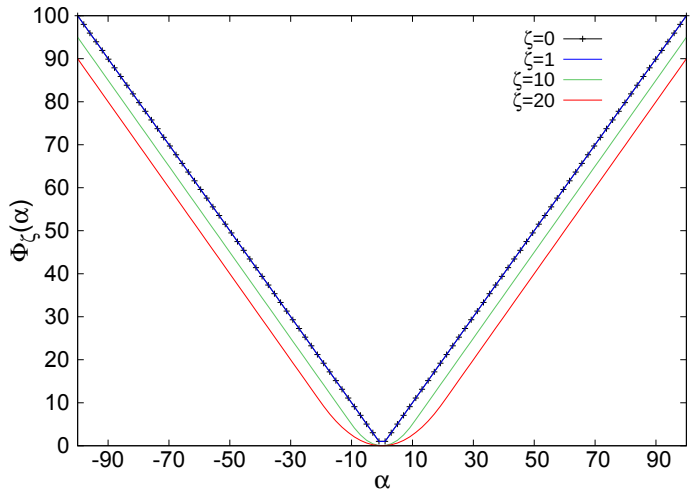

Fig. 4.1.: Absolute value function ($\zeta = 0$) compared to Huber function for different values of ζ.

both terms in the cost functional have the same order of magnitude on the objective region. The parameter ζ is chosen as a function of α_{max} and the required accuracy (4.127). The sensitivity controls the sparsity via the supplementary term arising from the approximated L^1-regularization term,

$$\frac{\partial \Phi_\zeta(\alpha)}{\partial \alpha} = \begin{cases} \frac{\alpha}{\zeta} & \text{if} \quad |\alpha| < \zeta \,, \\ \text{sign}(\alpha) & \text{if} \quad |\alpha| \geq \zeta \,. \end{cases} \tag{4.128}$$

4.5. Gradient Computation

While in the preceding sections the computation of the adjoint sensitivity has been described, this section deals with the computation of the gradient from the sensitivity. In this context, it is distinguished between volume and surface sensitivities.

Gradient Computation from Surface Sensitivities

The sensitivity is in the dual space of the control space (see Section 2.2). Therefore, for updates of the control, the sensitivity is unsuitable, unless the dual space is identical with the control space. Nevertheless, a common approach is to directly use the sensitivity for the update step in the gradient descent approach, which is incorrect from a mathematical point of view. Therefore, the gradient of the cost functional is required, located in the control space. The gradient $G(\beta)$ is computed from the surface sensitivity $\delta_\beta L = \hat{J}'(\beta)$, using the following definition

$$G\,(\beta) := \mathfrak{R}(\hat{J}'(\beta))\,. \tag{4.129}$$

$\mathfrak{R}(J'(\beta))$ denotes the Riesz representative (see Appendix A). To compute the Riesz representative, the control space U in which the gradient $G(\beta)$ is located is crucial to define the appropriate scalar and inner product. According to [86], a suitable choice is $\beta \in H^1(\Gamma)$, in which $H^1(\Gamma)$ denotes the Sobolev space of weakly differentiable functions over Γ with the scalar product

$$(\phi, \varphi)_{H^1(\Gamma)} := \int_\Gamma \left[\phi\varphi + \underline{\nabla}_\Gamma \phi \cdot \underline{\nabla}_\Gamma \varphi\right] d\Gamma \,, \tag{4.130}$$

representing a Hilbert space. The symbol $\underline{\nabla}_\Gamma$ denotes the tangential gradient,

$$\underline{\nabla}_\Gamma \phi := \underline{\nabla}\phi - (\underline{\nabla}\phi \cdot \underline{n})\,\underline{n} \,, \tag{4.131}$$

equivalent to a tangential projection of the gradient by subtraction of the normal component. The derivative $\hat{J}'(\beta)$ is only defined for $\beta \in \mathcal{C}^k(\Gamma, \mathbb{R})$. With the theorem of Hahn-Banach [1], $\hat{J}'$ can be extended onto $H^1(\Gamma)$, equipping $\mathcal{C}^k(\Gamma, \mathbb{R})$ with the norm of $H^1(\Gamma)$. From the Riesz representation theorem (see Appendix A), it follows for the gradient

$$(G(\beta), \phi)_{H^1(\Gamma)} = \langle \hat{J}'(\beta), \phi \rangle_{H^{-1}(\Gamma), H^1(\Gamma)} \text{ for all } \phi \in H^1(\Gamma) \,. \tag{4.132}$$

By inserting the scalar product (4.130), Equation (4.132) transforms to

$$\int_\Gamma \left[G\left(\beta\right)\phi + \underline{\nabla}_\Gamma G\left(\beta\right) \cdot \underline{\nabla}_\Gamma \phi\right] d\Gamma = \langle \hat{J}'\left(\beta\right), \phi \rangle \,. \tag{4.133}$$

The gradient $G(\beta)$ is supposed to be an element of $C^1(\Gamma, \mathbb{R})$. Integration by parts yields

$$\int_\Gamma \underline{\nabla}_\Gamma G\left(\beta\right) \cdot \underline{\nabla}_\Gamma \phi d\Gamma = -\int_\Gamma \Delta_\Gamma G(\beta)\phi d\Gamma + \int_{\partial\Gamma} \phi \underline{\nabla}_\Gamma G(\beta) \cdot t d\partial\Gamma \,. \tag{4.134}$$

The operator $\Delta_\Gamma := \underline{\nabla}_\Gamma \cdot \underline{\nabla}_\Gamma$ is denoted as *Laplace-Beltrami operator*. The boundary terms of Equation (4.134) vanish, as either Neumann or Dirichlet boundary conditions are considered, meaning that either $\underline{\nabla}_\Gamma G(\beta) \cdot t$ or ϕ vanish on $\partial\Gamma$. So, Equation (4.133) becomes

$$\int_\Gamma \left(G(\beta) - \Delta_\Gamma G\left(\beta\right)\right) \phi d\Gamma = \langle \hat{J}'(\beta), \phi \rangle \,. \tag{4.135}$$

The dual pairing in Equation (4.135) is rewritten as

$$\langle \hat{J}'(\beta), \phi \rangle = \int_\Gamma \mathcal{K}(\beta)\ \phi d\Gamma \,, \tag{4.136}$$

with a smooth function $\mathcal{K}(\beta)$. Therefore, Equation (4.135) becomes

$$\int_\Gamma \left(G\left(\beta\right) - \Delta_\Gamma G\left(\beta\right)\right) \phi d\Gamma = \int_\Gamma \mathcal{K}\left(\beta\right)\ \phi d\Gamma \,, \tag{4.137}$$

resulting in the Laplace-Beltrami equation,

$$G(\beta) - \Delta_\Gamma G(\beta) = \mathcal{K}(\beta) \ , \tag{4.138}$$

with $\mathcal{K}(\beta)$ corresponding to the integrand of the surface sensitivity G_L, Equation (4.60) and (4.101), respectively.

Gradient Computation from Volume Sensitivities

As in the previous section, the Riesz representative of the sensitivity is computed,

$$G(\alpha) := \mathfrak{R}\left(\hat{J}'(\alpha)\right) . \tag{4.139}$$

As the Darcy porosity term is bounded by α_{min} and α_{max}, it holds $\alpha \in L^2(\Omega)$ where $L^2(\Omega)$ denotes the Lebesgue space of square-integrable functions, that is also a Hilbert space (see Appendix A). Then the Riesz representation theorem (see Appendix A) becomes

$$\left(G(\alpha), \phi\right)_{L^2(\Omega)} = \langle \hat{J}'(\alpha), \phi \rangle_{L^2(\Omega), L^2(\Omega)} = \left(\hat{J}'(\alpha), \phi\right)_{L^2(\Omega)} \text{ for all } \phi \in L^2(\Omega) \ , \tag{4.140}$$

as for $L^2(\Omega)$ the dual space equals the primal space [1]. Thus, the sensitivity equals the gradient, $G(\alpha) = \hat{J}'(\alpha)$, and may directly be used for the gradient descent. The same holds for the porosity optimization on a set of porous zones $\mathcal{L}$ (see Section 4.4), as the porosity function $\alpha_\Omega \in L^2(\Omega)$.

5. Finite Volume Discretization

This chapter presents the numerical method for the solution of the primal and adjoint equations, namely the finite volume method. Discretization schemes for the physical terms of the state equations are described. Accordingly, suitable discretization schemes for the adjoint equations are derived. Subsequently, the arising algebraic equation system is given and numerical solution methods are presented.

5.1. Spatial Discretization

The spatial discretization converts the computational domain into a finite number of control volumes V, also denoted as computational cells. The amount of control volumes builds up the computational mesh. Using a cell centered scheme, each cell contains a computational point P in which the flow variables are stored, located in the centroid of the cell. A number of cell faces f bounds each control volume. Here, it is distinguished between boundary faces, located at the boundary of the domain, and internal faces. Each face is assigned an adjacent owner cell P and neighbor cell N. Boundary faces are only assigned one adjacent cell, being the owner cell by definition. A face area vector ${A_i}^{(f)}$ is related to each face, pointing outwards from the owner cell, being normal to the face and holding a magnitude equal to the area of the face. Face values are related to the midpoints of the faces.
It is discriminated between orthogonal and non-orthogonal meshes. Non-orthogonal meshes have two characteristics, which differentiates them from orthogonal meshes, that have to be considered in the spatial discretization.

- The connecting vector $\vec{PN}$ does not lie in the face center. This property has a consequence for the reconstruction of face values from cell center values.
- The connecting vector $\vec{PN}$ and the surface normal vector ${A_i}^{(f)}$ are not parallel. This property is of importance for the approximation of surface normal gradients.

Figure 5.1 illustrates the discretization model for orthogonal and non-orthogonal meshes. Concerning the element configuration, computational meshes may generally be divided into two types: **Structured meshes** are characterized by regular connectivity. The possible element choices are hexahedrons in 3D. **Unstructured meshes** are characterized by irregular connectivity, allowing for any possible element. Compared to structured meshes, this model calls for a face based data structure with an explicit storage of neighborhood relationships. These grids typically employ polyhedrons in 3D. Figure 5.2 illustrates structured and unstructured meshes.

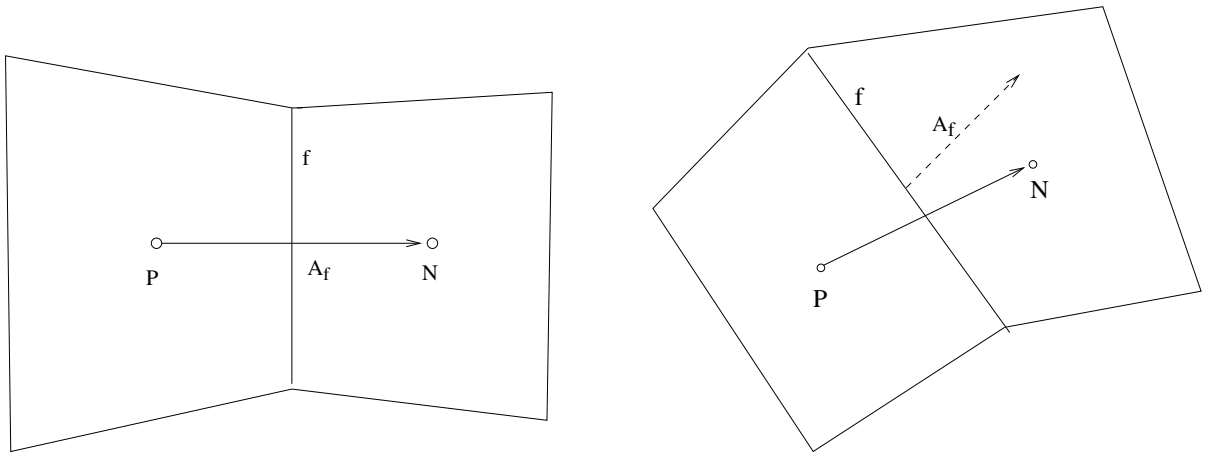

Fig. 5.1.: Orthogonal mesh (left) and non-orthogonal mesh (right).

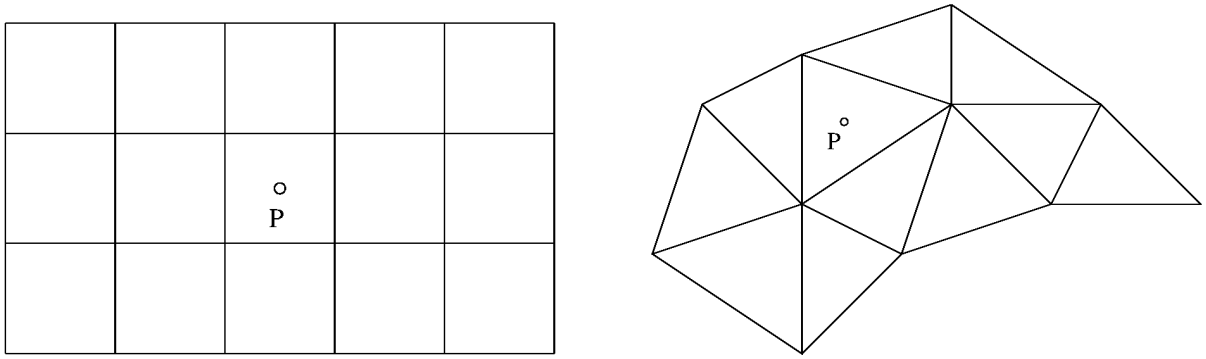

Fig. 5.2.: Structured mesh (left) and unstructured mesh (right).

In the subsequent section the equations are approximated in consideration of the accounting spatial discretization with arbitrary polyhedrons.

5.2. Equation Discretization

The governing equations are integrated over the solution domain Ω. Exemplarily, the integration is performed for the momentum equation (3.8) of the incompressible, steady state RANS equations, resulting in

$$\int_\Omega \rho \frac{\partial}{\partial x_j} u_i u_j d\Omega = -\int_\Omega \frac{\partial p}{\partial x_i} d\Omega + \int_\Omega \frac{\partial}{\partial x_j} \left[\mu_e \left(\frac{\partial u_i}{\partial x_j} + \frac{\partial u_j}{\partial x_i} \right) \right] d\Omega + \int_\Omega f_i d\Omega \,. \tag{5.1}$$

The balance equations hold for arbitrary control volumes. The integral over the whole computational domain Ω is thus split into integrals over the control volumes $V \in \Omega$, due

to the spatial discretization, which all follow (5.1)

$$\sum_{V\in\Omega}\int_V \rho\frac{\partial}{\partial x_j}u_iu_jdV = \sum_{V\in\Omega}\left\{-\int_V\frac{\partial p}{\partial x_i}dV + \int_V\frac{\partial}{\partial x_j}\left[\mu_e\left(\frac{\partial u_i}{\partial x_j}+\frac{\partial u_j}{\partial x_i}\right)\right]dV + \int_V f_i dV\right\}. \tag{5.2}$$

Using numerical integration, an algebraic equation is derived for each cell P, depending on the neighbor cells N. In the following, the most frequently used identities are itemized for a scalar ϕ.

- Gauß' theorem states

$$\int_V\frac{\partial}{\partial x_i}\phi dV = \oint_{\Gamma(V)}\phi n_i d\Gamma\,, \tag{5.3}$$

  where n_i denotes the outward pointing normal vector and $\Gamma(V)$ denotes the boundary of the control volume V.

- The closed surface integral over the boundary of a control volume V is expressed by the sum over all associated boundary faces f

$$\oint_{\Gamma(V)}\phi n_i d\Gamma = \sum_{f\in\Gamma(V)}\int_f \phi n_i df\,. \tag{5.4}$$

- Using the second order midpoint rule, volume and surface integrals are approximated by

$$\int_V \phi dV = \phi^{(P)}V^{(P)}\,, \tag{5.5}$$

$$\int_f \phi n_i df = \phi^{(f)}A_i{}^{(f)}\,, \tag{5.6}$$

  where $\phi^{(P)}$, $\phi^{(f)}$ denote the values for ϕ at cell center P and face center f, respectively. To obtain a second order accuracy, the centroid P has to be placed in the center of the control volume V.

Using the above mentioned expressions, the discretization of the primal and adjoint RANS and RANS-F equations at the control volumes is examined term-by-term. Basically, the main focus is on the approximation of:

- Surface and volume integrals
- Interpolation of face values
- Interpolation of face gradients

The following criteria should be considered for the discretization [75].

- Conservativity: The scheme should be conservative, i.e. the flux leaving the control volume through a face should be equal to the flux entering from the adjacent cell through the same face. Conservativity is achieved by choosing the same finite approximation for all face fluxes between P and N.
- Boundedness: The flow variable should be bounded by the minimum and maximum values of the neighbor cells. Boundedness is guaranteed by positive matrix coefficients m of discretization matrix M, i.e. $m^{(P)} \geq 0$, and diagonal dominance, i.e. $\sum_N |m^{(N)}| < |m^{(P)}|$ for all P and related neighbor cells N.
- Order of discretization: The lowest order determines the discretization order. To ensure high accuracy, a higher order of discretization is preferred. In practice, second order methods are sufficient [71].

In the next section, the discretization is considered in detail for the terms in the primal and adjoint RANS-F equations.

5.3. Primal and Adjoint Discretization Schemes

Primal and adjoint discretization schemes are identified for the convection, diffusion and source terms of the primal and adjoint equation systems. Specific attention is given to the duality of primal and adjoint discretization schemes, yielded by transposition of the discretization matrix.

Primal Convection

By means of Gauß' theorem (5.3), the discretization of the convection term for a general variable ϕ leads to

$$\int_V \rho \frac{\partial}{\partial x_j} \phi u_j dV = \oint_{\Gamma(V)} \rho n_j \phi u_j d\Gamma = \sum_{f \in \Gamma(V)} \rho \left(\phi u_n A\right)^{(f)} = \sum_{f \in \Gamma(V)} \phi^{(f)} \dot{m}_f \,, \tag{5.7}$$

where $A^{(f)}$ denotes the area of face f and $\dot{m}_f$ denotes the mass flux through face f,

$$\dot{m}_f = \rho u_n^{(f)} A^{(f)} \,, \tag{5.8}$$

computed via linear interpolation of face velocity ${u_n}^{(f)}$,

$${u_n}^{(f)} = \xi_P {u_n}^{(P)} + (1 - \xi_P) \, {u_n}^{(N)} \,, \tag{5.9}$$

with linear interpolation weight ξ_P, associated to cell P. Due to the product of the velocities, the convection term of the momentum equation (3.8) is non-linear. A standard approach

to deal with the convection term is linearization. Hereby, the values entering the mass flux are taken from an existing velocity field, usually from the previous iteration.
The value for the transported property in Equation (5.7) is expressed by the values on cell centers P and neighboring cells N or their respective gradients. In doing so, only the nearest neighbors N should be regarded. Physically, convection is a directional process [71]. This property needs to be taken into account when choosing the interpolation scheme. The **first-order upwind differencing scheme (UDS)** is mostly used for convection, as it is bounded and matches the physical properties of the convection. The face value $\underline{u}^{(f)}$ in the convection term (5.7) is determined, according to the direction of the flow, viz.

$$\underline{u}^{(f)} = \underline{u}^{(P)} \quad \text{if} \quad \dot{m}_f \geq 0\,, \tag{5.10}$$

$$\underline{u}^{(f)} = \underline{u}^{(N)} \quad \text{if} \quad \dot{m}_f < 0\,, \tag{5.11}$$

where the mass flux is computed from linear interpolation (5.9). The face value is taken from the cell center in upwind direction. Figure 5.3 illustrates the upwind scheme.

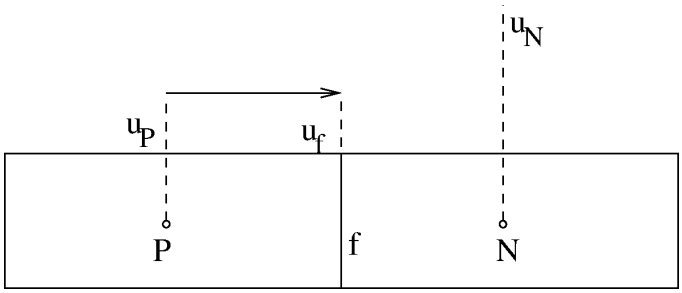

Fig. 5.3.: Upwind differencing scheme.

The UDS scheme ensures first order accuracy. The leading error of UDS is proportional to the diffusion term and may disturb the numerical solution. For high Reynolds numbers, the error due to an artificial approximation-based diffusion may be significantly larger than the actual physical diffusion. This effect is called *numerical diffusion* [71]. High-order upwind-based schemes are often used in deferred-correction mode to improve the accuracy for convection dominated high-Re number flows.

Adjoint Convection

In this paragraph consistent adjoint discretization schemes are derived for the convection term in the adjoint momentum equation (4.42),

$$-\int_V \rho u_i \frac{\partial \hat{\phi}}{\partial x_i} \delta\phi dV\,. \tag{5.12}$$

It is shown, that the adjoint complement to the primal upwind discretization scheme for the convection term is the downwind scheme. Initially, the discretization for the varied system is

derived. Subsequently, the discretization matrix is transposed. As a result, a discretization for the adjoint system is obtained. By using the upwind scheme (5.10), (5.11), the primal discretization of the convection term (5.7) reads

$$\int_V \rho \frac{\partial}{\partial x_j} \phi u_j dV = \sum_{f \in \Gamma(V)} \phi^{(f)} \dot{m}_f \approx \sum_{f \in \Gamma(V)} \left\{ \max\left(\dot{m}_f, 0\right) \phi^{(P)} + \min\left(\dot{m}_f, 0\right) \phi^{(N)} \right\}. \tag{5.13}$$

Part of the varied convection, leading to the adjoint convection, is considered, namely

$$\int_V \rho \frac{\partial}{\partial x_j} u_j \delta\phi dV = \sum_{f \in \Gamma(V)} \delta\phi^{(f)} \dot{m}_f \approx \sum_{f \in \Gamma(V)} \left\{ \left(\max\left(\dot{m}_f, 0\right) \delta\phi^{(P)} + \min\left(\dot{m}_f, 0\right) \delta\phi^{(N)} \right) \right\}. \tag{5.14}$$

In the next step, the discretization matrix for the varied variables is derived. The numerical integration for each cell results in a sum over all faces. Using index notation for matrices, all computational cells are numbered. The face between two computational cells k and s is denoted as $f = ks$, with associated normal vector pointing from cell k to cell s, and $f = sk$, with normal vector in opposite direction. If cell k and s do not share a face, it is set $\dot{m}_{ks} := 0$, such that the following matrix is obtained for the discretization of the varied convection part in Equation (5.14)

$$\begin{pmatrix} \sum_k \max\left(\dot{m}_{1k}, 0\right) & \min\left(\dot{m}_{12}, 0\right) & \cdots & \min\left(\dot{m}_{1n}, 0\right) \\ \min\left(\dot{m}_{21}, 0\right) & \sum_k \max\left(\dot{m}_{2k}, 0\right) & \cdots & \min\left(\dot{m}_{2n}, 0\right) \\ \vdots & \vdots & \vdots & \vdots \\ \min\left(\dot{m}_{n1}, 0\right) & \min\left(\dot{m}_{n2}, 0\right) & \cdots & \sum_k \max\left(\dot{m}_{nk}, 0\right) \end{pmatrix} \begin{pmatrix} \delta\phi^{(1)} \\ \delta\phi^{(2)} \\ \vdots \\ \delta\phi^{(n)} \end{pmatrix}. \tag{5.15}$$

Each row consists of n entries, at which n indicates the number of cells. Augmenting the primal convection part with Lagrange multipliers and factoring out the variational flow properties equals a transposition of the discretization matrix. Thus, the discretization of the adjoint system results in

$$\begin{pmatrix} \sum_k \max\left(\dot{m}_{1k}, 0\right) & \min\left(\dot{m}_{21}, 0\right) & \cdots & \min\left(\dot{m}_{n1}, 0\right) \\ \min\left(\dot{m}_{12}, 0\right) & \sum_k \max\left(\dot{m}_{2k}, 0\right) & \cdots & \min\left(\dot{m}_{n2}, 0\right) \\ \vdots & \vdots & \vdots & \vdots \\ \min(\dot{m}_{1n}, 0) & \min(\dot{m}_{2n}, 0) & \cdots & \sum_k \max(\dot{m}_{nk}, 0) \end{pmatrix} \begin{pmatrix} \hat{\phi}^{(1)} \\ \hat{\phi}^{(2)} \\ \vdots \\ \hat{\phi}^{(n)} \end{pmatrix}. \tag{5.16}$$

Considering cell s yields

$$\sum_k \max\left(\dot{m}_{sk}, 0\right) \hat{\phi}^{(s)} + \sum_k \min\left(\dot{m}_{ks}, 0\right) \hat{\phi}^{(k)}. \tag{5.17}$$

With $\dot{m}_{ks} = -\dot{m}_{sk}$ it is obtained

$$\sum_k \max\left(\dot{m}_{sk}, 0\right) \hat{\phi}^{(s)} + \sum_k \min\left(-\dot{m}_{sk}, 0\right) \hat{\phi}^{(k)} \,. \tag{5.18}$$

Due to the continuity balance, it holds

$$\sum_k \max\left(\dot{m}_{sk}, 0\right) = -\sum_k \min\left(\dot{m}_{sk}, 0\right) \,. \tag{5.19}$$

Therefore, (5.18) transforms to

$$-\sum_k \min\left(\dot{m}_{sk}, 0\right) \hat{\phi}^{(s)} + \sum_k \min\left(-\dot{m}_{sk}, 0\right) \hat{\phi}^{(k)} \,, \tag{5.20}$$

and, using $-\min\left(\dot{m}_{sk}, 0\right) = \max\left(-\dot{m}_{sk}, 0\right)$ leads to

$$\sum_k \max\left(-\dot{m}_{sk}, 0\right) \hat{\phi}^{(s)} + \sum_k \min\left(-\dot{m}_{sk}, 0\right) \hat{\phi}^{(k)} \,. \tag{5.21}$$

For a control volume V and its faces f, associated to cell centers P and N, the discretization of the adjoint convection reads

$$-\int_V \rho u_i \frac{\partial \hat{\phi}}{\partial x_i} dV = -\oint_{\Gamma(V)} \rho u_i n_i \hat{\phi} d\Gamma = \sum_{f \in \Gamma(V)} \left\{ \max\left(-\dot{m}_f, 0\right) \hat{\phi}^{(P)} + \min\left(-\dot{m}_f, 0\right) \hat{\phi}^{(N)} \right\} . \tag{5.22}$$

The resulting scheme corresponds to the upwind scheme for the negative convection term, equal to the **downwind differencing scheme**.

Primal Diffusion

The discretization of the diffusion term of the primal momentum equation (3.8) is considered, viz.

$$\int_V \frac{\partial}{\partial x_j} \left[\mu_e \left(\frac{\partial u_i}{\partial x_j} + \frac{\partial u_j}{\partial x_i} \right) \right] dV \,. \tag{5.23}$$

By applying Gauß' theorem (5.3) and the continuity equation (3.9), the term is transformed to

$$\int_V \frac{\partial}{\partial x_j} \left[\mu_e \left(\frac{\partial u_i}{\partial x_j} + \frac{\partial u_j}{\partial x_i} \right) \right] dV = \oint_{\Gamma(V)} \mu_e \left(\frac{\partial u_i}{\partial x_j} \right) n_j d\Gamma = \sum_{f \in \Gamma(V)} \mu_e^{(f)} \left(\frac{\partial u_i}{\partial x_j} \right)^{(f)} {A_j}^{(f)} \,, \tag{5.24}$$

using linear interpolation for $\mu_e^{(f)}$. The discretization of the surface normal gradient ${A_j}^{(f)} \frac{\partial u_i}{\partial x_j}$ at face f is considered. Opposed to the convection, which is a one-way quantity, the diffusion is non-directional and therefore approximated in a symmetric way. For an orthogonal mesh with outward pointing vector ${A_j}^{(f)}$ and connecting vector $\vec{PN}$ parallel to each other, the term of Equation (5.24) is approximated via

$$ {A_j}^{(f)} \left(\frac{\partial u_i}{\partial x_j} \right)^{(f)} = A^{(f)} \frac{u^{(N)} - u^{(P)}}{|\vec{PN}|} \,, \tag{5.25} $$

using $A^{(f)} = |{A_j}^{(f)}|$.
For non-orthogonal meshes, the term ${A_j}^{(f)} \frac{\partial u_i}{\partial x_j}$ is split into an orthogonal part, in direction of the connection vector $\vec{PN}$, and a non-orthogonal part,

$$ {A_i}^{(f)} \left(\frac{\partial u_i}{\partial x_j} \right)^{(f)} = \underline{o}_n \left(\frac{\partial u_i}{\partial x_j} \right)^{(f)} + \underline{o}_t \left(\frac{\partial u_i}{\partial x_j} \right)^{(f)} , \tag{5.26} $$

where $\underline{o}_n$ denotes the orthogonal, and $\underline{o}_t$ the non-orthogonal part. The vectors $\underline{o}_n$ and $\underline{o}_t$ are chosen, such that

$$ {A_i}^{(f)} = \underline{o}_n + \underline{o}_t \,. \tag{5.27} $$

The orthogonal vector coefficient $\underline{o}_n$ is chosen to be parallel to $\vec{PN}$ and is determined by using Equation (5.25). The non-orthogonal part is explicitly computed from linear interpolation

$$ \left(\frac{\partial u_i}{\partial x_j} \right)^{(f)} = \xi_P \left(\frac{\partial u_i}{\partial x_j} \right)^{(P)} + (1 - \xi_P) \left(\frac{\partial u_i}{\partial x_j} \right)^{(N)} , \tag{5.28} $$

by employing the current gradient values. Various possibilities to split ${A_j}^{(f)}$ into $\underline{o}_n$ and $\underline{o}_t$ are presented, for example, in [45]. The type of correction is specified by choice of a surface normal gradient scheme. The non-orthogonal correction may lead to unboundedness [45], especially if the mesh non-orthogonality is high. For reduction of the unboundedness, the correction may be limited or completely left out.
The thermal diffusion in the primal internal energy equation (3.27) is treated analogously to the diffusion term in the momentum equation (5.24), by Gauß transformation,

$$ \int_V \frac{\partial}{\partial x_j} \left[\kappa_e \frac{\partial T}{\partial x_j} \right] dV = \oint_{\Gamma(V)} \kappa_e \frac{\partial T}{\partial n} d\Gamma = \sum_{f \in \Gamma(V)} \kappa_e^{(f)} \left(\frac{\partial T}{\partial n} \right)^{(f)} A^{(f)} \,, \tag{5.29} $$

choice of an interpolation scheme for κ_e and a surface normal gradient scheme.

Adjoint Diffusion

The dual discretization scheme for the diffusion term,

$$\int_V \frac{\partial}{\partial x_j}\left(\mu_e \frac{\partial \hat{\phi}}{\partial x_j}\right) dV\,, \tag{5.30}$$

is deduced. Again, starting point is the discretization of the linearized, primal diffusion. The variation of the diffusive flux for an orthogonal mesh, according to Equation (5.24) and (5.25), results in

$$\delta \int_V \frac{\partial}{\partial x_j}\left(\mu_e \frac{\partial \phi}{\partial x_j}\right) dV = \sum_{f\in\Gamma(V)} \mu_e^{(f)} \left(\frac{\partial \delta\phi}{\partial x_j}\right)^{(f)} A_j{}^{(f)} = \sum_{f\in\Gamma(V)} \mu_e^{(f)} A^{(f)} \frac{\delta\phi^{(N)} - \delta\phi^{(P)}}{|\vec{PN}|}\,. \tag{5.31}$$

Using the matrix notation and $|\vec{ks}|$ for the distance between cell k and s, the discretization (5.31) results in

$$\begin{pmatrix} -\sum_k \frac{\mu_e A^{(1k)}}{|\vec{1k}|} & \frac{\mu_e A^{(12)}}{|\vec{12}|} & \cdots & \frac{\mu_e A^{(1n)}}{|\vec{1n}|} \\ \frac{\mu_e A^{(21)}}{|\vec{21}|} & -\sum_k \frac{\mu_e A^{(2k)}}{|2k|} & \cdots & \frac{\mu_e A^{(2n)}}{|\vec{2n}|} \\ \vdots & \vdots & \vdots & \vdots \\ \frac{\mu_e A^{(n1)}}{|\vec{n1}|} & \frac{\mu_e A^{(n2)}}{|\vec{n2}|} & \cdots & -\sum_k \frac{\mu_e A^{(nk)}}{|\vec{nk}|} \end{pmatrix} \begin{pmatrix} \delta\phi^{(1)} \\ \delta\phi^{(2)} \\ \vdots \\ \delta\phi^{(n)} \end{pmatrix}\,, \tag{5.32}$$

where $A^{(ks)}$ denotes the face magnitude for face $f = ks$ with $A^{(ks)} := 0$, if k and s are non-adjacent. The matrix is symmetric, as $A^{(ks)} = A^{(sk)}$ and $|\vec{sk}| = |\vec{ks}|$, and, therefore, equal to its transposed counterpart. The symmetric property reflects the self-adjointness of the diffusion operator. For orthogonal meshes, the adjoint diffusion is treated analogously to the primal diffusion,

$$\int_V \frac{\partial}{\partial x_j}\left(\mu_e \frac{\partial \hat{\phi}}{\partial x_j}\right) dV = \sum_{f\in\Gamma(V)} \mu_e{}^{(f)} \left(\frac{\partial \hat{\phi}}{\partial x_j}\right)^{(f)} A_j{}^{(f)} = \sum_{f\in\Gamma(V)} \mu_e{}^{(f)} A^{(f)} \frac{\hat{\phi}^{(N)} - \hat{\phi}^{(P)}}{|\vec{PN}|}\,. \tag{5.33}$$

For non-orthogonal meshes, the explicit non-orthogonality correction is directly reapplied in the adjoint algorithm, with the adjoint correction term reading, accordingly,

$$\underline{o}_t \left(\frac{\partial \hat{\phi}}{\partial x_j}\right)^{(f)}\,. \tag{5.34}$$

Primal and Adjoint Source Terms

Terms that cannot be written as convective or diffusive terms are treated as sources. A source term S_ϕ is considered as a general function of ϕ. The source term is split into an explicit part, S_C, and an implicit part, S_P, viz.

$$S_\phi = S_C + S_P \cdot \phi \,. \tag{5.35}$$

An explicit source term is approximated by appropriate discretization schemes, by taking the values from the previous iteration, and then added to the right-hand side of the equation [23]. An implicit source is integrated over the control domain and linearized by midpoint rule (5.5). Accordingly, numerical integration of the source term (5.35) leads to

$$\int_V S_\phi dV = {S_C}^{(P)} V^{(P)} + {S_P}^{(P)} V^{(P)} \phi^{(P)} \,. \tag{5.36}$$

Thus, the explicit part, ${S_C}^{(P)} V^{(P)}$, enters the right-hand side of the equation and the coefficient in the implicit part, ${S_P}^{(P)} V^{(P)}$, enters the matrix. It is advisable to treat the source term implicitly, if possible [45]. To sustain diagonal dominance, terms associated to negative diagonal coefficients are treated explicitly, terms with positive impact implicitly. The treatment of the remaining terms of the considered equations are described in the following. The **advection term** (4.6) of the adjoint momentum equation (4.42),

$$-\int_V \rho u_i \frac{\partial \hat{u}_i}{\partial x_j} dV \,, \tag{5.37}$$

with additional boundary term, is a supplementary term only apparent in the adjoint equations. It arises from part of the variation of the convection term. There are different approaches, derived and validated by [60], [31], [78]. Mainly, it is distinguished between schemes, derived from the discretization of the continuous equations, and schemes, derived from the discrete equations by transposition of the discretization matrix. As the advection term includes the gradient of the adjoint velocity, thus, taking large values near the boundary for turbulent flow problems, it is neglected for the sake of convergence in this thesis. On the one hand, neglecting the advection term leads to robust simulations, but, on the other hand, it distorts the result for the adjoint flow field and the sensitivity. The momentum equation of the adjoint Navier-Stokes-Fourier equations (4.82) also contains an advective term, arising from part of the variation of the convection term of the primal internal energy equation (3.27). Analogously to the advection term in the adjoint momentum equation, the term may be integrated by using integration by parts, leading to a modified volume integral and a boundary integral. In both cases the advection term is treated explicitly. Hence, the term is approximated from the values of the previous iteration step by choice of a gradient and interpolation scheme (Gauß linear). The **Darcy term** inside the primal and adjoint momentum equations (3.32),(4.106) is treated implicitly by approximation via the midpoint rule. Thus, it enters the system as matrix coefficient. If $\alpha > 0$, the coefficient

sustains the diagonal dominance. The **pressure gradient** in primal and adjoint momentum equations (3.8), (4.42) is treated implicitly within the Laplace equation of the pressure correction scheme, which will be referred to later, by Gauß' theorem and choice of a surface normal gradient scheme (snGradScheme). The primal and adjoint **continuity equation** (3.9), (4.43) is treated explicitly inside the pressure correction method (see Section 5.6), using Gauß' theorem and linear interpolation. Primal and adjoint **dissipation** in (3.27) and (4.82) is treated explicitly, by separation into the accounting gradients, using Gauß' theorem and linear interpolation. Primal and adjoint **buoyancy** in (3.25) and (4.84) are treated explicitly by using the midpoint rule (5.5). Table 5.1 summarizes the numerical treatment of the source terms.

Table 5.1.: Numerical treatment of source terms.

Term	Implicit/Explicit	Numerical scheme
advection in adjoint RANS-F	explicit	Gauß, linear interpolation
Darcy term	implicit	midpoint rule
primal & adjoint pressure gradient	implicit	Gauß, snGradScheme
primal & adjoint continuity equation	explicit	Gauß, linear interpolation
primal & adjoint dissipation	explicit	Gauß, linear interpolation
primal & adjoint buoyancy	explicit	midpoint rule

Computation of Boundary Fluxes

At the boundary faces **boundary fluxes** are obtained, contributing to the balance of the adjacent inner control volumes. From the primal boundary conditions, defined in Section 3.4, and the adjoint boundary conditions ((4.44)–(4.50) and (4.85)–(4.94)) the fluxes are computed for inlet, outlet, walls and symmetry planes by appropriate discretization schemes.

5.4. Turbulence Modeling

In Chapter 3 the steady state fluid dynamic equations (3.8) and (3.9) are derived by application of an averaging procedure. From this averaging operation the Reynolds stress

tensor arises, which is subsequently modeled by the Boussinesq approximation (3.5) using an isotropic turbulent dynamic viscosity μ_t. In the near-wall region, the computation of the turbulence properties has to be considered carefully, as the physics distinguishes from other parts of the flow domain [45]. There are two main approaches for the computation near the wall region; in the low-Reynolds (low-Re) approach, the flow properties are fully resolved in the near-wall region. Therefore, a fairly fine mesh is necessary, leading to an accurate solution, yet, induces higher computational effort. In the high-Reynolds (high-Re) number approach, the turbulence properties near the wall are modeled with *wall functions*, by taking advantage of the well studied behavior of boundary layer flows. As the high-Re approach allows for using coarse meshes in the near-wall region, the computational effort decreases and is thus common practice for complex fluid computations. Both approaches are described in the following.
The flux of momentum, denoted as F_i, at a wall face f_w is considered, being the sum of diffusive, convective and pressure induced flux,

$$F_i = F_i^d + F_i^c + F_i^p \,. \tag{5.38}$$

Gauß' theorem is applied to the convection term (5.7) at the near wall cell, leading to the convective flux at the wall face, which is zero,

$$F_i^c = \int_{f_w} \rho n_j u_i u_j df = \dot{m}_{f_w} u_i^{(f_w)} = 0 \,, \tag{5.39}$$

due to the zero velocity boundary condition at the wall. Application of Gauß' theorem to the pressure gradient at the near wall cell in the momentum equation (3.8) leads to

$$F_i^p = \int_{f_w} p n_i df = p^{(f_w)} A_i^{f_w} \,. \tag{5.40}$$

As the face value $p^{(f_w)}$ is computed from the zero gradient boundary condition at the wall and a Taylor series approximation, the pressure wall face value results in $p^{(f_w)} = p^{(P)}$. For the diffusive flux (5.23) the application of Gauß' theorem and the plane Couette flow assumption results in

$$F_i^d = \int_{f_w} \mu_e \frac{\partial u_{i(t)}}{\partial x_j} n_j df = \int_{f_w} {\tau_i}^w df \,, \tag{5.41}$$

where ${\tau_i}^w$ denotes the wall shear stress,

$${\tau_i}^w := \mu_e \left(\frac{\partial u_{i(t)}}{\partial n} \right)_{y=0} \,, \tag{5.42}$$

and y the distance to the wall. In the following, it is anticipated that the tangential velocity vector reduces to one velocity component in the direction tangential to the wall, denoted as

u, and the change of the wall normal component is suppressed. This assumption is justified if curvature aspects are neglected [70]. For a **low-Re** strategy, a fine grid is necessary to resolve the linear near wall zone below a dimensionless wall distance of $y^+ = 5$,

$$\frac{\partial u}{\partial n} = \frac{u^{(P)}}{y^{(P)}}\,, \tag{5.43}$$

by making use of the fact that the values of velocity and wall distance are zero at the wall. As the connecting vector between wall node and cell center is parallel to the surface normal vector ${A_i}^f$, no orthogonality correction applies. For a high-Re strategy, a relatively coarse mesh is used, i.e. the distance to the first off-wall node, $y^{(P)}$, is fairly large. Compared to the linear near wall zone, the physics of the flow change completely in this region of the wall. Therefore, the velocity gradient cannot be approximated via the difference quotient. For this purpose, the **law of the wall** is applied, stating, that the average velocity of a turbulent flow is proportional to the logarithm of the distance to the wall. The law of the wall reads

$$U^+ = \frac{1}{K}\ln(\mathtt{E}y^+) \quad \text{with} \quad \mathtt{E} = 9.793\,,\ K = 0.41\,, \tag{5.44}$$

with dimensionless velocity U^+, wall distance y^+ and friction velocity u_τ defined as

$$U^+ := \frac{u^{(P)}}{u_\tau}\,, \tag{5.45}$$

$$y^+ := \frac{y u_\tau}{\nu}\,, \tag{5.46}$$

$$u_\tau := \sqrt{\frac{\tau_w}{\rho}}\,, \tag{5.47}$$

where ν denotes the kinematic viscosity, $\nu = \frac{\mu}{\rho}$ and τ_w the wall shear stress magnitude. Note that Equation (5.44) only holds in the logarithmic layer, for which $y^+ \gtrsim 30$. Using sufficiently coarse meshes with $y^+ \gtrsim 30$, the law of the wall can be applied. In detail, the law of the wall can be studied, for example, in [67]. Hence, the diffusive flux at the wall face (5.41) is computed from the squared friction velocity, using Equation (5.47),

$${F_i}^d = \int_{f_w} {\tau_i}^w df = \int_{f_w} {u_\tau}^2 \rho\, t_i\, df\,, \tag{5.48}$$

which is expressed by the logarithmic law of the wall (Equation (5.44) and (5.45)),

$$u_\tau = \frac{K u^{(P)}}{\ln(\mathtt{E}y^+)}\,. \tag{5.49}$$

Besides from the flux of momentum, the heat flux through the wall is considered. The heat flux, denoted as F^q, through the wall is computed, from Equation (5.29) as

$$F^q = \int_{f_w} -\kappa_e \frac{\partial T}{\partial n} df = \int_{f_w} q^w df \,, \tag{5.50}$$

with wall heat flux q^w. Using a low-Re approach, the normal temperature gradient is modeled via the difference quotient, analogously to (5.25), such that

$$\frac{\partial T}{\partial n} = \frac{T^{(P)} - T^{(w)}}{y^{(P)}} \,, \tag{5.51}$$

requiring a fine mesh to avoid errors. Reynolds' analogy between momentum and energy transport gives a similar logarithmic law for the mean temperature. The thermal law of the wall [47] states for the logarithmic layer,

$$T^+ = \frac{\rho u_\tau c_p (T^{(w)} - T^{(P)})}{q^w} = Pr_t \left[\frac{1}{K} \ln(\mathtt{E} y^+) + \mathtt{P} \right] = Pr_t \left[U^+ + \mathtt{P} \right] \,, \tag{5.52}$$

where $\mathtt{P}$ denotes the Jayatilleke wall function, defined as

$$\mathtt{P} = 9.24 \left(\frac{Pr}{Pr_t}^{\frac{3}{4}} - 1 \right) \left(1 + 0.28 e^{-0.007 \frac{Pr}{Pr_t}} \right) \,, \tag{5.53}$$

T^+ denotes the dimensionless temperature. The thermal law of the wall (5.52) leads to an equation for the wall heat flux q^w,

$$q^w = \frac{\rho u_\tau c_p (T^{(w)} - T^{(P)})}{T^+} = \frac{\rho u_\tau c_p (T^{(w)} - T^{(P)})}{Pr_t \left(\ln(\mathtt{E} y^+) \frac{1}{K} + \mathtt{P} \right)} \,. \tag{5.54}$$

The calculation of wall shear stress magnitude τ_w and wall heat flux q^w from the law of the wall is realized in an indirect manner, by proper boundary conditions, as outlined in the following.

Turbulent Boundary Conditions

For the transport equations for k (3.10) and ω (3.11), boundary conditions are required. To compute the wall shear stress (5.42) and the wall heat flux (5.50) by the accounting model (low-Re or high-Re), wall boundary conditions for μ_t and κ_t are properly set.

Wall

A boundary condition for μ_t models the wall shear stress (5.42) by a low-Re or high-Re approach. In a **low-Re** computation, the wall shear stress is computed from the difference

quotient (5.43) and μ_t from the ratio of k and ω (3.12). For a coarse mesh, the approximation through the difference quotient is inexact. For a **high-Re** computation the turbulent eddy viscosity is adapted, such that the approximation through the difference quotient is accurate. The turbulent eddy viscosity is required to fulfill

$$\mu_e \frac{u^{(P)}}{y^{(P)}} = \tau_w \,. \tag{5.55}$$

For wall shear stress magnitude τ_w holds by (5.47) and (5.49),

$$\tau_w = \rho u_\tau^2 = \frac{\rho u_\tau u^{(P)} K}{\ln(\mathtt{E} y^+)} \,. \tag{5.56}$$

Therefore, it holds for $\mu_e = \mu_t + \mu$ and by using Equation (5.55) and (5.56),

$$(\mu + \mu_t) \frac{u^{(P)}}{y^{(P)}} = \frac{\rho u^{(P)} u_\tau K}{\ln(\mathtt{E} y^+)} \,. \tag{5.57}$$

By inserting Equation (5.46) for u_τ, Equation (5.57) is reformulated to the final boundary condition for μ_t at the wall,

$$\mu_t = \left(\frac{K y^+}{\ln(\mathtt{E} y^+)} - 1 \right) \mu \quad \text{on} \quad \Gamma_w \,. \tag{5.58}$$

Analogously, the boundary condition for κ_t is required to model the wall heat flux (5.50),

$$q^w = -\kappa_e \left(\frac{\partial T}{\partial n} \right)_{y=0} \,. \tag{5.59}$$

In a **low-Re** computation, the wall heat flux is computed from the difference quotient, κ_t computed from μ_t and Pr_t. Analogously to the wall shear stress, the turbulent heat conductivity has to be adapted for the **high-Re** approach, such that the approximation through the difference quotient resembles the wall heat flux. The turbulent thermal heat conductivity κ_t is required to fulfill

$$-\kappa_e \frac{(T^{(P)} - T^{(w)})}{y^{(P)}} = q^w \,. \tag{5.60}$$

Using $Pr = \frac{\mu c_p}{\kappa}$, $\kappa_e = \kappa + \kappa_t$, and combining Equation (5.60) with Equation (5.54) for the wall heat flux, results in the high-Re boundary condition for κ_t at the wall,

$$\kappa_t = \mu c_p \left(\frac{y^+}{Pr_t \left(\ln(\mathtt{E} y^+) \frac{1}{K} + \mathtt{P} \right)} - \frac{1}{Pr} \right) \,. \tag{5.61}$$

Depending on the model, low-Re and high-Re wall boundary conditions are set for the turbulent kinetic energy k and specific dissipation rate ω. For **low-Re** computations, the turbulent kinetic energy k equals zero at the wall,

$$k = 0 \quad \text{on} \quad \Gamma_w \,. \tag{5.62}$$

For a **high-Re** computation, the turbulent kinetic energy k is set to a homogeneous Neumann boundary condition, i.e.

$$\frac{\partial k}{\partial n} = 0 \quad \text{on} \quad \Gamma_w \,, \tag{5.63}$$

asymptotically equal to the zero gradient boundary condition. The boundary condition for the turbulent dissipation rate ω is taken from Menter [56]. For **low-Re** cases, ω is set to

$$\omega^{(P)} = \frac{6\nu}{\beta_1 {y^{(P)}}^2} \quad \text{on} \quad \Gamma_w \,, \tag{5.64}$$

in which $\beta_1 = 0.075$ is a constant. In the **high-Re** case, ω is computed from

$$\omega^{(P)} = \frac{\sqrt{k^{(P)}}}{C_\mu^{\frac{1}{4}} K y^{(P)}} \quad \text{on} \quad \Gamma_w \,, \tag{5.65}$$

at which $C_\mu = 0.09$ is a constant.

Inlet

At the inlet, the turbulent kinetic energy k is computed from the turbulence intensity I, as performed comparably, for example, in [59],

$$k = \frac{3}{2}(|\underline{u}_{in}| \cdot I)^2 \quad \text{on} \quad \Gamma_{in} \,. \tag{5.66}$$

The value of I depends on the level of turbulence. The turbulent dissipation rate ω is computed from the mixing length ℓ [59],

$$\omega = \frac{\sqrt{k}}{C_\mu{}^{\frac{1}{4}} \ell} \quad \text{on} \quad \Gamma_{in} \,. \tag{5.67}$$

Since the treatment of the turbulence properties is not in the focus of the thesis, a detailed description is omitted. Further information is found, for example, in [67].

Outlet

At the outlet k and ω are set to zero gradient boundary condition, i.e.

$$\frac{\partial \omega}{\partial n} = 0 \quad \text{and} \quad \frac{\partial k}{\partial n} = 0 \quad \text{on} \quad \Gamma_{out} \,. \tag{5.68}$$

5.5. Algebraic Equation System

Out of the finite volume discretization, a system of algebraic equations is created, viz.

$$m^{(P)}\phi^{(P)} + \sum_N m^{(N)}\phi^{(N)} = R^{(P)} \,, \tag{5.69}$$

with right-hand side for cell P denoted as $R^{(P)}$. The system of equations is solved in the segregated approach [64, 36], i.e. the equations for the variables in the distinct control volumes are solved one by one in a certain order. This sequence is also called *outer iteration*. The outer iteration is repeated until an error tolerance is met. Within a so called *inner iteration* a Picard linearization is used and the equation for the variables are solved iteratively, until an error tolerance is met (see [45]). To establish the inter-equation coupling, a special treatment is required; the semi-implicit pressure linked equation solver (SIMPLE) algorithm [65] couples the continuity and momentum equations and is described in detail in Section 5.6. For solving the equation system $M\phi = R$, the most common iterative solvers are utilized, namely preconditioned (bi-)conjugate gradient (PCG/PBiCG) or generalized geometric-algebraic multi-grid (GAMG). Iterative solvers are preferable, as they benefit from the sparsity of the equation system [45]. Compared to direct solvers, they are also more appropriate for huge systems of equations. For a detailed description of the iterative solvers see, for example, [55]. Diagonal dominance is required to guarantee convergence. Therefore, in the discretization, terms are treated, such that the diagonal dominance is sustained. A preferred implicit scheme, sustaining the diagonal dominance, is the upwind differencing scheme for the convection (cf. Section 5.2). Another criterion that should be fulfilled is boundedness of the solution. Boundedness guarantees that the computed variable value lie between neighboring values. Violating the boundedness of the system leads to unphysical results and oscillating values [71]. To guarantee boundedness, all matrix coefficients need to be positive. When applying a non-orthogonal correction, one has a trade-off between accuracy of the discretization and boundedness of the matrix system, as the correction weakens the diagonal dominance due to the integration of second neighbor control volumes. Therefore, the correction terms are inserted explicitly as source terms on the right-hand side. The orthogonal term remains implicit in the equation system. Another method to increase the diagonal dominance is to apply **under-relaxation**. The idea is to decrease the progress from one iteration to the other by a limiting factor, $0 < \alpha_\phi \leq 1$, such that the iteration in step n becomes

$$\phi^n = \phi^{old} + \alpha_\phi \left(\phi^{new} - \phi^{old}\right) \,, \tag{5.70}$$

where ϕ^{old} denotes the value from the previous iteration and ϕ^{new} the solution for cell P of

$$m^{(P)}\phi^{new} + \sum_N m^{(N)}\phi^N = R^{(P)} \tag{5.71}$$

with related neighbors N. Inserting Equation (5.71) for ϕ^{new} in (5.70) leads to the following equation system,

$$\frac{m^{(P)}}{\alpha_\phi}\phi^n + \sum_N m^{(N)}\phi^{(N)} = R^{(P)} + \frac{1-\alpha_\phi}{\alpha_\phi} m^{(P)}\phi^{old}\,. \tag{5.72}$$

As the diagonal coefficient is divided by $\alpha_\phi \leq 1$, the diagonal dominance is increased.

5.6. Pressure Correction Scheme

The Reynolds averaged Navier-Stokes equations (3.8) and (3.9) are considered for an incompressible fluid. The system of equations leads to a saddle point problem, as the continuity equation (3.9) only contains information on the velocity, but not on the pressure. Thus, the information on velocity and pressure has to be decoupled, as performed by the SIMPLE algorithm [16], [65] introduced in this section. In the first step the momentum equation (3.8) is discretized and linearized. For this purpose, Equation (3.8) is rewritten in a semi-discretized form as,

$$m^{(P)}u^{(P)} + \sum_N m^{(N)}u^{(N)} = -\frac{\partial p}{\partial x_i}\,. \tag{5.73}$$

For the velocity component $u^{(P)}$ holds

$$u^{(P)} = \frac{1}{m^{(P)}}\left(-\frac{\partial p}{\partial x_i} + H(u)\right)\,, \tag{5.74}$$

where $H(u)$ includes the matrix coefficients for all neighbors, multiplied by the corresponding velocities and all other source terms apart from the pressure gradient,

$$H(u) = -\sum_N m^{(N)}u^{(N)}\,. \tag{5.75}$$

In the next step, the linearized equation system has to be solved for each unknown at each mesh point. In 3D, for each computational cell P, the equation system consists of three equations and four unknowns. Therefore, a preliminary velocity $\tilde{u}$ without the contribution of the pressure gradient is defined,

$$\tilde{u}^{(P)} = \frac{1}{m^{(P)}}H(u)\,. \tag{5.76}$$

The preliminary velocity does in general not fulfill the continuity equation,

$$\frac{\partial \tilde{u}_i}{\partial x_i} \neq 0\,. \tag{5.77}$$

Application of the continuity equation (3.9) to the equation for the velocity (5.74) leads to the Laplace equation for the pressure,

$$\frac{1}{m^{(P)}}\frac{\partial^2 p}{\partial {x_i}^2} = \frac{\partial}{\partial x_i}\frac{H(u)}{m^{(P)}} = \frac{\partial \tilde{u}_i}{\partial x_i}\,, \tag{5.78}$$

by inserting the definition of the preliminary velocity (5.76). The Laplace equation is discretized in the standard way (compare to Equation (5.24)), such that the following discretized form is obtained

$$\sum_f \frac{1}{m^{(P)}}\left(\frac{\partial p}{\partial n}\right)^{(f)} A^{(f)} = \sum_f \left(\frac{H(u)}{m^{(P)}}\right)^{(f)} {A_i}^{(f)}\,. \tag{5.79}$$

In conjunction with the new pressure, the velocity u is corrected by using (5.74) and (5.76),

$$u = \tilde{u} - \frac{1}{m^{(P)}}\frac{\partial p}{\partial x_i}\,. \tag{5.80}$$

Accordingly, a correction for the fluxes is performed,

$${A_i}^{(f)} u^{(f)} = {A_i}^{(f)}\left[\left(\frac{H(u)}{m^{(P)}}\right)^{(f)} - \frac{1}{m^{(P)}}\left(\frac{\partial p}{\partial x_i}\right)^{(f)}\right]\,. \tag{5.81}$$

Consequently, the continuity equation is fulfilled, but, in general the momentum equation is not fulfilled. Repetition of the procedure improves the conformance for both, continuity and momentum equation. Algorithm 3 summarizes the steps of the SIMPLE algorithm.

Algorithm 3: SIMPLE Algorithm.

1. Momentum-Predictor Step: Obtain a preliminary velocity by solving Equation (5.76).
2. Pressure Correction: Solve the Laplace equation for the pressure (5.79).
3. Explicit Velocity Correction: Update the velocity and the fluxes by solution of Equation (5.80) and (5.81).
4. Repeat until convergence is obtained.

6. Verification and Validation

In this chapter validation and verification studies are presented. In the first section the adjoint shape sensitivity is compared to the derivative obtained from finite differences. In the second section the solution method for the gradient is examined by comparison of the numerical solution of the Laplace-Beltrami equation to the analytical solution for an academic test case. The third section presents a mesh study for the prediction quality of coarsened meshes. In the last section the sparsity promoting regularization term is validated by application to simple, fluid dynamic test cases.

6.1. Verification of Sensitivities

The adjoint shape sensitivity displays the directional derivative of the cost functional with respect to a normal displacement of the design surface. For verification purposes, the adjoint sensitivity is compared to the derivative of the cost functional, obtained from finite differences (see also [49]). Subsequently, the gradient is computed from the sensitivities by solving the Laplace-Beltrami equation. The considered test case comprises the laminar flow over a 2D heated ellipse, centrally mounted in a channel. The computational domain covers $10^{-2}\,\mathrm{m} \times 2 \cdot 10^{-3}\,\mathrm{m}$. The height of the ellipse is $2 \cdot 10^{-4}\,\mathrm{m}$. Only half of the symmetric configuration is computed. The mesh consists of 28 000 control volumes, consisting of unstructured hexahedrons and associated hanging nodes. Figure 6.1 displays the computational grid.

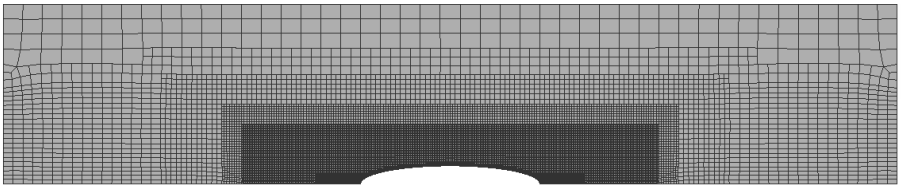

Fig. 6.1.: Computational grid for test case heated ellipse.

The inlet bulk velocity is assigned to $u_B = 1.5 \cdot 10^{-1}\,\frac{\mathrm{m}}{\mathrm{s}}$. The Reynolds number, based on the height of the channel ($l = 2 \cdot 10^{-3}\,\mathrm{m}$) and a kinematic viscosity of $\nu = 1.5 \cdot 10^{-5}\,\frac{\mathrm{m}^2}{\mathrm{s}}$, is $Re = \frac{u_B \cdot l}{\nu} = 20$, hence the flow is considered laminar. The mean temperature is set to $T = 290\,\mathrm{K}$. The ellipse is heated with a temperature of $T = 291\,\mathrm{K}$. Hereby, the related Grashof number is $Gr = \frac{g_0 \cdot \beta_T \cdot \Delta T \cdot L^3}{\nu^2} = 1$, with the standard acceleration due to gravity of $g_0 = 9.81\,\frac{\mathrm{m}^2}{\mathrm{s}}$ and a thermal expansion coefficient $\beta_T = 3 \cdot 10^{-3}/\mathrm{K}$. Except for the ellipse,

the upper and lower domain boundaries are assigned to symmetry conditions. For inlet and outlet, typical boundary conditions are employed. At the inlet, prescribed velocity and temperature, as well as zero pressure gradient are employed. Zero gradient for temperature and velocity, as well as prescribed pressure are used at the outlet. The ellipse, marking the design surface, is set to no-slip. The temperature is set to 290 K along the lower and upper boundaries and $T = 291\,\mathrm{K}$ along the ellipse. As an example for the adjoint sensitivity analysis the deviation to a desired temperature referring to $T_d = 291\,\mathrm{K}$ (3.39) is minimized at the outlet. The cost functional is associated to a contribution to the adjoint boundary condition (4.94), defined in Equation (6.1), viz.

$$\rho\hat{T}u_n + \kappa_e\frac{\partial\hat{T}}{\partial n} + (T - T_d) = 0 \quad \text{on} \quad \Gamma_{out}\,. \tag{6.1}$$

For the simulation a suitable solver (*buoyantBoussinesqSimpleFoam*) of OpenFOAM®, based on the SIMPLE algorithm (Algorithm 3), and its adjoint analogue are applied to the primal and adjoint Reynolds-averaged Navier-Stokes-Fourier equations (3.25)–(3.27) and (4.82)– (4.84). The buoyancy term is modeled by the Boussinesq approximation (3.24). The simulation for the primal flow was iterated until a fair level of convergence was achieved, i.e. normalized initial residuals below 10^{-6} and 25 000 iterations. Hereby, the initial residuals are scaled with a normalization factor by default. In Figure 6.2 the results for the primal velocity and temperature are presented.

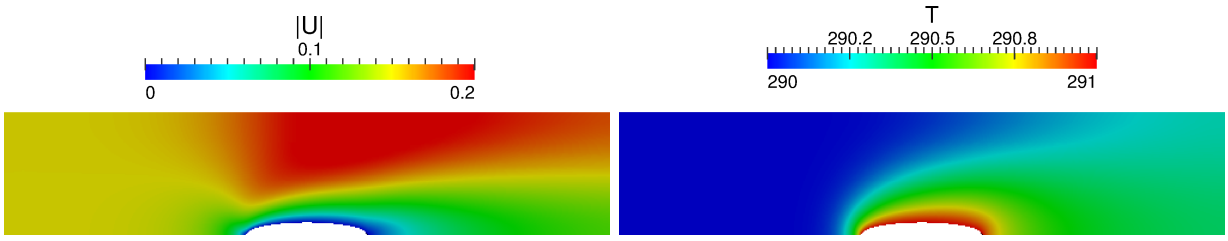

Fig. 6.2.: Predicted primal magnitude of the velocity (left) and temperature field (right).

The temperature has its maximum at the ellipse and features a plume downstream of the heated obstacle (Figure 6.2, right). Since the Reynolds number is fairly low, a significant amount of diffusion distributes the density and temperature plume along the complete outlet cross section. The displacement of the velocity field towards the upper boundary (Figure 6.2, left), induced by the obstacle, is supported by buoyancy terms downstream of the ellipse.
Based on the primal flow field, the adjoint Reynolds-averaged Navier-Stokes-Fourier equations are solved until a fair level of convergence is achieved (normalized initial residuals fall below 10^{-6}). Note that the adjoint solution has no strict physical meaning, therefore, the plausibility of the results is usually hard to judge. The main criterion on judging the quality of the results is the sensitivity, computed from the primal and adjoint flow field in a postprocessing step, according to Equation (4.101). Hereby, the surface normal gradients of the primal and adjoint velocity are computed and projected into the tangential direction.

The result of the adjoint sensitivity is outlined in Figure 6.3, including a diagram for the sensitivity plotted on the surface of the ellipse. The diagram shows the 410 discrete design surface elements along the abscissa and their sensitivity values on the ordinate. Hereby, the sensitivity is scaled by wall patch area $\Delta\Gamma_w$ at each surface patch, respectively.

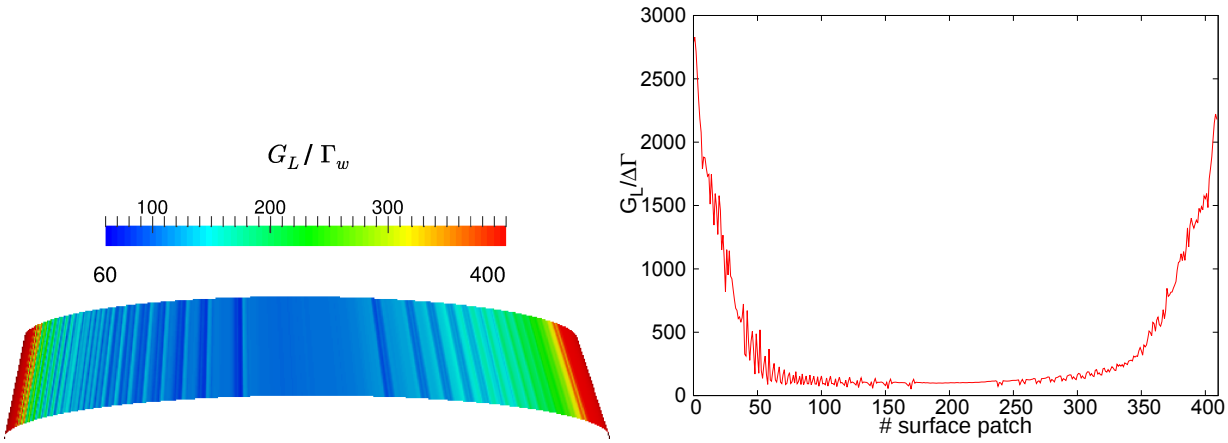

Fig. 6.3.: Contour plot (left) and diagram (right) of adjoint sensitivity for heated ellipse.

Large sensitivities are obtained at the ends of the ellipse, smaller ones along the crest. Note that the sensitivity displays the derivative of the cost functional with respect to an outward movement of the surface, i.e. with respect to an increase of the fluid volume.
The derivative of the cost functional, obtained from the adjoint solution, is compared to the derivative of the cost functional, obtained from (first-order) finite differences. For this purpose, the derivative of the cost functional is approximated for each node on the surface Γ_{dsg} from a first-order accurate differencing scheme, according to Equation (6.2),

$$\frac{\partial J}{\partial \beta} = \frac{J_{new} - J_{old}}{\Delta\beta} + \mathcal{O}((\Delta\beta)^2)\,, \tag{6.2}$$

involving the values of the cost functional for the perturbed mesh (J_{new}) and for the original mesh (J_{old}). Note that this approximation is only valid for perturbations small enough to neglect non-linearities, but prone to numerical errors for very small perturbations. As in the computation of the sensitivity, the finite differences are scaled with wall patch area $\Delta\Gamma_w$. The generation of the required 410 computational meshes is scripted to minimize mesh-quality influences on the approximated cost functional derivative. A normal perturbation of $\Delta\beta = 2 \cdot 10^{-10}\,\mathrm{m}$, $\Delta\beta = 1 \cdot 10^{-9}\,\mathrm{m}$ and $\Delta\beta = 2 \cdot 10^{-9}\,\mathrm{m}$ is used in the present study. Figure 6.4 shows the sensitivities along the axis of the ellipse, obtained from the finite difference approach. The sensitivities obtained from finite differences are congruent for different magnitudes of the perturbation. Thus, the perturbations are small enough to neglect nonlinearities. Figure 6.5 displays the comparison of the adjoint sensitivity to the derivative of finite differences for $\Delta = 2 \cdot 10^{-9}$.

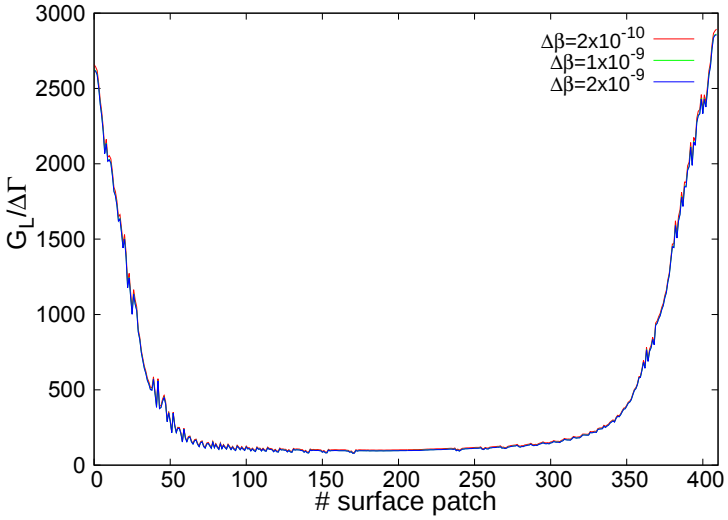

Fig. 6.4.: Sensitivity from finite differences for different magnitudes of the perturbation.

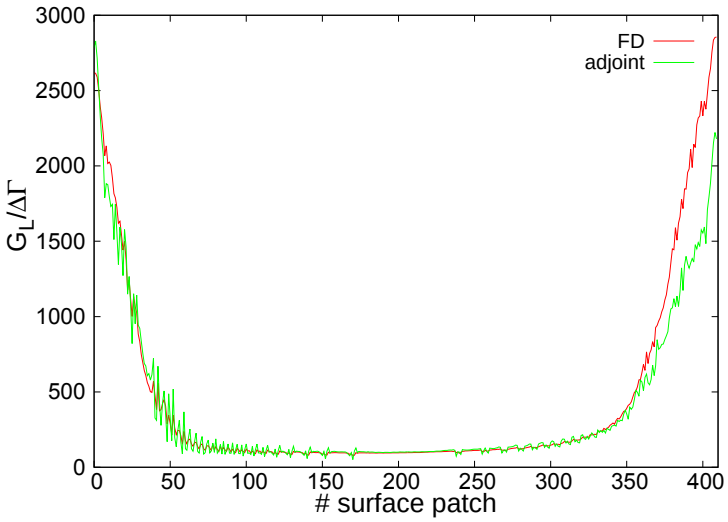

Fig. 6.5.: Comparison of adjoint sensitivity to sensitivity from finite differences.

The adjoint sensitivity displays a satisfactory agreement with the result of the finite differences. The agreement deteriorates at the rear of the obstacle (in the direction of flow), due to the performed approximations in the derivation of the sensitivity (neglection of advection term and particularly curvature aspects). The trend – or sign of the derivative – however always agrees between the two evaluation techniques.
For further evaluation purposes, the gradient is computed by solving the Laplace-Beltrami equation based on the sensitivity fields, obtained from finite differences and from the adjoint calculation. The accounting sensitivity serves as right-hand side in the Laplace-Beltrami equation (4.138). The implicit second order partial differential equation is solved by an appropriate solver, implemented in OpenFOAM® [29]. The gradients from finite differences

and from the adjoint sensitivity are plotted along the axis of the ellipse, displayed in Figure 6.6.

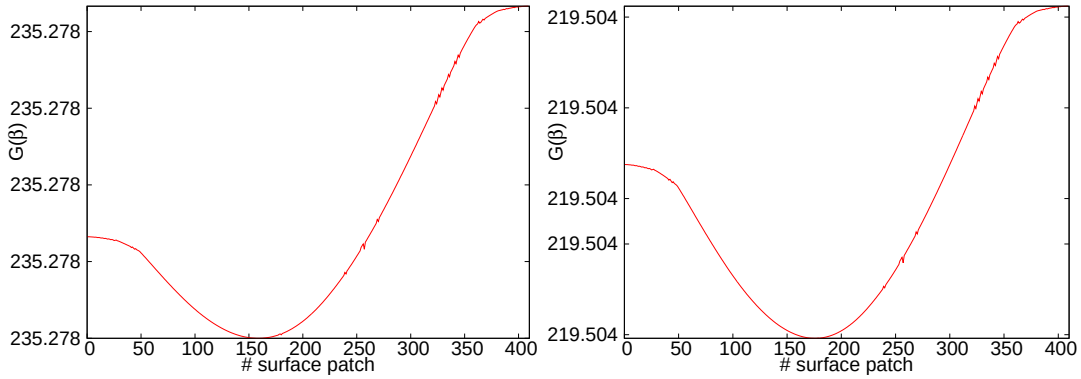

Fig. 6.6.: Gradient from finite differences for $\Delta = 2 \cdot 10^{-9}$ (left), gradient from adjoint sensitivity (right), plotted on ellipse.

The qualitative development of both gradients agrees well. However, the values of the gradients, obtained from finite differences and adjoint sensitivity, disagree ($G_L = 235.278$ for the gradient from finite differences and $G_L = 219.504$ for the gradient from the adjoint sensitivity, see Figure 6.6). However, the gradients are both almost at a constant level, respectively. Compared to the sensitivity (Figure 6.5), the gradient is at a level about 10 times smaller. A reason for this discrepancy is the influence of the mesh size $\Delta x \approx 5\,\mathrm{m}^{-6}$ of the surface patch area on the solution of the Laplace-Beltrami equation.
The study shows that the behavior of the adjoint sensitivity agrees qualitatively well with the behavior of the sensitivity, obtained from finite differences. The gradient from the adjoint sensitivity is thus able to predict the behavior of the flow for moderate surface shape deformations.

6.2. Verification of Gradient Computation

An accurate solution method for the Laplace-Beltrami equation is essential, as the result provides the gradient (cf. Section 4.5), subsequently used in the gradient descent. On that account, the numerical solution of the Laplace-Beltrami equation is verified in this section. For this purpose, an academic test case is considered for which the exact solution of the Laplace-Beltrami equation is known. The comparison of the numerical to the analytical solution then provides information on the quality of the solution method. In the first step the analytic solution of the Laplace-Beltrami equation is derived for the considered test case. In the second step the setup for the numerical simulation is presented. In the last part of the section the numerical results are compared to the analytical data, being able to compute absolute and relative errors.
Under consideration is an analytic test case on a circle. The employment of cylindrical coordinates is preferred. Thus, a mapping of the local, Cartesian coordinate vector (x, y)

onto the polar coordinate system is performed,

$$\begin{pmatrix} x \\ y \end{pmatrix} \longrightarrow \begin{pmatrix} r\cos(\theta) \\ r\sin(\theta) \end{pmatrix} , \tag{6.3}$$

marked by angle θ and radius r. From the Laplace operator formulated in physical cylindrical coordinates,

$$\Delta = \frac{\partial^2}{\partial r^2} + \frac{1}{r}\frac{\partial}{\partial r} + \frac{1}{r^2}\frac{\partial^2}{\partial \theta^2} , \tag{6.4}$$

the Laplace-Beltrami operator is derived, equal to the angular part of (6.4), viz.

$$\Delta_\Gamma = \frac{1}{r^2}\frac{\partial^2}{\partial \theta^2} , \tag{6.5}$$

see also [86] and [29].
The function $\sinh(\theta)$ is considered on the unit circle,

$$h(r,\theta) = h(1,\theta) = \sinh(\theta) . \tag{6.6}$$

The hyperbolic sine is an eigenfunction for the Laplace-Beltrami operator, since, under consideration of (6.5) and by setting $r = 1\,\mathrm{m}$,

$$\Delta_\Gamma h(r,\theta) = \frac{\partial^2}{\partial \theta^2}\sinh(\theta) = \sinh(\theta) . \tag{6.7}$$

Inserting $h(1,\theta)$ into the Laplace-Beltrami equation (4.138) yields

$$h(1,\theta) - \Delta_\Gamma h(1,\theta) = 0 , \tag{6.8}$$

by using (6.7). Thus, $h(1,\theta) = \sinh(\theta)$ is a solution of Equation (4.138) with zero right-hand.
Equation (6.8) is solved numerically by application of an appropriate solver, implemented in OpenFOAM® in [29]. The Laplace-Beltrami equation (4.138) with zero right-hand side (cf. (6.8)) is solved at the boundary of one quarter of the unit circle. Accordingly, the angle θ ranges between 0 and $\frac{\pi}{2}$. The circle line is discretized with 200 cells in circumferential direction. The rim is set to a height of $l = 0.001\,\mathrm{m}$. At the boundaries the function values are set to $h(1,\frac{\pi}{2}) = \sinh(\frac{\pi}{2}) = 2.3013$ and $h(1,0) = \sinh(0) = 0$, according to the considered function. At the arc a symmetry plane is employed (cf. [29] and Figure 6.7). The numerical solution of the Laplace-Beltrami equation, $G(\theta)$, is compared to the hyperbolic sine at the 200 discrete sampling points.

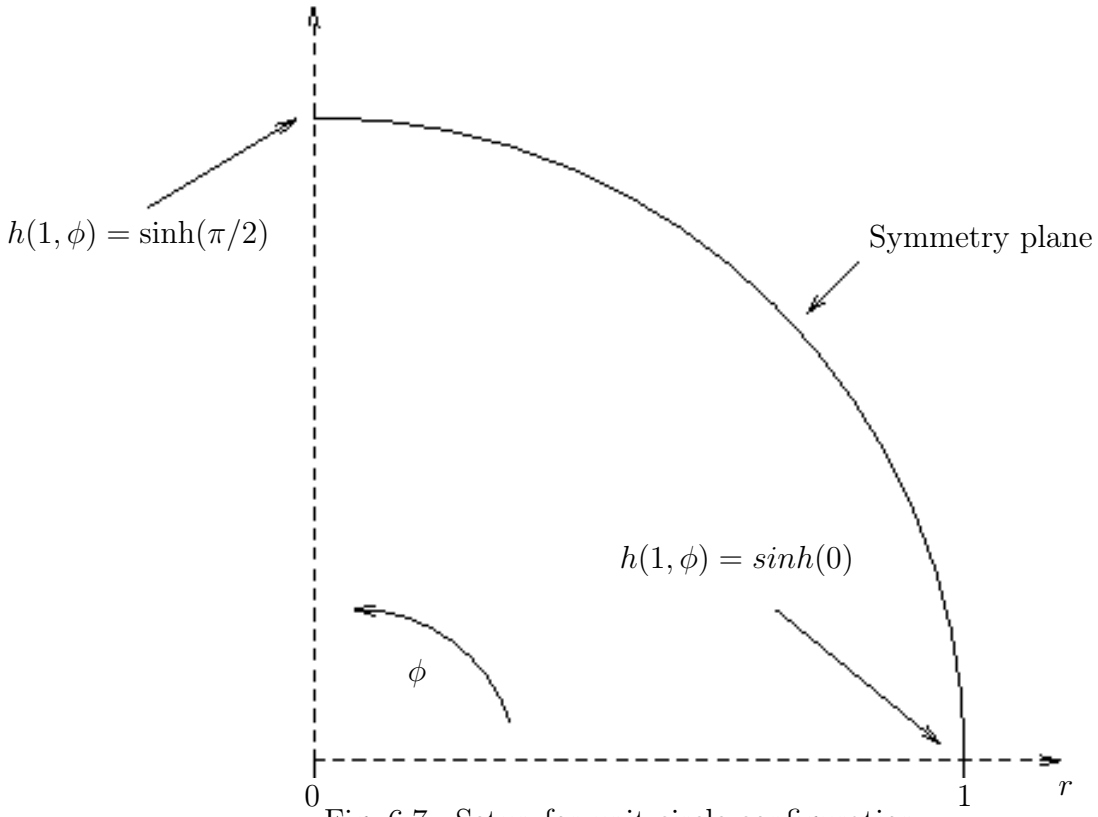

Fig. 6.7.: Setup for unit circle configuration.

The maximum absolute error is

$$\max_{0<\theta<\frac{\pi}{2}} |\sinh(1,\theta) - G(\theta)| = 0.004896\,, \tag{6.9}$$

taken at an angle of $\theta = \frac{\pi}{2}$. Employing the maximum function value, the relative error is thus computed as

$$\mathsf{e} = \frac{\max_{0<\theta<\frac{\pi}{2}} |\sinh(1,\theta) - G(\theta)|}{\max_{0<\theta<\frac{\pi}{2}} |\sinh(1,\theta)|} = \frac{0.004896}{2.231296} = 0.002127\,, \tag{6.10}$$

corresponding to 0.2 %. Hence, the numerical and analytical solutions only slightly distinguish. Figure 6.8 illustrates the result. The curves in Figure 6.8 almost perfectly coincide. Therefore, the numerical solution of the Laplace-Beltrami equation represents the analytic solution. The solver is thus able to accurately solve the Laplace-Beltrami equation. Small numerical errors may be led back to mesh approximation inaccuracies.

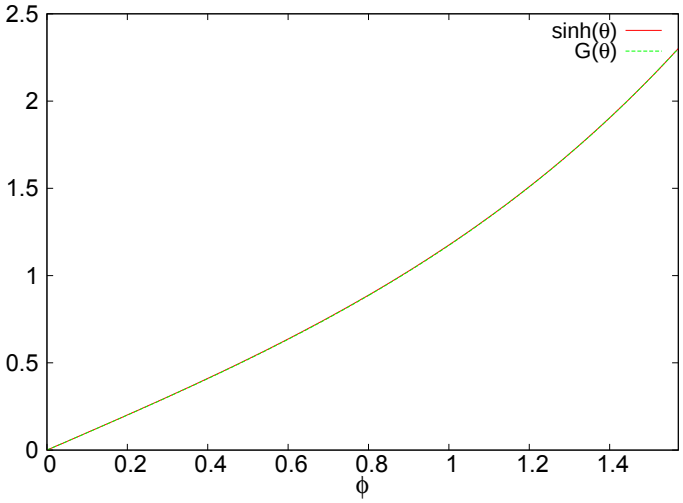

Fig. 6.8.: Comparison of analytical to numerical solution of Laplace-Beltrami equation.

6.3. Validation of Mesh Coarsening

In Section 2.6 a *reduced* Armijo algorithm has been presented. Instead of solving the RANS equations on the reference mesh to evaluate the cost functional, a coarser mesh is utilized for the cost functional evaluation to save computational time and resources.
In this section the quality of coarsened meshes is validated by performing numerical simulations for different levels of refinement. The validation is performed for two test cases, a cylinder test case, modeled by a structured mesh in 2D, analogously to Schäfer and Turek in 1996 [72] and a test case for the flow through a bend duct, modeled by an unstructured mesh in 3D. The difference to characteristic reference data is computed to evaluate the quality of the results.

Cylinder

This case has been well studied by different research groups, as published in [72]. The computational domain is a 2D rectangle $\Omega = [0, 2.2]\,\mathrm{m} \times [0, 0.41]\ \mathrm{m}$ and features a circular cylinder of radius $r = 0.05\,\mathrm{m}$, located at $(0.2\,\mathrm{m}, 0.2\,\mathrm{m})$, with respect to its midpoint. A parabolic inlet profile located at the left boundary models the inflow. Upper, lower and cylinder boundaries are set to no-slip walls. At the right boundary typical outlet boundary conditions (zero pressure, zero gradient velocity) are set. Figure 6.9 illustrates the computational setup.

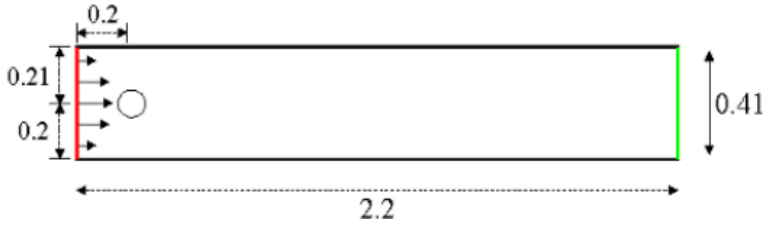

Fig. 6.9.: Cylinder test case setup [15].

The parabolic inflow profile is described by

$$u(0, y) = \left(\frac{4\, u_{max}\, y(0.41 - y)}{0.41^2}, 0 \right) , \tag{6.11}$$

with a maximum velocity of $u_{max} = 0.3\,\frac{\mathrm{m}}{\mathrm{s}}$. A contour plot of the inlet velocity is displayed in Figure 6.10.

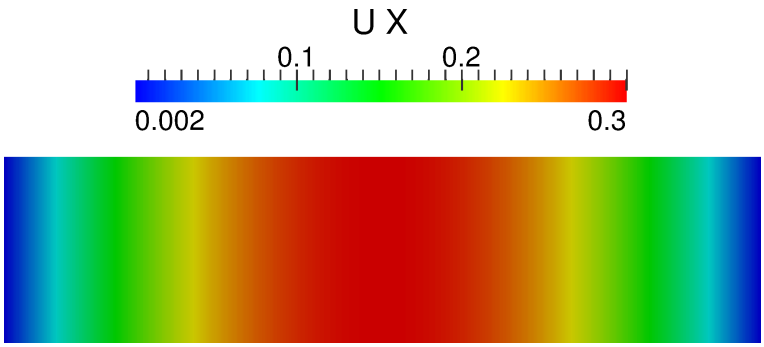

Fig. 6.10.: Inlet velocity for test case cylinder.

The test case is laminar at a Reynolds number of $Re = 20 = \frac{u_B \cdot l}{\nu}$, with the diameter of the cylinder, $l = 0.1\,\mathrm{m}$ and the bulk velocity, $u_B = 0.2\,\frac{\mathrm{m}}{\mathrm{s}}$. For further reference, see [72]. Ten distinct structured meshes have been generated, using the OpenFOAM® routine *blockMesh*. The number of computational cells ranges from $\#V = 514$ to $\#V = 274\,652$. A coarsening factor of approximately two lies between the accounting mesh levels. The stationary, incompressible RANS equations (3.8) and (3.9) are solved on the meshes by using the solver *simpleFoam*, based on the SIMPLE algorithm (see Algorithm 3). Up to 3 000 iterations are performed until a fair level of convergence is achieved (normalized initial residuals fall below 10^{-4}). The normalized pressure difference $p_{diff} := \frac{1}{\rho} p(a_1) - \frac{1}{\rho} p(a_2)$ in the points directly in front of and behind the cylinder ($a_1 = (0.15\,\mathrm{m}, 0.2\,\mathrm{m})$ and $a_2 = (0.25\,\mathrm{m}, 0.2\,\mathrm{m})$) is determined. The numerical results for the pressure coefficient ($C_p = \frac{2p}{(\rho {u_B}^2)}$) on four different meshes are illustrated in Figure 6.11.

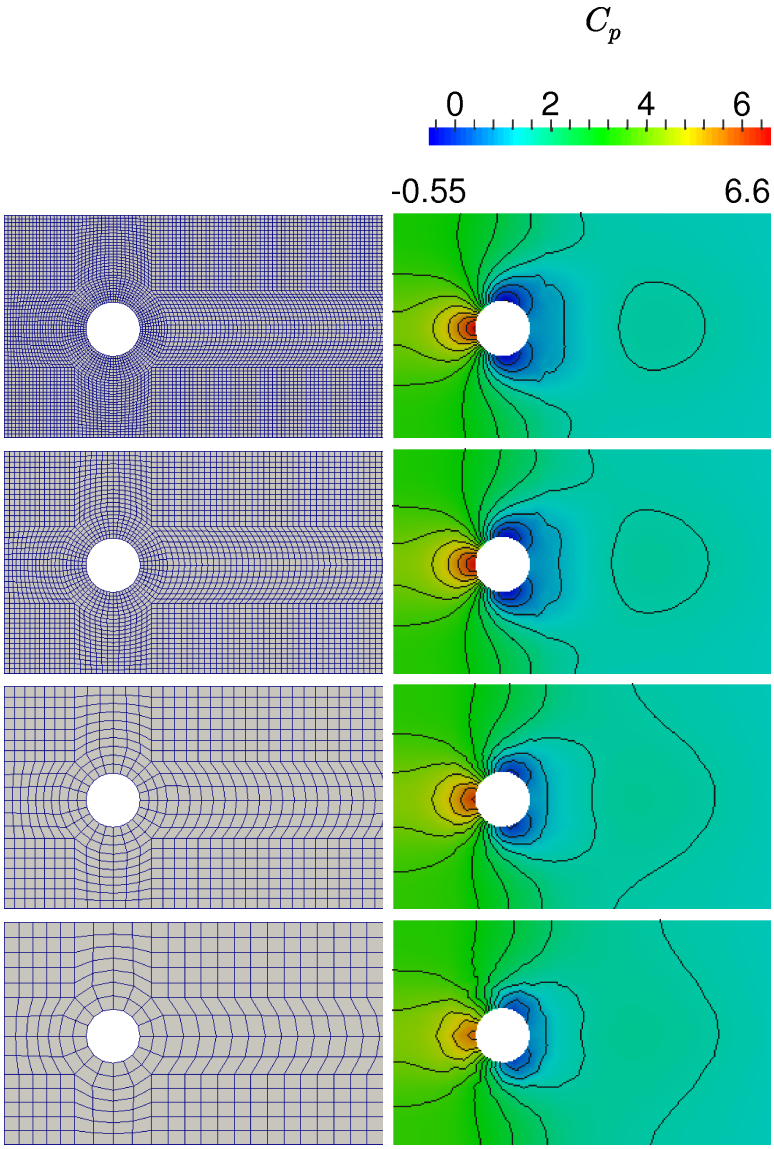

Fig. 6.11.: Generated structured meshes (left) and related pressure coefficient with fitting contour lines (right) around cylinder for $\#V = 17\,800$, $\#V = 8\,806$, $\#V = 2\,076$ and $\#V = 1\,025$ (from top to bottom, respectively).

To judge the conformity of the pressure coefficient, the fitting contour lines for the considered four different meshes are illustrated in Figure 6.12. As apparent from Figure 6.12, the contour lines for the pressure coefficients for $\#V = 17\,800$ and $\#V = 8\,086$ agree fairly well. For this reason, meshes with a resolution higher than $\#V = 17\,800$ are dispensable. Therefore, the focus lies on meshes with $\#V = 17\,800$ or less. The results for the meshes with $\#V = 2\,076$ and $\#V = 1\,025$ intensely discriminate from the results of the finer meshes (see Figure 6.12).

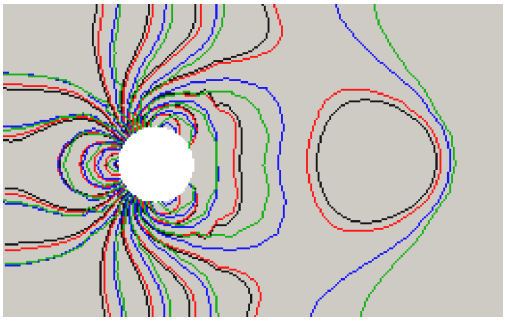

Fig. 6.12.: Pressure coefficient with fitting contour lines around cylinder for $\#V = 17\,800$ (black), $\#V = 8\,806$ (red), $\#V = 2\,076$ (blue) and $\#V = 1\,025$ (green).

Analogously to [72], the numerical results are compared to the solution gained from high order spectral methods (see [58]). In this way, the reference value for the pressure difference is expected to $p_{diff} = 0.117520\,\frac{\mathrm{m}^2}{\mathrm{s}^2}$. Table 6.1 displays the values for pressure difference and relative errors with respect to the reference solution.

Table 6.1.: Error in the computation of p_{diff} for different meshes.

Number of cells $\#V$	514	1 025	2 076	4 450	8 806
p_{diff} in $\frac{\mathrm{m}^2}{\mathrm{s}^2}$	0.081531	0.098534	0.105927	0.112305	0.114380
Relative error e	30.6 %	16.1 %	9.9 %	4.4 %	2.7 %
Number of cells $\#V$	17 800	34 888	70 480	138 880	274 652
p_{diff} in $\frac{\mathrm{m}^2}{\mathrm{s}^2}$	0.115701	0.116483	0.117017	0.117341	0.117552
Relative error e	1.5 %	0.9 %	0.4 %	0.1 %	<0.1 %

The computation for $\#V = 17\,800$ leads to a relative error e =1.5 %, which is a reasonable result. This mesh offers a good balance between accuracy and computational cost. A coarsening by factor four ($\#V = 4\,450$) still delivers reasonable results ($\mathsf{e} = 4.4\,\%$). Reducing the number of cells by a factor of eight ($\#V = 2\,076$) already leads to a relative error of 9.9 %. The results for the meshes with $\#V = 1\,025$ or less nodes are unreliable ($\mathsf{e} \geq 16.1\,\%$). Starting from the mesh with $\#V = 17\,800$, a reduction factor up to four is acceptable to judge the general behavior of the fluid dynamic properties. A reduction factor of eight is inadvisable.

Bend Duct

The second validation case for the comparison of mesh-fineness vs. accurateness is the stationary, laminar flow through a 3D bend duct. The geometry is taken from a tutorial case [4]. The volume mesh consists of unstructured tetrahedrons. Mesh generation has been performed using ANSA [4]. Figure 6.13 displays the geometry.

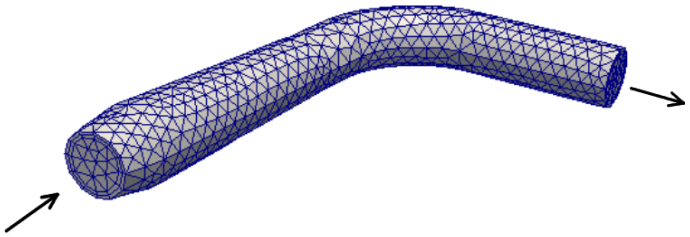

Fig. 6.13.: Geometry of bend duct. Inlet located on the left, outlet on the right.

The case consists of inlet, outlet, and wall with typical boundary conditions (no-slip velocity and zero pressure gradient at walls, fixed velocity and zero pressure gradient at inlet and zero pressure, zero velocity gradient at outlet). The bulk velocity at the inlet is set to $u_B = 0.011\,\frac{\mathrm{m}}{\mathrm{s}}$. A kinematic viscosity of $\nu = 1.49 \cdot 10^{-5}\,\frac{\mathrm{m}^2}{\mathrm{s}}$ is utilized. Based on the diameter of the inlet ($l = 0.04\,\mathrm{m}$), the Reynolds number is $Re = 30$. To answer the question of how coarse a mesh may get, different meshes are generated; the number of cells ranging from $\#V = 3\,466$ to $\#V = 669\,838$. The coarsening factor lies between 1.3 and 2.3. The governing fluid dynamic equations are the incompressible RANS equations (3.8) and (3.9). The simulations are performed by using the solver *simpleFoam* until a satisfactory level of convergence is reached (2 000 iterations, normalized initial residuals fall below 10^{-7}). The velocity magnitude is evaluated at a line on a cutting plane inside the duct (see Figure 6.14).

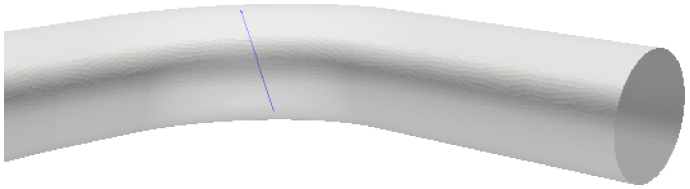

Fig. 6.14.: Bend duct with line (blue) on cutting plane for evaluation.

In the first step the computed velocity magnitude is compared visually along the reference line for the different meshes. As reference profile, the shape of a parabola is considered. The corresponding results are displayed in Figure 6.15. Due to the low Reynolds number, the velocity profiles converge to a parabolic shape. At the finest mesh level ($\#V = 669\,838$) a smooth parabolic velocity profile is reached, whereas the profiles of the coarser meshes contain kinks, due to the poor resolution. The computation for the mesh with $\#V = 36\,282$ already shows a quite reasonable velocity profile resembling a parabola while the result for the mesh with $\#V = 221\,618$ already delivers a velocity profile very close to a parabolic

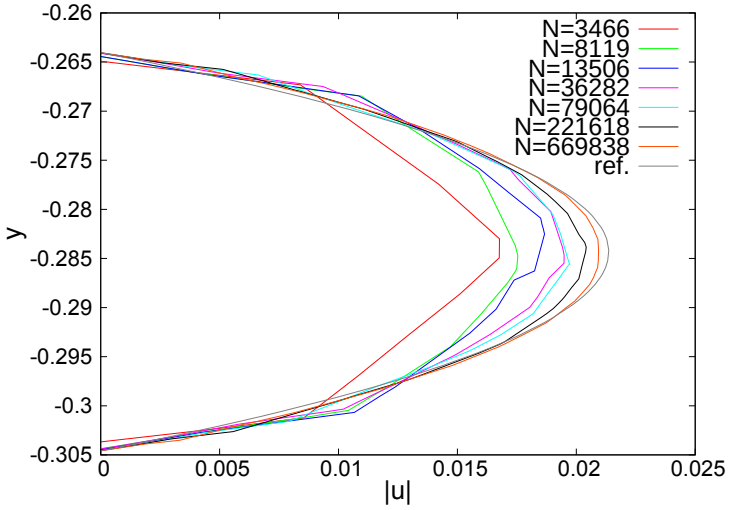

Fig. 6.15.: Velocity magnitude for different meshes and reference parabola profile.

shape. The computation for the meshes with $\#V = 3\,466$, $\#V = 8\,119$ and $\#V = 13\,506$ severely deviate from the velocity profile for the finest mesh ($\#V = 669\,838$). Hereby, large differences with respect to the maximum velocity value at the finest mesh level are obtained.
As a result, $\#V = 221\,618$ leads to reasonable predictions; the mesh with 36 282 cells yields already acceptable results of lower quality. Meshes with 13 506 or less control volumes are unreliable.
To validate the error numerically, the magnitude of the maximum velocity along the line at the finest mesh level (with 669 838 computational cells), $|\underline{u}_{max}| = 0.020935\ \frac{\mathrm{m}}{\mathrm{s}}$, is employed as a reference value for the error computation. Table 6.2 summarizes the results.

Table 6.2.: Error of maximum velocity magnitude for different meshes.

Number of cells $\#V$	3 466	8 119	13 506	25 067	36 282	55 876
$\lvert\underline{u}_{max}\rvert$ in $\frac{\mathrm{m}}{\mathrm{s}}$	0.016768	0.017544	0.018665	0.019046	0.019488	0.01927
Relative error e	19.9 %	16.2 %	10.8 %	9.0 %	6.9 %	7.9 %
Number of cells $\#V$	79 064	163 653	221 618	367 196	546 558	669 838
$\lvert\underline{u}_{max}\rvert$ in $\frac{\mathrm{m}}{\mathrm{s}}$	0.019724	0.020197	0.020415	0.020725	0.020903	0.020935
Relative error e	5.8 %	3.5 %	2.5 %	1.0 %	0.15 %	0.0 %

In line with the visual interpretation, the error for the computation with $\#V = 221\,618$ is sufficiently low (2.5 %). This mesh offers a good balance between accuracy and computational costs. The mesh with $\#V = 36\,282$ yields an error of 6.9 %, still acceptable to predict the general behavior of the fluid dynamic properties. Meshes with lower resolution yield an error of 9.0 % and more. Based on the mesh with $\#V = 221\,618$, a reduction factor of six ($\#V = 36\,282$) is still acceptable to obtain reasonable results. A reduction factor of 8 or more ($\#V = 25\,067$) leading to an error of $\mathsf{e} \geq 9.0\,\%$, is inadvisable. In summary, reduction factors up to six are advisable for the reduced Armijo approach. Employing reduction factors of this magnitude, delivers reasonable results for the Armijo evaluation, as well as reduces the computational costs as much as possible. Note that the factor computation bases on the mesh representing an optimal balance between accuracy and computational effort. Starting from a mesh with more cells, the reasonable reduction factor may even be higher.

6.4. Validation of Sparse Porosity Optimization

In this section the impact of the insertion of the L^1- regularization term into the topology optimization problem on the sparsity is validated (see Section 4.4) with two simple test cases in 2D, inspired by [6]. In the first place, the flow is simulated for the initial topology to obtain a reference flow solution and to determine the value of the considered cost functional. Subsequently, topology optimization is performed, firstly non-regularized, then with inserted regularization term and different weighting factors. The study compares the intensity of regularization with the amount of sparsity and the related degree of improvement.

Diffusor

The computational domain consists of a $0.1\,\mathrm{m} \times 0.1\,\mathrm{m}$ square, homogeneously discretized by 900 isotropic control volumes. In fact, due to simulation reasons, a third z-axis is included with $\Delta z = 0.01\,\mathrm{m}$, consisting of a single layer of cells. As the patch type for the front and rear patch is set to *empty*, the case is equivalent to a 2D simulation. The remaining boundaries are assigned to inlet, outlet and wall. A laminar, stationary computation with a Reynolds number of $Re = 1$, based on the height of the inlet, $l = 0.1\,\mathrm{m}$, is performed. The inlet bulk velocity is set to $u_B = 1\,\frac{\mathrm{m}}{\mathrm{s}}$ and the kinematic viscosity to $\nu = 0.1\,\frac{\mathrm{m}}{\mathrm{s}^2}$. The considered cost functional is uniformity of the velocity at the outlet (3.38), with $|\underline{u}_d| = 3\,\frac{\mathrm{m}}{\mathrm{s}}$, on the centric third of the outlet, and $|\underline{u}_d| = 0\,\frac{\mathrm{m}}{\mathrm{s}}$ at the remaining outlet. In general, the cost functional uniformity of velocity is of importance when dealing with the optimization of ventilation components, as a homogeneous outflow increases passengers' comfort and system efficiency. The computational setup is depicted in Figure 6.16.
In the first step a primal simulation of the flow, governed by the RANS equations (3.32) and (3.33) including the Darcy term (3.32), is performed, using the solver *simpleFoam*, until a satisfactory convergence is achieved (5 000 iterations, normalized initial residuals fall below

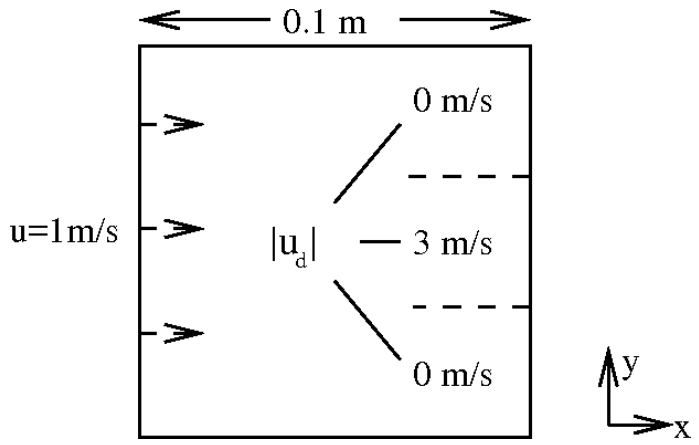

Fig. 6.16.: Computational domain with inlet (left), outlet (right) and wall (top and bottom). The desired velocity $\underline{u}_d$ takes different values at the outlet.

10^{-9}). The initial cost functional value before the optimization is $J_0 = 6.55445 \times 10^{-4}\ \frac{\mathrm{m}^5}{\mathrm{s}^2}$. In the second step, the adjoint RANS equations (4.106) and (4.107), including the Darcy term, are solved numerically.
The boundary terms arising from the cost functional are inserted into the boundary conditions for the adjoint velocity and pressure at the outlet, see (4.49) and (4.50),

$$\hat{p} = \rho u_n \hat{u}_n + \rho u_i \hat{u}_i + \mu_e \frac{\partial \hat{u}_n}{\partial n} + \left(u_n - |u_{i(d)}|\right) , \tag{6.12}$$

$$0 = \rho \hat{u}_{i(t)} u_n + \mu_e \frac{\partial \hat{u}_{i(t)}}{\partial n} + u_{i(t)} . \tag{6.13}$$

The equations are solved numerically up to a satisfactory convergence (normalized initial residuals below 10^{-5}). Hereby, no porosity modification is performed; the Darcy porosity term is constant $\alpha = 0\ \frac{\mathrm{kg}}{\mathrm{m}^3\mathrm{s}}$. The results for the primal and adjoint velocity and the integrand of the computed sensitivity are illustrated in Figure 6.17.
The computed sensitivity proposes to increase the porosity at lower and upper part of the outlet (negative sensitivity values in Figure 6.17, right), while the middle part of the outlet is supposed to stay fluid (positive sensitivity values in Figure 6.17, right). As the desired velocity is set to $|\underline{u}_d| = 3\ \frac{\mathrm{m}}{\mathrm{s}}$ in the centric third of the outlet and the velocity magnitude at this part is smaller ($u_n = 1.5\ \frac{\mathrm{m}}{\mathrm{s}}$, see Figure 6.17, left), the proposition of the sensitivity is reasonable as blocking the lower and upper part of the outlet increases the velocity at the center.

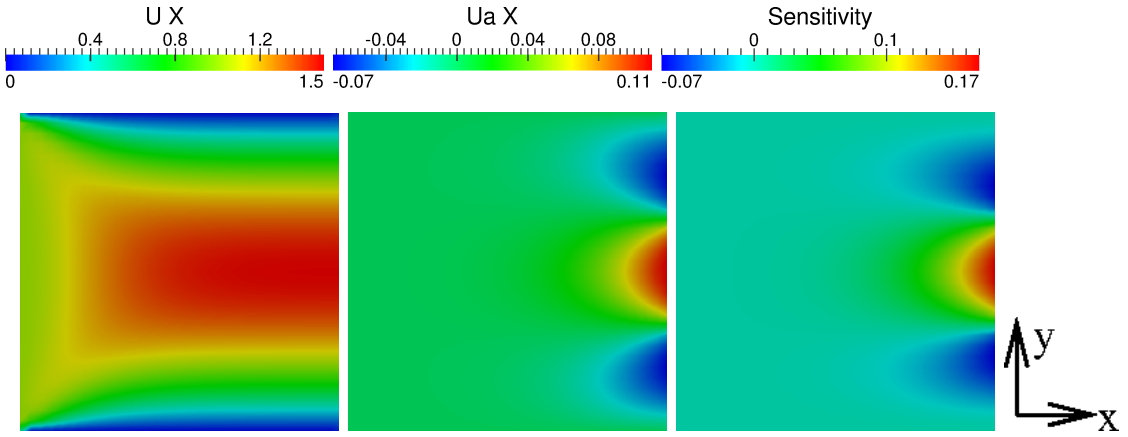

Fig. 6.17.: Primal (left) and adjoint (middle) velocity in x-direction and related sensitivity (right).

In the next step the step size λ is determined heuristically. The porosity is increased in regions where the sensitivity is negative. From the primal and adjoint simulation the minimum value of the sensitivity is determined, namely

$$\min_{P\in\Omega} \{\hat{u}_i^{(P)} u_i^{(P)} V^{(P)}\} = -7 \cdot 10^{-9}\,, \tag{6.14}$$

with $V = 1 \cdot 10^{-7}\,\mathrm{m}^3$. A maximum porosity change of 1 % of α_{max} is aimed in one update step. The maximum porosity value is set to $\alpha_{max} = 3\,000\,\frac{\mathrm{kg}}{\mathrm{m}^3\mathrm{s}}$. Therefore, the step size is computed from

$$\lambda \cdot 7 \cdot 10^{-9} = \frac{\alpha_{max}}{100}\,, \tag{6.15}$$

resulting in a step size in the order of magnitude between $\lambda = 10^9$ and $\lambda = 10^{10}$. The porosity distribution is optimized in the first step by setting $\epsilon = 0$, omitting the sparsity supporting term in the cost functional. Algorithm 2 is traversed in conjunction with a constant step size for the gradient descent. The design loop is repeated until the cost functional has reached a local minimum and does not change significantly. The computations reveal that the optimization performs best for a step size of $\lambda = 10^{11}$. Figure 6.18 shows the porosity distribution after the optimization cycle and the related cost functional progress. The final porosity distribution (Figure 6.18, left) represents a diffusor shape, with large porosity values at lower and upper part of the flow domain and zero porosity values in the middle of the domain. Concurrently with the development of the porosity values, the cost functional value decreases (Figure 6.18, right) during the design cycle. This behavior is reasonable, as large porosity values decrease the velocity, and, thus, the velocity is low in regions where $|\underline{u}_d| = 0\,\frac{\mathrm{m}}{\mathrm{s}}$ and high in the centric outlet region where $|\underline{u}_d| = 3\,\frac{\mathrm{m}}{\mathrm{s}}$ and $\alpha = 0\,\frac{\mathrm{kg}}{\mathrm{m}^3\mathrm{s}}$. The primal velocity before and after the porosity optimization is illustrated in Figure 6.19.

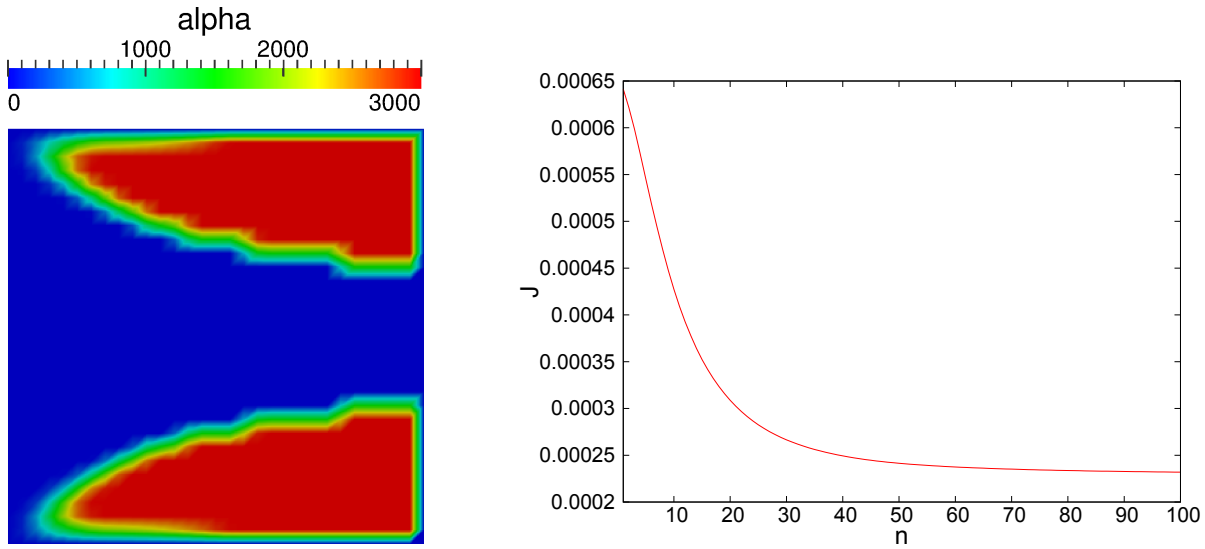

Fig. 6.18.: Porosity distribution (left) and cost functional progress (right) for the simulation without regularization ($\epsilon = 0$).

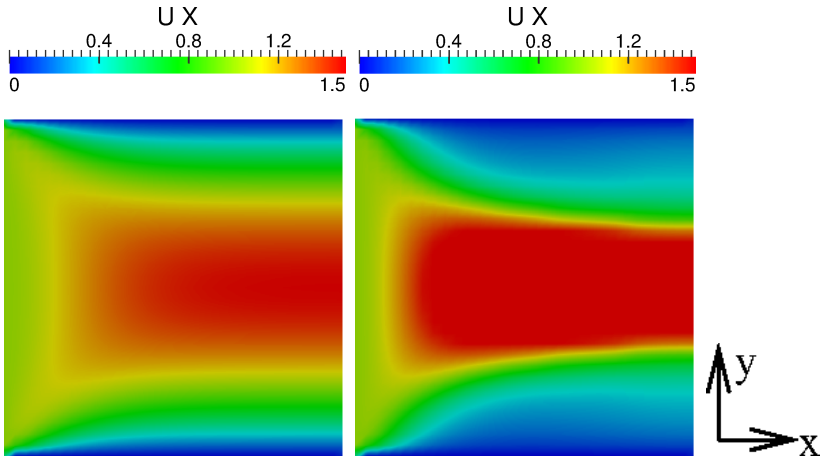

Fig. 6.19.: Primal x-velocity before (left) and after (right) the optimization (no regularization).

Figure 6.19 (left) displays large velocity values at the outlet in regions where $|\underline{u}_d| = 0\,\frac{\mathrm{m}}{\mathrm{s}}$. The velocity gradually reduces towards the wall boundary. For the optimized topology (Figure 6.19, right) the velocity value is maximum at the centric third of the outlet and low at upper and lower part of the outlet, due to the porosity distribution (Figure 6.18, left). The normalized cost functional value after the optimization is $J/J_0 = 0.34$, resulting in a large improvement of 66 %, relative to the initial cost functional value. In the next step it is examined if a sparse distribution of the porosity can be realized via insertion of the L^1-regularization term (4.124). The regularization term is inserted into the cost functional

such that the cost functional becomes

$$J = \int_{\Gamma_{out}} \frac{1}{2} \left(u - \underline{u}_d\right)^2 d\Gamma + \epsilon \int_{\Omega} |\alpha| \; d\Omega \,. \tag{6.16}$$

The approximation by the Huber function (4.125) may be omitted as the porosity values are positive and, thus, the L^1-regularization term is differentiable. In [19] it is shown that the results with the Huber approximation are similar for this case.
In the next step a value for the weighting factor ϵ is estimated. It is required to weight the regularization term in the same amount as the cost functional. Therefore, both should have the same order of magnitude. The maximum value of the cost functional uniformity of velocity is estimated at the outlet, by using the data from the primal simulation. The cost functional uniformity takes it maximum value for $u_i = (0.099 \quad 0.0 \quad 0.0)\,\frac{\mathrm{m}}{\mathrm{s}}$. The regularization term is maximal for $\alpha = \alpha_{max}$. Therefore, the weighting factor is computed from

$$\epsilon = \frac{\int_{\Gamma_{out}} \frac{1}{2} \left(u - \underline{u}_d\right)^2 d\Gamma}{\int_{\Omega} \alpha_{max} d\Omega} \approx 1.5 \cdot 10^{-2} \,. \tag{6.17}$$

To examine the behavior towards different weighting factors, the optimization is performed for $\epsilon = 1.5 \cdot 10^{-2}$, $\epsilon = 1.5 \cdot 10^{-3}$ and $\epsilon = 1.5 \cdot 10^{-4}$, using a step size $\lambda = 10^{11}$. Table 6.3 illustrates the normalized cost functional values for different values of ϵ.

Table 6.3.: Results for different values of ϵ.

	Relative cost functional value J/J_0	Improvement	$\alpha_{mean}/\alpha_{max}$
$\epsilon = 0$	0.34	66 %	0.45
$\epsilon = 1.5 \cdot 10^{-4}$	0.35	65 %	0.264
$\epsilon = 1.5 \cdot 10^{-3}$	0.41	59 %	0.117
$\epsilon = 1.5 \cdot 10^{-2}$	0.69	31 %	0.024

The results depict descending porosity values, simultaneous with the ascend of the weighting factor. For the maximum weighting factor $\epsilon = 1.5 \cdot 10^{-2}$ a sparse distribution ($\frac{\alpha_{mean}}{\alpha_{max}} = 0.024$) is obtained. For smaller weighting factors the amount of porosity also reduces from an initial value of $\frac{\alpha_{mean}}{\alpha_{max}} = 0.45$ for $\epsilon = 0$ to $\frac{\alpha_{mean}}{\alpha_{max}} = 0.264$ for $\epsilon = 1.5 \cdot 10^{-4}$ and $\frac{\alpha_{mean}}{\alpha_{max}} = 0.117$ for $\epsilon = 1.5 \cdot 10^{-3}$. The amount of porosity is almost reduced by a factor of two and four for $\epsilon = 1.5 \cdot 10^{-4}$ and $\epsilon = 1.5 \cdot 10^{-3}$, respectively. However, the improvement of the cost

functional only mildly reduces (from 66 % for $\epsilon = 0$ to 65 % for $\epsilon = 1.5 \cdot 10^{-4}$ and 59 % for $\epsilon = 1.5 \cdot 10^{-3}$). For the largest considered weighting factor ($\epsilon = 1.5 \cdot 10^{-2}$), the amount of control reduces by a factor of 18, still delivering a cost functional improvement of 31 %. Figure 6.20 shows the porosity distribution and related velocities for different values of ϵ.

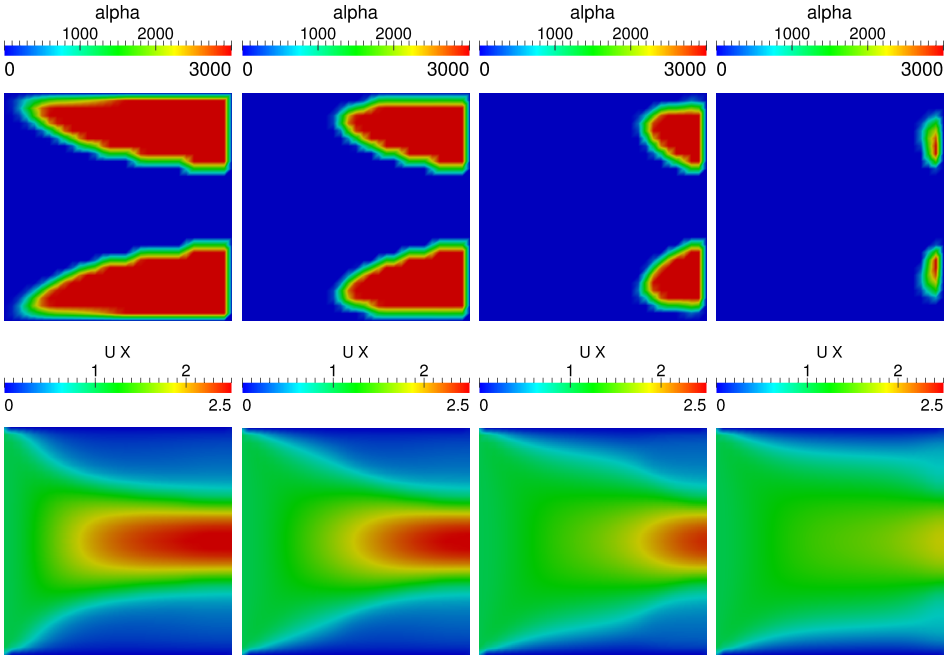

Fig. 6.20.: Porosity distribution (top) and related streamwise velocity (bottom) for $\epsilon = 0$, $\epsilon = 1.5 \cdot 10^{-4}$, $\epsilon = 1.5 \cdot 10^{-3}$ and $\epsilon = 1.5 \cdot 10^{-2}$ (from left to right).

With increasing weighting factor ϵ the distribution becomes sparser (Figure 6.20, top). Concurrently with the porosity development, the velocity profile turns out to be closer to the desired velocity for increasing weighting factors (Figure 6.20, bottom). As the results demonstrate, the insertion of the regularization term helps to determine porosity regions having a high impact on the cost functional.

Bifurcating Channels

The second validation case refers to the same domain (of the size 0.3 m $\times$ 0.3 m) and discretization, with two outlets at the top and the bottom of the right-hand side face. Due to simulation reasons, a third z-axis is included with $\Delta z = 0.01\,\mathrm{m}$, consisting of a single layer of cells. As before, the patch type for the front and rear patch is set to *empty*, therefore, the case is equivalent to a 2D simulation. A stationary, laminar computation with a Reynolds number of $Re = 50$ is performed, based on the reference velocity $|\underline{u}_{ref}| = 50\frac{\mathrm{m}}{\mathrm{s}}$ at one third of the inlet, a reference length of $l = 0.1\,\mathrm{m}$ and a kinematic viscosity of $\nu = 0.1\frac{\mathrm{m}}{\mathrm{s}^2}$. The boundaries are set to inlet, outlet and wall, as usual. The cost functional dissipated power (3.40) through the device boundary is an important quantity to judge the

system efficiency and is thus considered in this case. The computational setup is depicted in Figure 6.21

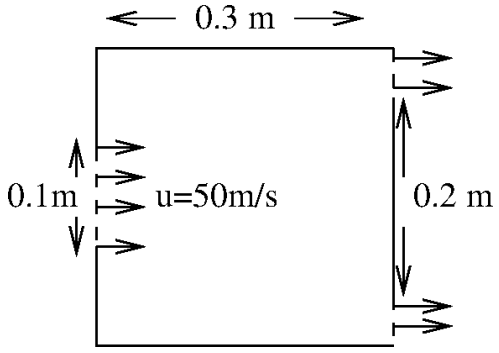

Fig. 6.21.: Computational domain. Constant velocity at one third of the inlet (left), two outlets (right).

A primal simulation of the flow, governed by the RANS equations including the Darcy term (3.32) and (3.33), is performed, using the solver *simpleFoam* until a satisfactory convergence is achieved (5 000 iterations, normalized initial residuals fall below 10^{-8}). The initial cost functional value before the optimization is $J_0 = 89.7204\,\frac{\mathrm{m}^6}{\mathrm{s}^3}$. Based on the primal solution, the adjoint equations, including the Darcy term (4.106) and (4.107), are solved numerically. The Darcy term is set to constant zero in the first place and not modified. The boundary terms arising from the cost functional are inserted into the boundary conditions for the adjoint velocity and pressure at the outlet, see (4.49) and (4.50),

$$\hat{p} = \rho u_n \hat{u}_n + \rho u_i \hat{u}_i + \mu_e \frac{\partial \hat{u}_n}{\partial n} - \frac{1}{2} u_i u_i - {u_n}^2 \,, \tag{6.18}$$

$$0 = \rho \hat{u}_{i(t)} u_n + \mu_e \frac{\partial \hat{u}_{i(t)}}{\partial n} - \rho u_{i(t)} u_n \,, \tag{6.19}$$

and inlet (4.47)

$$\hat{u}_n = \frac{1}{\rho} u_n \,. \tag{6.20}$$

The equations are solved numerically up to a satisfactory convergence (normalized initial residuals fall below 10^{-8}). The result for the primal and adjoint velocity and the integrand of the computed sensitivity (4.111) are illustrated in Figure 6.22
The computed sensitivity proposes to increase the porosity in regions where only little flow activity is present (negative values of the sensitivity in Figure 6.22, right; low velocity values at Figure 6.22, left). In regions where a high flow activity is present, the sensitivity proposes to let the porosity stay zero, corresponding to fluid media (positive values of the sensitivity in Figure 6.22, right; large velocity values at Figure 6.22, left). The proposition of the sensitivity is reasonable, as blocking dead water regions increases the system efficiency and thus improves the dissipated power cost functional.

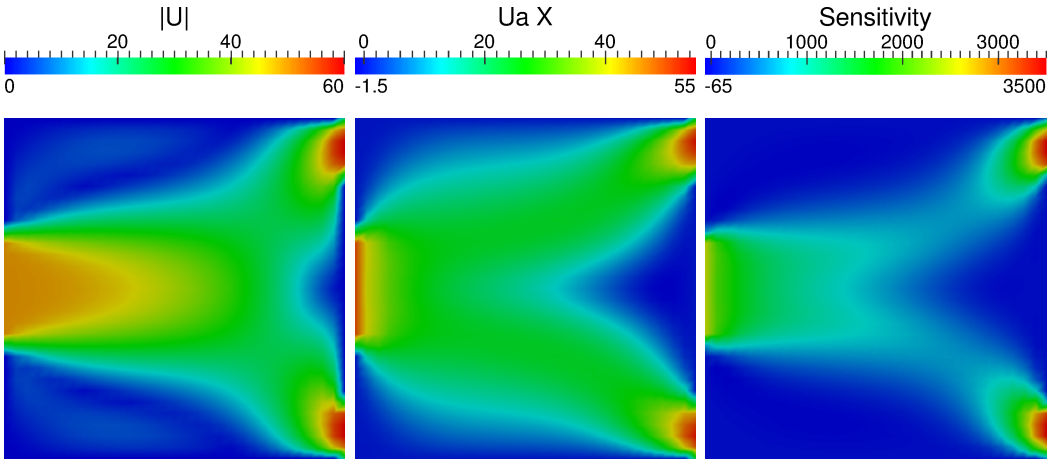

Fig. 6.22.: Magnitude of primal velocity (left), adjoint x-velocity (middle) and related sensitivity (right).

Porosity modification is applied to reach a local minimum of the cost functional. The maximum porosity value is set to $\alpha_{max} = 10\,000\,\frac{\mathrm{kg}}{\mathrm{m^3 s}}$. In the first step the step size λ is computed heuristically, analogously to the preceding test case. The maximum, negative value of the sensitivity is

$$\min_{P\in\Omega}\{\hat{u}_i^{(P)} u_i^{(P)} V^{(P)}\} = -6.5 \cdot 10^{-5}\,, \tag{6.21}$$

with $V = 1 \cdot 10^{-6}\,\mathrm{m}^3$. A maximum porosity change of 1 % of α_{max} is aimed in one update step, therefore, the step size is determined from

$$\lambda \cdot \hat{u}_i u_i V = \frac{\alpha_{max}}{100}\,, \tag{6.22}$$

resulting in a step size of approximately $\lambda = 10^6$. The porosity distribution is improved in the first step by setting $\epsilon = 0$, omitting the sparsity supporting term in the cost functional. Algorithm 2, combined with a constant step size for the gradient descent, is traversed until the cost functional reaches a local minimum and does not change significantly. Figure 6.23 illustrates the porosity distribution after the optimization cycle and the cost functional progress. The final porosity distribution (Figure 6.23, left) depicts a bifurcation, guiding the flow to the upper and lower part of the outlet, where it flows out of the domain. Concurrently with the porosity development, the cost functional decreases (Figure 6.23, right). The development of the cost functional is reasonable, as the final topology enables to efficiently guide the flow through the device boundary, and, thus, lowers the dissipated power. The normalized cost functional value after the optimization is $J/J_0 = 0.94$, representing an improvement of 6 %, relative to the initial cost functional value.

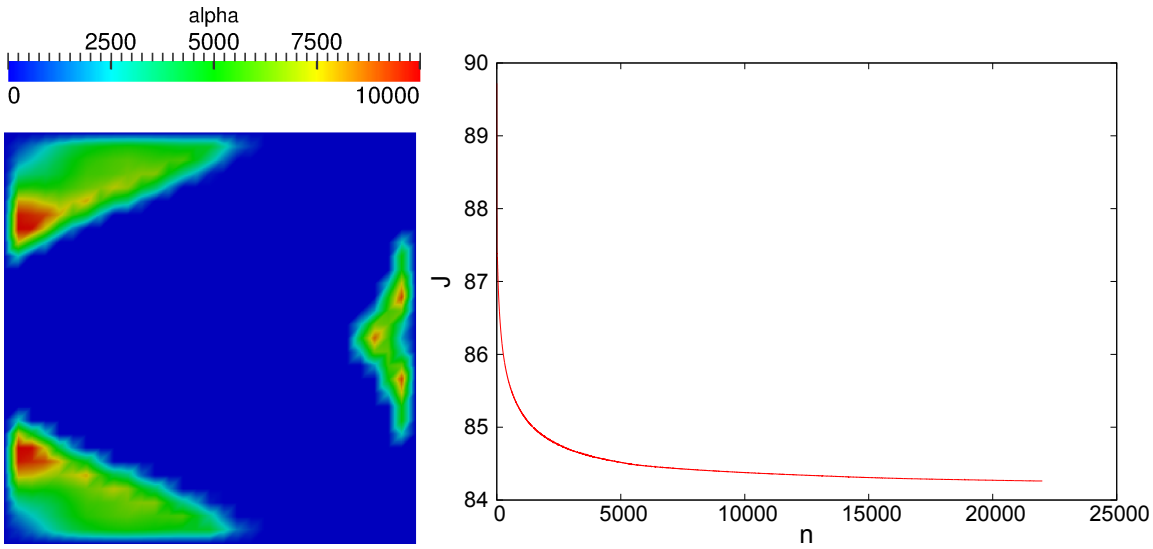

Fig. 6.23.: Porosity distribution (left) and cost functional progress (right).

To promote a sparse distribution of the control, the L^1-regularization term (4.124) is inserted into the cost functional such that the cost functional becomes

$$J = -\int_\Gamma \left(\frac{p}{\rho} + \frac{1}{2}u_i u_i\right) u_n d\Gamma + \epsilon \int_\Omega |\alpha| \, d\Omega \,. \tag{6.23}$$

As the porosity values only take positive values, the regularization term is differentiable. In the next step a value for the regularization weighting factor ϵ is estimated, such that both, cost functional and regularization term, have the same order of magnitude. The cost functional dissipated power takes it maximum value at the outlet for $|\underline{u}| = 60\,\frac{\mathrm{m}}{\mathrm{s}}$, $\frac{p}{\rho} = 0\,\frac{\mathrm{m}^2}{\mathrm{s}^2}$ and at the inlet for $|\underline{u}| = 50\,\frac{\mathrm{m}}{\mathrm{s}}$, $\frac{p}{\rho} = 2\,000\,\frac{\mathrm{m}^2}{\mathrm{s}^2}$. The regularization term is maximum for $\alpha = \alpha_{max}$. Therefore, the weighting factor is computed from

$$\epsilon = \frac{\int_\Gamma (\frac{p}{\rho} + \frac{1}{2}u_i u_i) u_n d\Gamma}{\int_\Omega \alpha_{max} d\Omega} \approx 65 \,. \tag{6.24}$$

To validate the behavior for different weighting factors, the optimization is performed for $\epsilon = 0$, $\epsilon = 0.065$, $\epsilon = 0.65$, $\epsilon = 6.5$ and $\epsilon = 65$, using a step size $\lambda = 10^6$. Figure 6.24 shows the porosity distribution for different values of ϵ.
Increasing the weighting factor ϵ leads to a sparser distribution. For $\epsilon = 65$ almost no control is apparent (Figure 6.24, right). Also for a comparatively small weighting factor ($\epsilon = 0.65$), the amount of porosity notably decreases (Figure 6.24, second picture from left). Table 6.4 displays the numerical results, including the corresponding cost functional values.

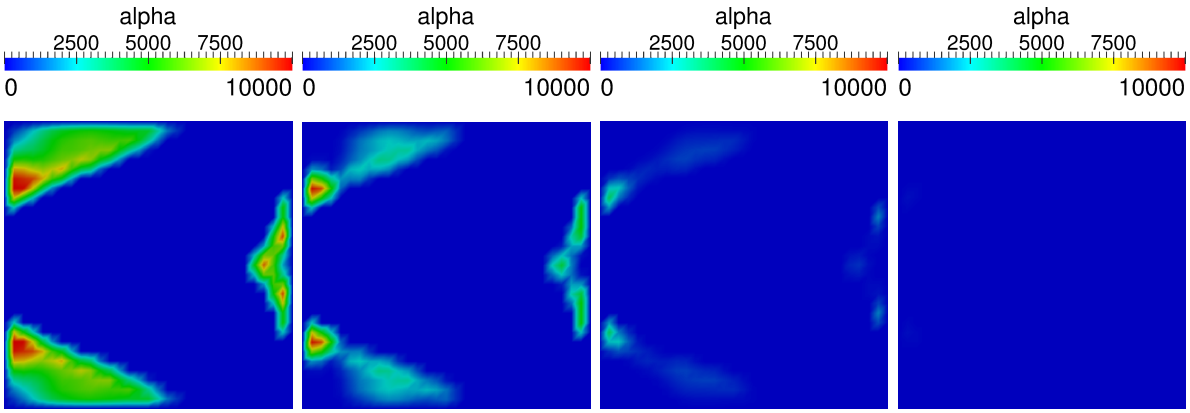

Fig. 6.24.: Porosity distribution for $\epsilon = 0$, $\epsilon = 0.65$, $\epsilon = 6.5$ and $\epsilon = 65$.

Table 6.4.: Results for different values of ϵ.

	Relative cost functional value J/J_0	Improvement	$\frac{\alpha_{mean}}{\alpha_{max}}$
$\epsilon = 0$	0.94	6 %	0.13
$\epsilon = 0.065$	0.94	6 %	0.11
$\epsilon = 0.65$	0.945	5.5 %	0.05
$\epsilon = 6.5$	0.97	3 %	0.01
$\epsilon = 65$	0.9988	0.12 %	0.00016

Though the amount of control is reduced by almost a factor of three (for $\epsilon = 0.0$, $\frac{\alpha_{mean}}{\alpha_{max}} = 0.13$ and $\epsilon = 0.65$, $\frac{\alpha_{mean}}{\alpha_{max}} = 0.05$), the improvement of the cost functional only mildly reduces (from 6 % to 5.5 %). Lower values of ϵ only slightly reduce the amount of porosity ($\frac{\alpha_{mean}}{\alpha_{max}} = 0.11$ for $\epsilon = 0.065$), while still delivering the same amount of improvement (6 %). A larger weighting factor leads to a heavy reduction of the mean porosity by a factor of 13 ($\frac{\alpha_{mean}}{\alpha_{max}} = 0.01$ for $\epsilon = 6.5$), still, the cost functional improvement is existent (3 %). For an even larger value of $\epsilon = 65$, almost no porosity is present ($\frac{\alpha_{mean}}{\alpha_{max}} = 0.00016$), accordingly, the cost functional experiences almost no improvement (0.12 %).
In both cases (diffusor and bifurcating channels), the insertion of the regularization leads to a reduction of the porosity amount, but still delivers a sufficient cost functional improvement. Generally, the method may successfully be applied to cases where the amount of control is related to costs, as regions with highest impact on the cost functional are determined. To that effect, the insertion may be applied to cases where it has to be decided *where* to put the control (see also Stadler [76]). However, the approach is not capable of

yielding a digital distribution. The regularization helps to reduce the amount of control but does in general not reduce regions with intermediate control values. For this goal, different approaches should be studied. The method is however very valuable from an engineering point of view. The porosity is often associated with significant weights; a drastic reduction of weight without significant compromises on the cost functional is very appreciated. Examples refer to aerospace industry where weight reductions are crucial.

7. Application

In this chapter the adjoint sensitivity analysis is applied to 3D turbulent industrial cases. The first section presents the results of the adjoint shape optimization, employed to improve the uniformity of flow for a cabin air outlet of an aircraft. In the second section the results of the optimization of a mixing chamber to heat the ventilated air flows of an aircraft are displayed. The cost functional refers to the mixing efficiency in buoyancy-driven flows. Adjoint topology optimization of the cost functional uniformity of flow is applied to two cabin air outlets of aircrafts in the third and fourth section. Hereby, the focus lies on different step size computations for the gradient descent and the insertion of a regularization term to promote a sparse distributed control.

7.1. Shape Optimization of Do728-KLA

The first application for the adjoint shape optimization is a cabin air outlet of a Dornier 728 aircraft (Do728-KLA). The numerical results are validated experimentally with Particle Image Velocimetry (PIV) measurements. The results presented were developed during the cooperation with the German Aerospace Center, published in [48].
The upstream geometry of the cabin air outlet consists of a 178 mm long circular duct with a diameter of 57 mm, followed by a 185 mm (length) $\times$ 1 000 mm (width) $\times$ 165 mm (height) angled chamber, including a deflector and 17 perforated plates, and subsequently 17 air outlets (see Figure 7.1, left). To simulate a realistic outflow behavior, a box is added to the geometry ((see Figure 7.1, right). The boundaries of the box are assigned to outlet and wall. Here, the outlet consists of the vertical face at the right hand-side of the geometry (see Figure 7.1, right).

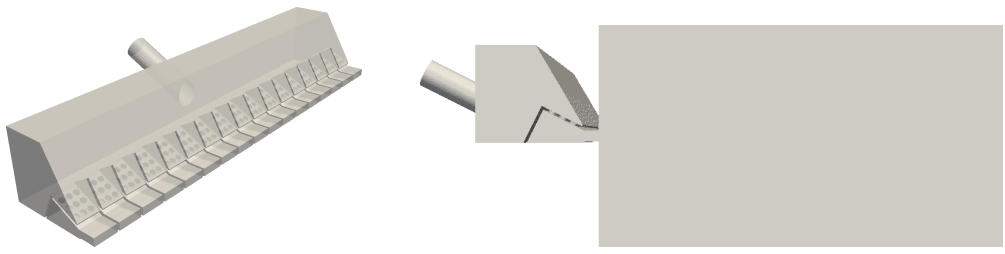

Fig. 7.1.: Geometry of the cabin air outlet Do728, with box (right) for simulating the outflow.

The mesh without the plenum consists of roughly seven million unstructured tetrahedrons.

Mesh generation has been accomplished using ANSA [4]. The governing equations are the incompressible RANS equations (3.8), (3.9). The Reynolds-number, based on the diameter of the pipe, is $Re = 27\,000$ with an inlet bulk velocity of $u_B = 7\,\frac{\mathrm{m}}{\mathrm{s}}$ and a kinematic viscosity of $\nu = 1.49 \cdot 10^{-5}\,\frac{\mathrm{m}^2}{s}$. Turbulence is modeled via the high-Re SST $k-\omega$ turbulence model (3.10)–(3.12). Besides, the boundaries are assigned to typical ducted flow properties, consisting of inlet, outlet, and wall. The objective is to minimize the cost functional uniformity of the velocity at the outlet (3.38), evaluated at the outlet segments with respect to a desired velocity $\underline{u}_d$. The desired velocity $\underline{u}_d$ is set to $|\underline{u}_d| = 0.8916\,\frac{\mathrm{m}}{\mathrm{s}}$ in normal direction of the outlet, to ensure mass conservation. The cost functional is associated to a contribution to the adjoint boundary conditions (4.49), (4.50), turning to

$$\hat{p} = \rho u_n \hat{u}_n + \rho u_i \hat{u}_i + \mu_e \frac{\partial \hat{u}_n}{\partial n} + \left(u_n - |u_{i(d)}|\right) \qquad \text{on} \quad \Gamma_{out}\,, \tag{7.1}$$

$$0 = \rho \hat{u}_{i(t)} u_n + \mu_e \frac{\partial \hat{u}_{i(t)}}{\partial n} + u_{i(t)} \qquad \text{on} \quad \Gamma_{out}\,, \tag{7.2}$$

as the desired velocity points in outlet-normal direction. The design boundary consists of the basement of the chamber and the deflector (see Figure 7.2).

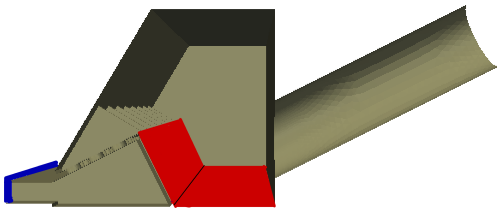

Fig. 7.2.: Geometry of Do728-KLA. Surfaces enabled for the shape modification marked in red, objective surface marked in blue.

Steady state simulations, solving primal (3.8), (3.9) and adjoint (4.42), (4.43) RANS equations, are executed by using the solver *simpleFoam* of OpenFOAM®. Hereby, the SIMPLE algorithm and its adjoint analogue are repeated until a satisfactory convergence is achieved (normalized initial residuals below 10^{-6} for primal and adjoint fields after 5 000 iterations). The cost functional is evaluated for the mesh with a plenum behind the cabin air outlet (Figure 7.1, right) in a cell zone (Figure 7.2), corresponding to the outlet of the mesh without plenum (Figure 7.1, left), and is normalized by the volume of the cell zone. The evaluation of the cost functional for the initial design results in a value of $J_0 = 0.08027\,\frac{\mathrm{m}^2}{\mathrm{s}^2}$. Figure 7.3 displays the velocity magnitude at the outlet of the Do728-KLA and related streamtracers for the initial configuration. The velocity magnitude is large at both sides of the cabin air outlet, while it is small in the center, as depicted in Figure 7.3. The flow collides against the deflection plate and spreads to the sides, resulting in the depicted velocity distribution. The solution of the primal and the corresponding adjoint incompressible Reynolds-averaged Navier-Stokes equations leads to the sensitivity (4.60), that indicates, how body contours should be modified to obtain an improvement of the cost functional. The computed sensitivity is displayed in Figure 7.4 (left).

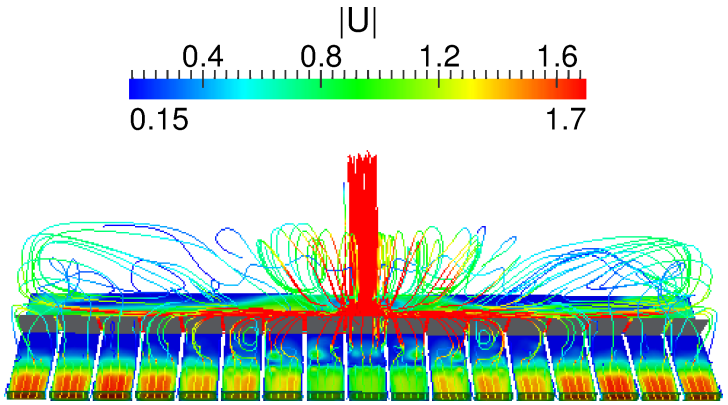

Fig. 7.3.: Velocity magnitude and related streamtracers for simulated flow at Do728-KLA.

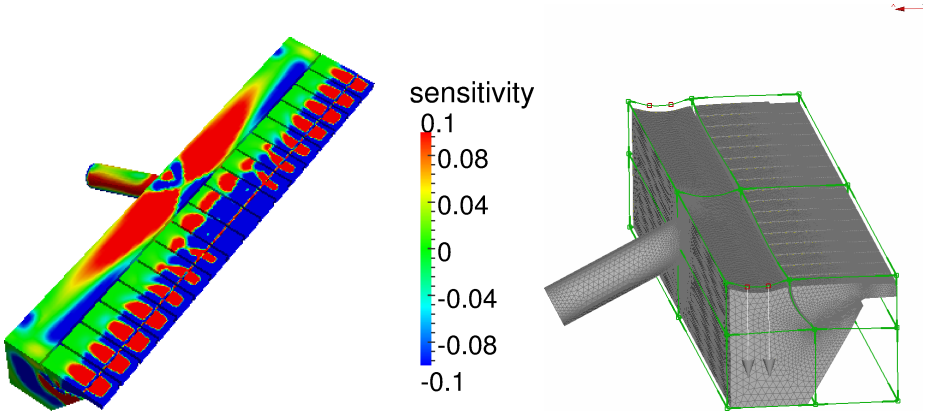

Fig. 7.4.: Contour plot of sensitivity for original geometry (left) and morphing model with optimized geometry (right) of the cabin air outlet Do728-KLA. The deformation of the surface mesh is intensified in the center of the cabin air outlet.

The sensitivity induces an inward movement of the center of the basement. Compacting the centric part of the outlet leads to a magnification of the present velocity field. Due to the small velocity magnitude in the centric part of the air outlet (Figure 7.3), the proposed deformation results in a more homogeneous outflow. The shape modification is realized by means of the commercial software ANSA [4]. In this way, the sensitivity is automatically mapped to the morphing parameters of ANSA [4] and the mesh is morphed accordingly (see Figure 7.4, right). Figure 7.5 displays the cross section for the distinct designs. The inward movement of the basement increases from design step to design step (see Figure 7.5). The deformation is accomplished along the whole basement and deflection plate while it is most intense at the centric part.
The cost functional evaluation for the modified design results in a value of $J/J_0 = 0.89$ (normalized by the initial cost functional value). Thus, an improvement of 11 %, compared to the initial value of the cost functional, is achieved. As the optimization technique steps towards a local minimum with every design cycle, a second design cycle based on the

Fig. 7.5.: Cross Section of Do728-KLA for the original design (left), first (middle) and second (right) redesign.

morphed mesh and the related primal and adjoint velocity fields is performed, leading to an improvement of 13 % ($J/J_0 = 0.87$), compared to the initial configuration, resulting in a further improvement of 2 %. The total pressure loss improves 1 % compared to the initial configuration. Figure 7.6 illustrates the results for the velocity magnitude of the initial geometry and of the deformed geometries at one line ($z = 0.01157\,\mathrm{m}$) along half of the outlet ($y = [0, 0.5]\,\mathrm{m}$).

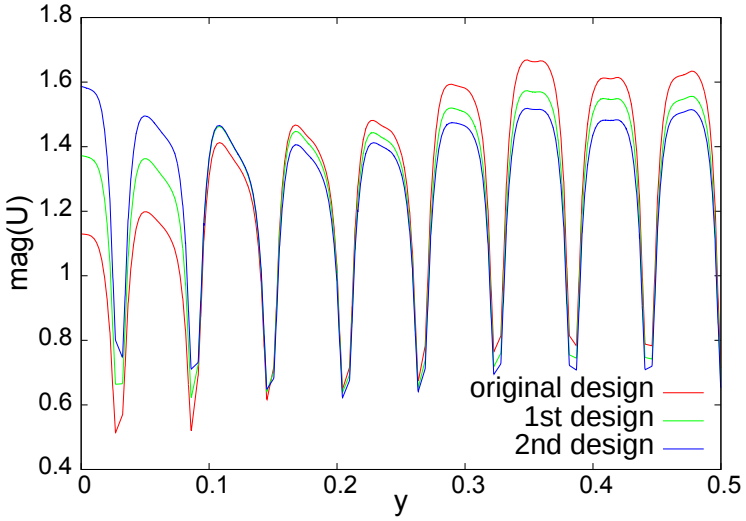

Fig. 7.6.: Velocity magnitude along one half of the outlet for different shapes.

Figure 7.6 clearly depicts the improved homogeneity for the first and second design. To validate the results of the RANS simulation, the homogeneity of the flow velocity of the original and the improved air outlet is investigated experimentally using PIV, see [68]. To conduct PIV, the fluid is seeded with tracer particles, small enough to follow the flow. The particles are illuminated with a planar laser beam. The inlet bulk velocity is $u_B = 7\,\frac{\mathrm{m}}{\mathrm{s}}$. Two pictures of the particles are taken with a small time difference. Using the software PIVview, the flow velocity field is calculated from the particle displacement, computed from two pictures taken at different times. The experimental setup is depicted in Figure 7.7 and consists of a Nd:YAG laser, whose beam is shaped with a light-sheet optic to illuminate the measurement region.

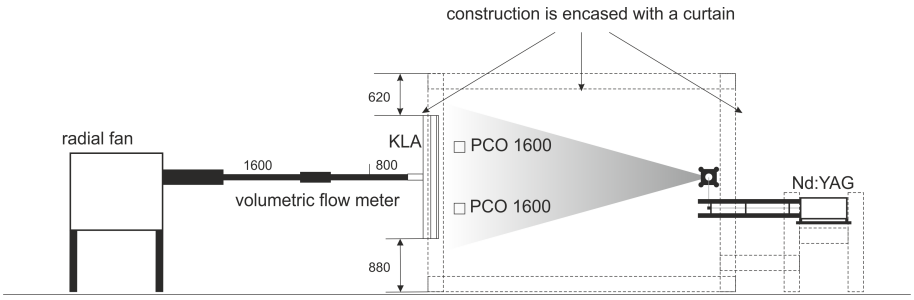

Fig. 7.7.: PIV measurement setup.

The air flowing through the outlet is supplied by a radial fan and the flow velocity is measured with a volumetric flow meter. The cutting plane is positioned orthogonal and central to the outlet segments. Furthermore, DEHS seeding (see Table 7.1) is added to the flow at the inlet of the radial fan. Due to safety reasons and to prevent external influences on the studied flow, the setup is encased with a curtain to avoid scattered light. All details of the PIV measurement are listed in Table 7.1.

Table 7.1.: PIV measurement parameters.

Laser	2× neodymium-doped yttrium aluminum garnet (N_d:YAG) laser 532 nm 350 mJ, repetition rate 10 Hz
Cameras	2× PCO1600, resolution: 1 600×1 200 pixel
Light-sheet optics	−150 mm biconcave, 300 mm, F 100 mm Zyl.
Scattering particles	Di-Ethyl-Hexyl-Sebacat (DEHS) particles, size: 0.5–1.5 μm
Volume-flow rate	287–4 300 $^{l}/_{min}$ with an accuracy of +/− 2.5 %, typical: 1 080 $^{l}/_{min}$
Fan	steplessly variable radial fan
Fabrication of the outlet	rapid prototyping with PA2200
Field of view	2 × 600 mm×420 mm
Interrogation window	12×12 mm
# Averaged vector fields	694
Vector distance	6×6 mm

Figure 7.8 presents a comparison of the measured velocity fields in horizontal planes. Regarding the homogeneity of the flow, the original and the improved outlet geometries produce considerably different velocity distributions. The averaged velocity field of the original outlet, shown in Figure 7.8 (left), is characterized by pronounced maxima, whereas the flow of the modified outlet is more homogeneous (see Figure 7.8, right).
In Figure 7.9 the relative deviation to the averaged velocity, obtained from the PIV measurement, is directly compared to the relative deviation obtained from the numerical simulations, respectively, at a distance of 5 cm from the air outlet.

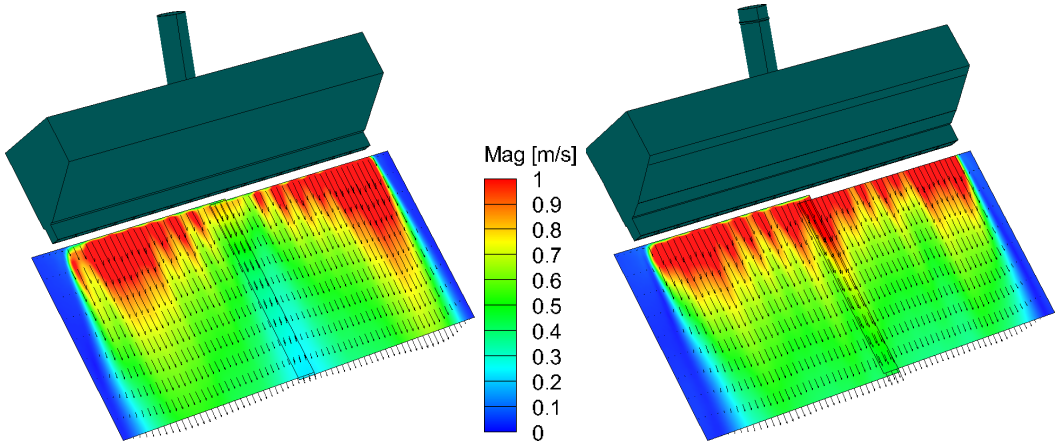

Fig. 7.8.: PIV velocity field, for original (left) and improved (right) outlet in horizontal planes.

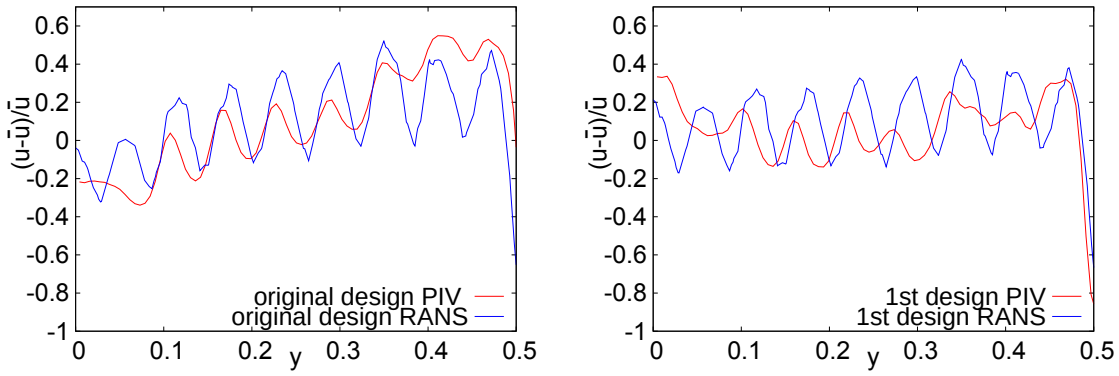

Fig. 7.9.: Comparison of the computed and measured relative deviation of the velocity magnitude to the averaged velocity magnitude in the center of the outlet plane for the initial (left) and the modified (right) design.

The relative deviation, obtained from the experiments, is comparable to the relative deviation from the numerical simulations (see Figure 7.9). The differences can be explained by measuring inaccuracy and modeling errors in the RANS calculation. However, both results clearly show the improvement of the homogeneity at the outlet. Therefore, the experiments confirm the geometrical modification, induced by the adjoint sensitivity. Hence, in spite of the performed simplifications (neglect of the advection term, frozen turbulence), the adjoint sensitivity analysis leads to a significant improvement of the cost functional.

7.2. Shape Optimization of Mixing Chamber

The second application case for the adjoint shape optimization is a mixing chamber. The mixing chamber aggregates warm air, supplied from the cabin, and cool air, supplied from the ventilation components. The flow leaves the chamber through several exits, connected

to distinct compartments of the aircraft. Therefore, the flow in the mixing unit is affected by temperature changes, modeled by the buoyancy driving force inserted at the right-hand side of the momentum equation. Accordingly, the temperature field is computed, by solving the related internal energy equation. In Figure 7.10, the geometry of the mixing chamber with its tapped inlets and exits is illustrated.

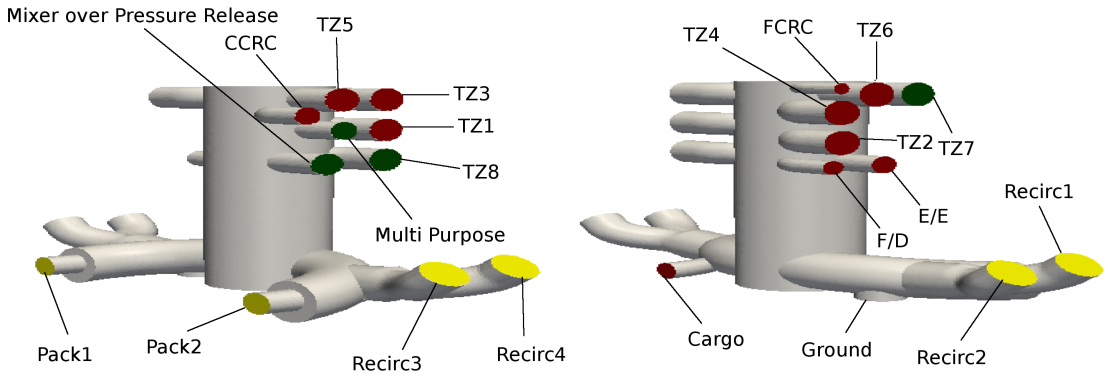

Fig. 7.10.: Front (left) and back (right) side of mixing chamber with tapped inlets (yellow), walls (green) and outlets (red).

For data protection reasons, the geometry in Figure 7.10 is distorted and the dimensions are omitted. The mixing unit is supplied by two equally designed premixing units, connected to the recirculation system (Recirc1–Recirc4) and the by the air generation system (Pack1, Pack2), as depicted in Figure 7.10. The four lateral recirculation accesses (Recirc1–Recirc4) guide the air from the cabin into the chamber. Air from the air-conditioning is blown in via the two Pack accesses. Subsequently, the air leaves the chamber through the outlets at the top of the chamber. Tapped to the mixer unit are 11 outlets (Temperature zones (TZ) 1-6, Flight Deck (F/D), Overhead Flight Crew Rest Compartment (FCRC), Overhead Cabin Crew Rest Compartment (CCRC), Cargo Hold (CRG), Avionics backup supply (E/E)), see also Figure 7.10. Several configurations depending on the number of passengers, seated in the cabin, exist. It is distinguished in manual/normal/low/high workload. In the considered case a normal workload is assumed for an aircraft with a moderate amount of space for passengers (NORM-800). The temperature zones TZ7 and TZ8 are closed, as these zones do not exist for smaller aircrafts. Furthermore, the exits Multi Purpose, Mixer over Pressure Release and Ground are closed. Different temperatures, leading to buoyancy effects, have to be taken into account in the flow model. The governing equations are the incompressible RANS-F equations (3.25)–(3.27). The Reynolds number is $Re = 130\,000$. Turbulence is modeled via the high-Re SST $k-\omega$ turbulence model (3.10)–(3.12).
In Table 7.2, 7.3 and 7.4 the boundary conditions for outlet, wall and inlet, used in the simulation are stated. The values of the volume flow rate and the temperature are normalized by their maximum values.

Table 7.2.: Outlet boundary conditions for mixing chamber.

Γ_{out}	TZ1	TZ2	TZ3	TZ4	TZ5	TZ6
Pressure	$\frac{\partial p}{\partial n} = 0$	$\frac{\partial p}{\partial n} = 0$	$\frac{\partial p}{\partial n} = 0$	$\frac{\partial p}{\partial n} = 0$	$\frac{\partial p}{\partial n} = 0$	$\frac{\partial p}{\partial n} = 0$
Normalized volume flow rate	0.59	0.5	0.6	0.47	0.55	0.53
Temperature	$\frac{\partial T}{\partial n} = 0$	$\frac{\partial T}{\partial n} = 0$	$\frac{\partial T}{\partial n} = 0$	$\frac{\partial T}{\partial n} = 0$	$\frac{\partial T}{\partial n} = 0$	$\frac{\partial T}{\partial n} = 0$
Γ_{out}	F/D	FCRC	CCRC	CRG	E/E	
Pressure	$\frac{\partial p}{\partial n} = 0$	$\frac{\partial p}{\partial n} = 0$	$\frac{\partial p}{\partial n} = 0$	$\frac{\partial p}{\partial n} = 0$	$\frac{\partial p}{\partial n} = 0$	
Normalized volume flow rate	0.16	0.04	0.34	0.34	0.28	
Temperature	$\frac{\partial T}{\partial n} = 0$	$\frac{\partial T}{\partial n} = 0$	$\frac{\partial T}{\partial n} = 0$	$\frac{\partial T}{\partial n} = 0$	$\frac{\partial T}{\partial n} = 0$	

Table 7.3.: Wall boundary conditions for mixing chamber.

Γ_w	Mixer over Pressure Release	Multi Purpose	Ground	Mixer	TZ7	TZ8
Pressure	$\frac{\partial p}{\partial n} = 0$	$\frac{\partial p}{\partial n} = 0$	$\frac{\partial p}{\partial n} = 0$	$\frac{\partial p}{\partial n} = 0$	$\frac{\partial p}{\partial n} = 0$	$\frac{\partial p}{\partial n} = 0$
Velocity	$0\,\frac{\mathrm{m}}{\mathrm{s}}$	$0\,\frac{\mathrm{m}}{\mathrm{s}}$	$0\,\frac{\mathrm{m}}{\mathrm{s}}$	$0\,\frac{\mathrm{m}}{\mathrm{s}}$	$0\,\frac{\mathrm{m}}{\mathrm{s}}$	$0\,\frac{\mathrm{m}}{\mathrm{s}}$
Normalized temperature	0.95	0.95	0.95	0.95	0.95	0.95

Table 7.4.: Inlet boundary conditions for mixing chamber.

Γ_{in}	Recirc1–Recirc4	Pack1&Pack2
Pressure	$\frac{\partial p}{\partial n} = 0$	$\frac{\partial p}{\partial n} = 0$
Normalized volume flow rate	0.6	1
Normalized temperature	1	0.91& 0.87

Wall functions are employed to compute the turbulence properties. A turbulence intensity of $I = 0.2$ and a mixing length of $\ell = 0.045\,\mathrm{m}$ is used. The Boussinesq equation models the density with a reference density of $\rho = 1.2615\,\frac{\mathrm{kg}}{\mathrm{m}^3}$ and a normalized reference temperature of $\frac{T_{ref}}{T_{max}} = 0.95$. The operating pressure is set to $p = 1\,013\,\mathrm{mbar}$. Other physical properties are set to standard conditions of air, i.e. an isochore heat capacity, $c_v = 718\,\frac{\mathrm{J}}{\mathrm{kgK}}$, and a thermal expansion coefficient $\beta_T = 3.5714 \cdot 10^{-3}\,\frac{1}{\mathrm{K}}$. The Prandtl number is set to $Pr = 0.71826$, the turbulent Prandtl number to $Pr_t = 0.7$. Mesh generation has been performed by ANSA

[4], providing roughly one million unstructured, tetrahedral cells. The goal is to improve the mixing efficiency at the outlets via adjoint shape optimization to supply homogeneous temperature levels to all temperature zones in the cabin, formulated as

$$J = \int_{\Gamma_{out}} \frac{1}{2}(T - T_d)^2 \rho u_i d\Gamma = \frac{1}{2} \sum_{f \in \Gamma_{out}} (T^{(f)} - T_d)^2 \dot{m}_f \,. \tag{7.3}$$

Hereby, the mixing efficiency is considered mass flow enhanced. The desired temperature T_d is considered as averaged temperature over all exits, namely

$$T_d = \sum_{f \in \Gamma_{out}} \frac{T^{(f)} A^{(f)}}{A_{out}} \,. \tag{7.4}$$

A small value of the cost functional implies a more efficient mixing in the chamber, as the temperature distribution is more homogeneous. The cost functional is defined at the outlets of the chamber, therefore, the adjoint boundary conditions (4.94) are adapted accordingly with the cost functional derivative, viz.

$$\rho \hat{T} u_n + \kappa_{eff} \frac{\partial \hat{T}}{\partial n} + (T - T_d)\, \rho u_i = 0 \quad \text{on} \quad \Gamma_{out} \,. \tag{7.5}$$

Steady state simulations, solving primal (3.25)–(3.27) and adjoint (4.82)– (4.84) RANS-F equations, are performed with the solver *buoyantBoussinesqSimpleFoam* and its adjoint analogue in OpenFOAM®. The solver uses the Boussinesq approximation (3.24) to model the buoyancy and the SIMPLE algorithm (Algorithm 3) to couple pressure and velocity. The reference temperature is computed at each iteration as average value over all outlets and treated as constant in the adjoint equation system. Figure 7.11 displays the result for the normalized velocity and temperature for the original design.

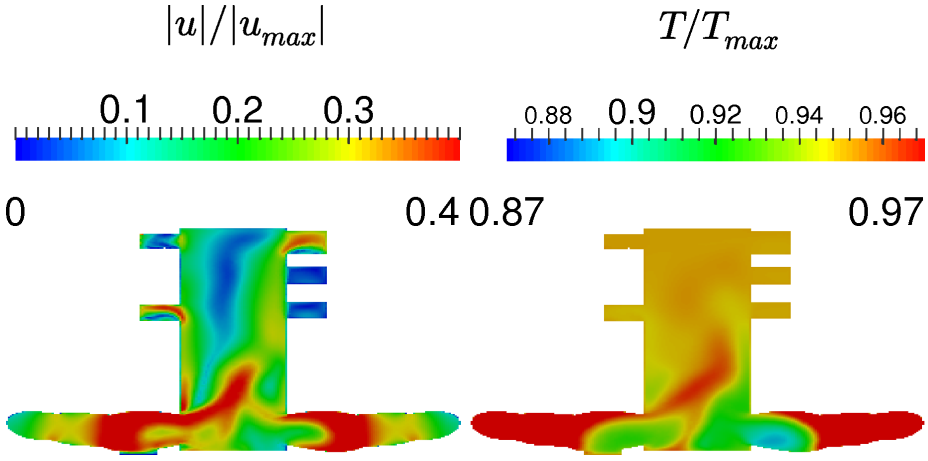

Fig. 7.11.: Normalized velocity magnitude (left) and temperature (right) in the mixing chamber.

Due to the warm air, guided via the recirculation units (Recirc1 and Recirc2) into the mixing chamber, buoyancy effects arise laterally for velocity and temperature (see Figure 7.11). Due to the cool air, guided via the pack units into basement of the chamber, a mixture of cool and warm air is present. The temperature of the air is at its lowest level at Pack2 ($\frac{T}{T_{max}} = 0.87$), therefore, the buoyancy effects are reduced at the related parts and the temperature is low, respectively (see Figure 7.11). The evaluation of the cost functional for the original design results in an initial value of $J_0 = 60\,274\,\frac{\mathrm{K^2\,kg}}{\mathrm{s}}$.
The adjoint equations (4.82)–(4.84) are subsequently solved. Hereafter, the solution of the primal and adjoint flow equations leads to the sensitivity (4.101) from which the gradient is computed by solution of the Laplace-Beltrami equation (4.138). Figure 7.12 displays the sensitivity and the gradient for the original design.

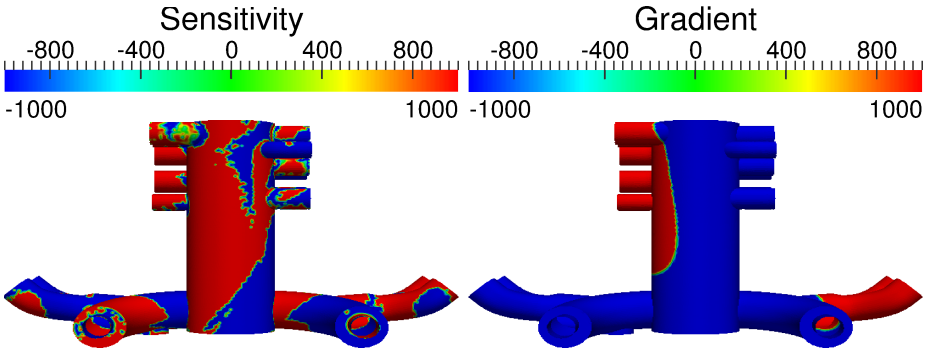

Fig. 7.12.: Sensitivity (left) and gradient (right) in the mixing chamber.

The sensitivity (Figure 7.12, left) shows a rough behavior with ragged contours while the gradient (Figure 7.12, right) behaves smoothly. A reason for the large differences between sensitivity and gradient is the influence of the mesh size $\Delta x \approx 1\,\mathrm{m}^{-2}$ on the solution of the Laplace-Beltrami equation. The considered example fortifies the necessity to compute the gradient for the shape modification. By combination of the gradient with a proper step size, the application of a gradient method, like steepest descent, leads to an improved design. The design boundary, Γ_{dsg}, enabled for the shape modification, is the whole mixing chamber wall. The surface is morphed according to the direction of the gradient, with a maximum deformation of $\Delta\beta = 0.01\,\mathrm{m}$. Negative values indicate a morphing in outward normal direction. In regions where the gradient is positive the mesh is slightly morphed inwards. At these regions the temperature is rather low for the original configuration (see Figure 7.11, right). Compacting these regions leads to a higher temperature level and, therefore, to an improvement of the cost functional. A further RANS simulation is performed to validate the degree of improvement. The new design results in a normalized value of $J/J_0 = 0.4161$ for the cost functional, equal to a relative improvement of 58 % compared to the initial design. The design cycle is performed four times. In Table 7.5 the values for the cost functional at the different outlets of the mixing chamber are summarized. Hereby, the cost functional values are normalized by the initial cost functional value.

Table 7.5.: Normalized values ($^{J}/_{J_0}$) of cost functional at the objective outlets and design cycles.

Design cycle	0	1	2	3	4
$^{J}/_{J_0}$ at TZ1	$5.35 \cdot 10^{-2}$	$0.04 \cdot 10^{-2}$	$0.38 \cdot 10^{-2}$	$0.15 \cdot 10^{-2}$	$0.16 \cdot 10^{-2}$
$^{J}/_{J_0}$ at TZ2	$3.86 \cdot 10^{-2}$	$0.01 \cdot 10^{-2}$	$0.03 \cdot 10^{-2}$	$0.07 \cdot 10^{-2}$	$0.003 \cdot 10^{-2}$
$^{J}/_{J_0}$ at TZ3	$6.56 \cdot 10^{-2}$	$0.17 \cdot 10^{-2}$	$0.11 \cdot 10^{-2}$	$0.02 \cdot 10^{-2}$	$0.07 \cdot 10^{-2}$
$^{J}/_{J_0}$ at TZ4	$11.84 \cdot 10^{-2}$	$0.81 \cdot 10^{-2}$	$0.21 \cdot 10^{-2}$	$0.04 \cdot 10^{-2}$	$0.01 \cdot 10^{-2}$
$^{J}/_{J_0}$ at TZ5	$0.05 \cdot 10^{-2}$	$0.60 \cdot 10^{-2}$	$0.01 \cdot 10^{-2}$	$0.02 \cdot 10^{-2}$	$0.02 \cdot 10^{-2}$
$^{J}/_{J_0}$ at TZ6	$0.75 \cdot 10^{-2}$	$0.03 \cdot 10^{-2}$	$0.05 \cdot 10^{-2}$	$0.19 \cdot 10^{-2}$	$0.26 \cdot 10^{-2}$
$^{J}/_{J_0}$ at E/E	$0.2 \cdot 10^{-2}$	$0.11 \cdot 10^{-2}$	$0.14 \cdot 10^{-2}$	$0.15 \cdot 10^{-2}$	$0.04 \cdot 10^{-2}$
$^{J}/_{J_0}$ at F/D	$1.84 \cdot 10^{-2}$	$0.30 \cdot 10^{-2}$	$0.08 \cdot 10^{-2}$	$0.09 \cdot 10^{-2}$	$0.07 \cdot 10^{-2}$
$^{J}/_{J_0}$ at FCRC	$44.16 \cdot 10^{-2}$	$33.61 \cdot 10^{-2}$	$35.08 \cdot 10^{-2}$	$31.24 \cdot 10^{-2}$	$29.08 \cdot 10^{-2}$
$^{J}/_{J_0}$ at CCRC	$12.24 \cdot 10^{-2}$	$0.27 \cdot 10^{-2}$	$0.63 \cdot 10^{-2}$	$0.02 \cdot 10^{-2}$	$0.03 \cdot 10^{-2}$
$^{J}/_{J_0}$ at Cargo	$13.15 \cdot 10^{-2}$	$5.66 \cdot 10^{-2}$	$1.44 \cdot 10^{-2}$	$0.79 \cdot 10^{-2}$	$0.60 \cdot 10^{-2}$
$\sum$	1	0.4161	0.3816	0.3278	0.30343
Improvement	0 %	58 %	62 %	67 %	70 %

The cost functional improves significantly from one design step to the other. The further design cycles lead to relative improvements of 58 %, 62 %, 67 % and 70 % compared to the initial design, for deformations of $\Delta\beta = 0.005\,\mathrm{m}$, $\Delta\beta = 0.003\,\mathrm{m}$ and $\Delta\beta = 0.002\,\mathrm{m}$, respectively. The critical point is the cost functional at the FCRC outlet, with a relative initial value of 0.44157, potentially offering the largest improvement. The highest amount of improvement for the sum over the exits is achieved after the first design cycle (58 %). Subsequent cycles lead to additional improvements of 4 %, 5 % and 3 %. Figure 7.13 illustrates the numerical results of the mass flow enhanced temperature difference at the outlets for sequential design cycles.

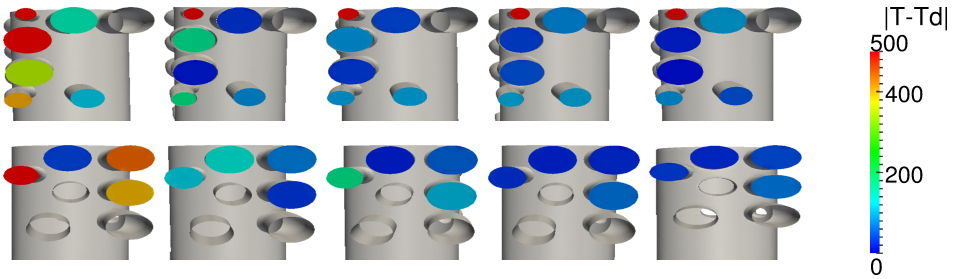

Fig. 7.13.: Difference to intermediate temperature at the lateral exits (top: right side, bottom: left side) for initial design and 1st, 2nd, 3rd, 4th design cycle (from left to right).

Figure 7.13 clearly illustrates the improvement of the cost functional from one design step to the other. While the difference to the desired temperature is large at several exits (Figure 7.13, left), the difference decreases in the course of the design modification.
As just demonstrated, the adjoint method delivers vast improvement for the considered application case and is therefore a preferable method for complex, temperature-related cases of this dimension.

7.3. Topology Optimization of Do728-KLA

The first application case for the topology optimization is the cabin air outlet of a Do728 aircraft. In contrast to Section 7.1, where the cabin air outlet has been endued with hole plates to homogenize the flow, the geometry contains 17 porous regions instead of hole plates, enabled for the porosity optimization. The aim is to compute an ideal porosity for each porous region, using two step size selection strategies. In Figure 7.14 the geometry of the Do728 cabin air outlet, equipped with porous regions, is illustrated.

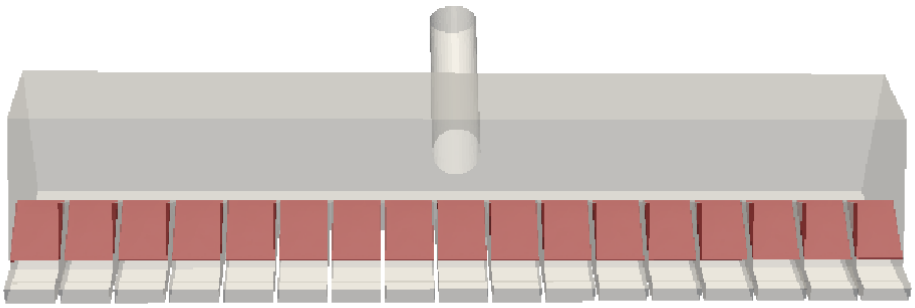

Fig. 7.14.: Cabin air outlet of Do728. Porous regions are marked in red.

Flows governed by the RANS equations with embedded Darcy term (4.116), (4.117) are studied. Here, $L^j \subset \Omega$ denote the 17 porous regions in the computational domain at which the embedded Darcy term reads $\alpha_{\mathcal{L}} = (\alpha^1, \cdots, \alpha^{17})^t \in \mathbb{R}^{17}$. An optimization problem is considered in which for given $\alpha_{\mathcal{L}} \in \mathbb{R}^{17}$ the RANS equations are fulfilled for u and p. As in the previous section the cost functional uniformity of the velocity at the outlet segments

(3.38) is examined. The desired velocity $\underline{u}_d$, computed from continuity arguments (inlet mass flux equals outlet mass flux) to $|\underline{u}_d| = 0.8916\,\frac{\mathrm{m}}{\mathrm{s}}$, is employed. The cost functional contributes to the adjoint boundary conditions (4.49), (4.50) yielding

$$\hat{p} = \rho u_n \hat{u}_n + \rho u_i \hat{u}_i + \mu_e \frac{\partial \hat{u}_n}{\partial n} + \left(u_n - |u_{i(d)}|\right) \qquad \text{on} \quad \Gamma_{out}, \tag{7.6}$$

$$0 = \rho \hat{u}_{i(t)} u_n + \mu_e \frac{\partial \hat{u}_{i(t)}}{\partial n} + u_{i(t)} \qquad \text{on} \quad \Gamma_{out}\,. \tag{7.7}$$

The control is the Darcy porosity term at the 17 porous plates for which an initial porosity value of $\alpha_0 = 200\,\frac{\mathrm{kg}}{\mathrm{m}^3\mathrm{s}}$ is set. The initial porosity involves the computation of the free area coefficient according to [35], by taking into account the thickness of the plate, the average velocity and assuming the same diameter of the orifices as for the geometry with perforated plates (see 7.1). In this way, the initial porosity corresponds to a hole plate with 80% covered by holes. At inlet and wall prescribed velocity and zero pressure gradient, at the outlet zero pressure and zero velocity gradient boundary conditions are employed. The flow enters the inlet with a bulk velocity of $u_B = 7\,\frac{\mathrm{m}}{\mathrm{s}}$. Based on the inlet bulk velocity, the diameter of the inlet ($l = 0.057\,\mathrm{m}$) and the kinematic viscosity of air, $\nu = 1.5 \cdot 10^{-5}\,\frac{\mathrm{m}^2}{\mathrm{s}}$, the Reynolds number is $Re = 27\,000$. Turbulence is modeled via the high-Re SST $k-\omega$ turbulence model (3.10)–(3.12). Steady state simulations, solving primal and adjoint incompressible RANS equations, are performed with *simpleFoam* and its adjoint analogue in OpenFOAM® on an unstructured mesh consisting of roughly two million tetrahedral cells until a fair level of convergence is reached (5 000 iterations, normalized initial residuals below 10^{-6}). The adjoint flow variables are computed by solving Equation (4.118) and (4.119) with appropriate boundary conditions (4.44)–(4.50) numerically. To obtain a reference solution, the porosity is assigned to the initial value. Figure 7.15 illustrates the velocity magnitude at the outlet and the related sensitivity at the porous zones.

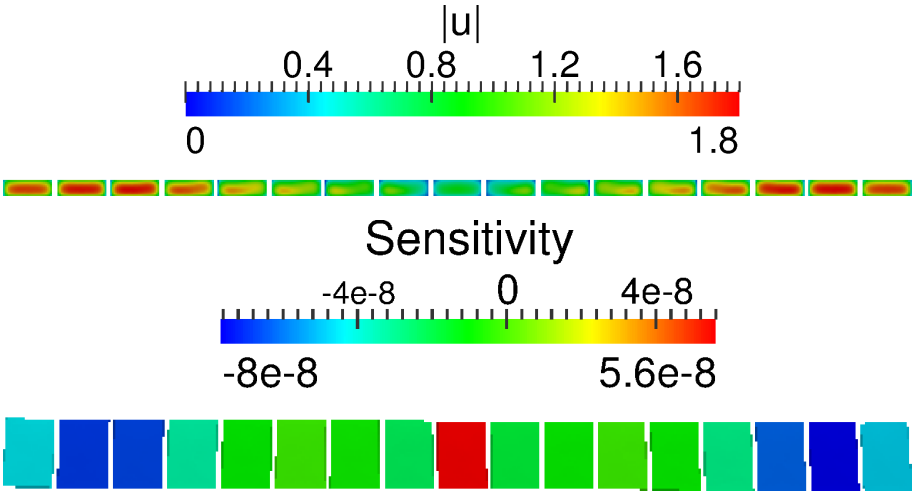

Fig. 7.15.: Velocity magnitude at outlet segments (top) and sensitivity at porous regions (bottom) for initial design of Do728-KLA.

Similar to the flow at the Do728-KLA with geometrically resolved hole plates (Section 7.1), the velocity magnitude is large at the lateral outlet segments and small at the centric components (Figure 7.15, top). Accordingly, the sensitivity induces to increase the porosity at the lateral porous zones (negative sensitivity values in Figure 7.15, bottom), while maximum positive sensitivity values at the centric porous zone (Figure 7.15, bottom) induce low porosity values at these parts. The proposition is reasonable as large porosity values decrease the velocity at the lateral outlet parts, leading to a homogenization of the outlet velocity. The initial cost functional value for the non-optimized porosity distribution is $J_0 = 0.00180856\,\frac{\mathrm{m}^4}{\mathrm{s}^2}$.
For the optimization the gradient descent is combined with two different step size selection strategies. Firstly, a constant step size, secondly, an Armijo step size selection strategy [18] for the gradient descent is employed. The maximal porosity value is $\alpha_{max} = 10\,000\,\frac{\mathrm{kg}}{\mathrm{m}^3\mathrm{s}}$, the minimal porosity value is $\alpha_{min} = 0\,\frac{\mathrm{kg}}{\mathrm{m}^3\mathrm{s}}$. The results for the constant step size and the step size computed from the Armijo rule are presented in the following subsections.

Constant Step Size

The topology optimization cycle (Algorithm 2) with a constant step size of $\lambda = 10^{10}$ and search direction $d = -\left(\frac{\partial L}{\partial \alpha_{\mathcal{L}}}\right)_{L^j} = -\sum_{P \in L^j} (u_i \hat{u}_i V)^{(P)}$ (4.122) is performed. The design for each porous zone is updated in a number of 200 design cycle loops. Starting from the porosity term $\alpha_0 = 200\,\frac{\mathrm{kg}}{\mathrm{m}^3\mathrm{s}}$ on all plates L^j, the final porosity distribution is as illustrated in Table 7.6 and Figure 7.16.

Table 7.6.: Porosity distribution after adjoint optimization with constant step size.

Plate number	D01	D02	D03	D04	D05	D06	D07	D08	D09
Porosity term in $\frac{\mathrm{kg}}{\mathrm{m}^3\mathrm{s}}$	7 907	8714	9 346	7 642	4 558	1 958	778	1 001	0
Plate number	D10	D11	D12	D13	D14	D15	D16	D17	
Porosity term in $\frac{\mathrm{kg}}{\mathrm{m}^3\mathrm{s}}$	982	747	1 908	4 693	7 676	9 354	9 026	8 123	

Low porosity values are present at the centric porous zones (D07-D11), large values at the lateral parts (D01-D04, D14-D17). The differences to the desired velocity at the outlet are displayed in Figure 7.17. While the velocity distribution is inhomogeneous for the initial design (Figure 7.17, top) with pronounced large differences to the desired velocity at the sides, the velocity distribution is more homogeneous for the new designed topology (Figure 7.17, bottom). The difference to the desired velocity decreases, particularly at lateral and centric outlet segments. After the design cycle, the relative cost functional value is $J/J_0 = 0.82$, yielding an improvement of approximately 18 %, relative to the initial value.

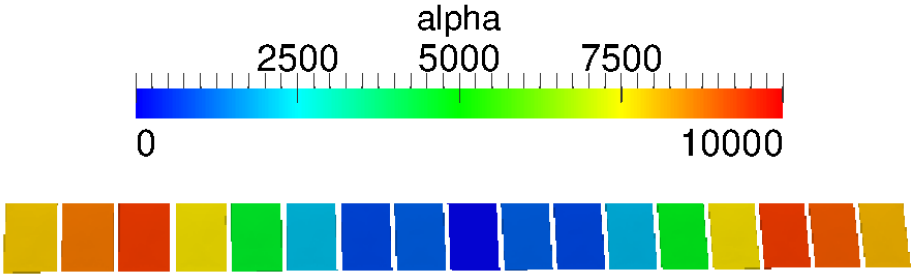

Fig. 7.16.: Porosity distribution on control regions.

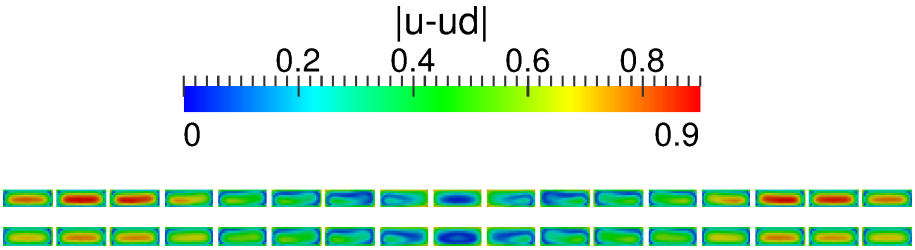

Fig. 7.17.: Difference to desired velocity $\underline{u}_d$ at outlet before (top) and after (bottom) the porosity optimization with constant step size.

Armijo Step Size

In this subsection an Armijo step length selection (2.45) rule is applied to the gradient descent in Algorithm 2 to improve the topology of the Do728 cabin air outlet.
The primal (4.116), (4.117) and adjoint (4.118), (4.119) RANS solutions, required for the sensitivity (4.122), are computed. The control is performed via modification of the porosity values on the 17 hole plates, using the Armijo step size strategy with $\sigma = 5 \cdot 10^{10}$, $\beta_* = 0.5$, $\gamma = 1 \cdot 10^{-4}$. A RANS-run for the porosity value of iteration step $k+1$, $\alpha_{\mathcal{L}}^k + \lambda d^k$ is necessary to determine $J(\alpha_{\mathcal{L}}^k + \lambda d^k)$ for evaluation of the Armijo condition (2.45), which is computationally expensive for complex systems. As a remedy, this value is evaluated on a coarse mesh (reduced Armijo approach, see Figure 2.1). To validate the quality of the reduced approach, the Armijo optimization strategy is also computed on a fine mesh. A number of 25 design updates is conducted. The Armijo condition (2.45) is fulfilled in each case after the first iteration, leading to $\lambda = 1$. The final porosity distributions for the full and the reduced Armijo approach are identical. The result is illustrated in Table 7.7 and Figure 7.18. Analogously to the result obtained with a constant step size, low porosity values are present at the centric (D07-D11), large values at the lateral porous zones (D01-D04, D14-D17). Therefore, the reduced approach with a coarser mesh yields the same result *and* reduces the cost of the Armijo rule evaluation in the step size selection. A cost functional reduction of 17% ($J/J_0 = 0.83$) is obtained from both Armijo techniques. The result of the difference to the desired velocity at the outlet is illustrated in Figure 7.19.

Table 7.7.: Porosity distribution after adjoint optimization with Armijo step size.

Plate number	D01	D02	D03	D04	D05	D06	D07	D08	D09
Porosity term in $\frac{kg}{m^3 s}$	8 485	10 000	10 000	7 534	3 938	610	74	411	0
Plate number	D10	D11	D12	D13	D14	D15	D16	D17	
Porosity term in $\frac{kg}{m^3 s}$	234	199	534	4 013	7 440	10 000	10 000	8 865	

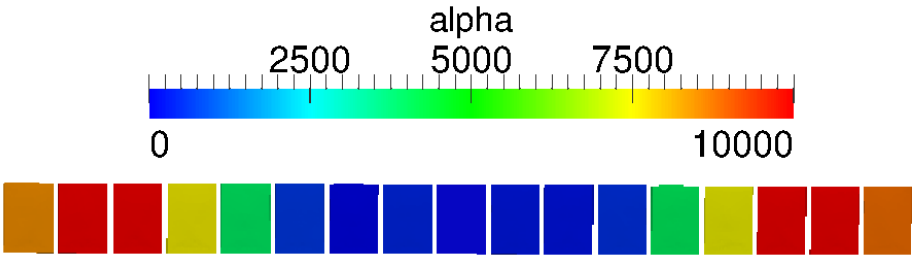

Fig. 7.18.: Porosity distribution on hole plates after topology optimization for Armijo step size strategy.

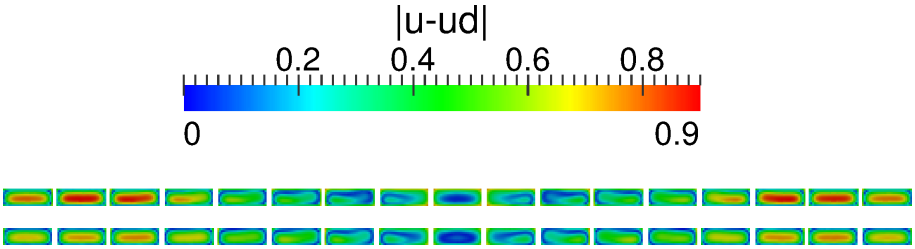

Fig. 7.19.: Difference to desired velocity at outlet before (top) and after (bottom) the Armijo porosity optimization.

Analogously to the computation with a constant step size, the velocity distribution is more homogeneous for the modified topology (Figure 7.19, bottom). The difference to the desired velocity decreases, particularly at the lateral and centric outlet segments. Compared to the usage of a constant step size (18 %), the improvement, yielded via the Armijo step size selection rule (17 %), is similar. Table 7.8 illustrates the comparison of the different step size selection strategies that are applied to the cabin air outlet, namely constant step size, full and reduced Armijo approach. The computational time reduces by a factor of 2.5 compared to the gradient descent with a constant step size and by a factor of three compared to the full Armijo approach (see Table 7.8).

Table 7.8.: Result for constant step size, full and reduced Armijo.

	Constant step size	Full Armijo	Reduced Armijo
Number of mesh cells	$4 \cdot 10^6$	$4 \cdot 10^6$	$7 \cdot 10^5$ & $4 \cdot 10^6$
Time per cost functional evaluation in seconds	-	100	15
Number of design updates	200	25	25
Improvement of cost functional	18 %	17 %	17 %
Computational time in hours	0.625	0.8	0.25

Concurrently, the reduced Armijo technique yields results similar to that achieved by means of different step size selection strategies (17 % for the reduced approach vs. 17 % for the full approach and 18% for the employment of a constant step size, see Table 7.8). Thus, the reduced Armijo strategy is very efficient in the considered application.
It has been shown that the reduced Armijo approach is an efficient technique to compute a suitable step size with simultaneously low computational costs, when compared to the full Armijo approach. Note that the quality of the reduced meshes is crucial to obtain trustworthy evaluations of the Armijo rule. Choosing the meshes too coarse causes unreliable predictions which may lead to incorrect step size selections.

7.4. Topology Optimization of Cockpit Air Outlet

The second application for the topology optimization is the air outlet of a cockpit, serving as validation case for the sparsity promoting regularization term. The air outlet consists of a pipe, through which the flow enters the upper part of the outlet. Subsequently, the flow is guided through a hole plate holding 185 holes, serving as porous control regions. After passing the hole plate, the flow enters the lower part of the air outlet before leaving the outlet. The plenum behind the air outlet is modeled by a box. The geometry without the box is illustrated in Figure 7.20.

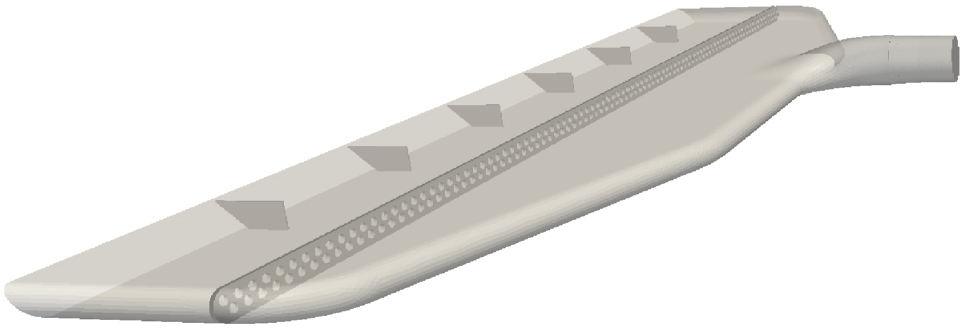

Fig. 7.20.: Geometry of cockpit air outlet.

For reasons of data protection, the geometry in Figure 7.20 is distorted. The governing equations are the primal (4.116), (4.117) and adjoint (4.118), (4.119) incompressible RANS equations with the modified Darcy porosity term defined on the 185 porous regions $L^j \subset \Omega$ as $\alpha_{\mathcal{L}} = (\alpha^1, \cdots, \alpha^{185})^t \in \mathbb{R}^{185}$. Typical boundary and initial conditions for ducted flows are employed. It is intended to improve the porosity distribution on the 185 holes contained in the hole plate. The governing cost functional is uniformity of the flow at the cut surface (3.38), located between air outlet and the plenum behind the air outlet with respect to a desired velocity $\underline{u}_d$, computed from the continuity equation, stating that the mass flux entering the domain is equal to the mass flux leaving the domain. A desired velocity of $\underline{u}_d = (0\ 0.5889\ 0.39)\ \frac{\mathrm{m}}{\mathrm{s}}$ is obtained. As the cost functional is not evaluated at the boundary outlet, but inside the flow domain, the boundary conditions reduce and additional cost functional derivatives arise in the volume equations (cf. Equation (4.7) and (4.9)). The adjoint volume equations (4.118), (4.119), are adapted as follows

$$-2\rho u_j \hat{S}_{ij} = \frac{\partial}{\partial x_j}\left(2\mu_e \hat{S}_{ij} - \hat{p}\delta_{ij}\right) - E(\alpha_{\mathcal{L}})\hat{u}_i - \frac{\partial j_\Omega}{\partial u_i}, \tag{7.8}$$

$$\frac{\partial \hat{u}_i}{\partial x_i} = 0\,, \tag{7.9}$$

where

$$\frac{\partial j_\Omega}{\partial u_i} = (u_i - u_{i(d)}) \quad \text{on} \quad \Omega_{dsg}\,, \tag{7.10}$$

and the boundary conditions (4.46)–(4.47) at the inlet reduce to

$$\hat{u} = 0\,, \tag{7.11}$$

and the outlet boundary conditions (4.49)–(4.50) reduce to

$$\hat{p} = \rho u_n \hat{u}_n + \rho u_i \hat{u}_i + \mu_e \frac{\partial \hat{u}_n}{\partial n}\,, \tag{7.12}$$

$$0 = \rho \hat{u}_{i(t)} u_n + \mu_e \frac{\partial \hat{u}_{i(t)}}{\partial n}\,. \tag{7.13}$$

The sensitivity is computed from the volume weighted average value over each hole (4.122). Note that the cost functional derivative in Equation (7.8) only appears on Ω_{obj}, i.e. the cut interface of the air outlet and the plenum. The steady state primal and adjoint RANS equations are solved by using *simpleFoam* and its adjoint analogue until a fair level of convergence is achieved. As before, the high-Re SST $k-\omega$ turbulence model (3.10)–(3.12) is used to model the turbulent flow ($Re = 31\,000$). Figure 7.21 displays the result for the velocity at the outlet and the related sensitivity at the porous zones before the optimization is performed.

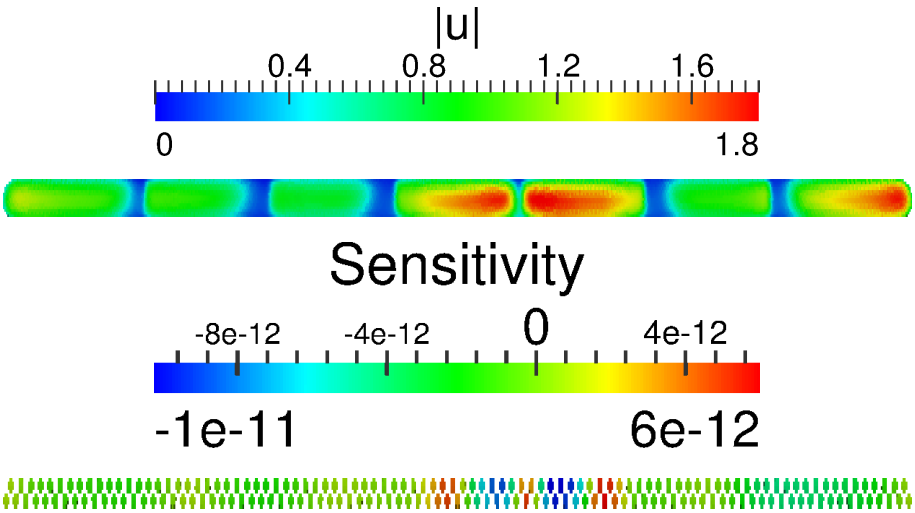

Fig. 7.21.: Velocity at the outlet before optimization.

The value of the cost functional is normalized by the volume of the cut interface, Ω_{obj}. For the initial topology ($\alpha_0 = 0\,\frac{\mathrm{kg}}{\mathrm{m^3 s}}$ at the porous regions L^j) the evaluation results in an initial cost functional value of $J_0 = 0.28849\,\frac{\mathrm{m^2}}{\mathrm{s^2}}$. The velocity magnitude is maximum at the centric and right part of the outlet (see Figure 7.21, top). Correspondingly, the sensitivity takes negative values at the related holes (see Figure 7.21, bottom). Negative sensitivity values on the holes induce an increase of the accounting porosity values; positive values induce a decrease, respectively. Increasing the porosity value lowers the accounting velocity as the hole is less permeable for the flow to pass. The sensitivity takes negative values with a large magnitude at regions where the velocity is high, and positive values at regions where the velocity is low. Thus, the proposition of the sensitivity is reasonable.
In the next step, the realization of the porosity modification induced by the sensitivity is conducted. The adjoint topology optimization in conjunction with a steepest descent approach is applied. In the topology optimization design cycle (Algorithm 2) the porosity is adapted by a gradient descent step, using the sensitivity and a constant step size of $\lambda = 10^{13}$ and search direction $d = -\left(\frac{\partial L}{\partial \alpha_{\mathcal{L}}}\right)_{L^j} = -\sum_{P \in L^j} (\hat{u}_i u_i V)^{(P)}$. A maximum porosity value of $\alpha_{max} = 10^6\,\frac{\mathrm{kg}}{\mathrm{m^3 s}}$ models a closed hole. Algorithm 2 is repeated until the porosity changes converge and the cost functional does not decrease any more. Figure 7.22 shows the cost functional progress. The reason for the fluctuating cost functional value in Figure 7.22 is the stepwise adaptation of the velocity value to the change of porosity. After the porosity value is converged, the fluctuation reduces. The relative cost functional value is decreased to $J/J_0 = 0.54$ for the modified topology. Hence, the cost functional improves significantly by 46 %, relative to the initial value. The porosity distribution is illustrated in Figure 7.23. Large porosity values are apparent in parts where the velocity magnitude is large for the initial design. Figure 7.24 and Figure 7.25 illustrate the distribution of the velocity and the cost functional value at the cut surface for the original and improved topology.

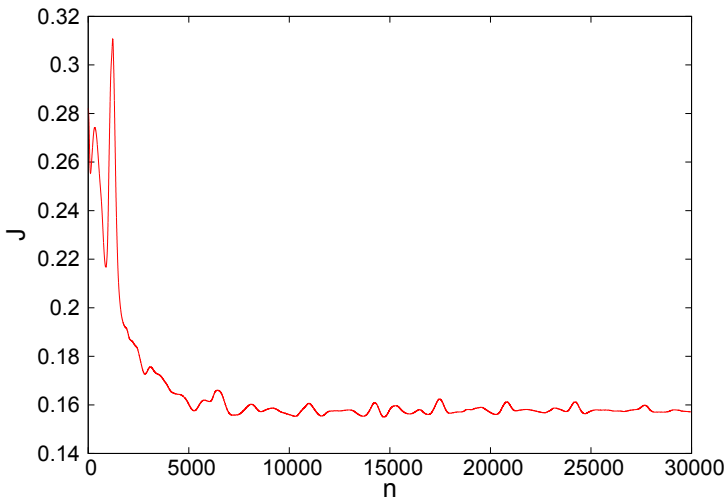

Fig. 7.22.: Cost functional value development during the design cycle.

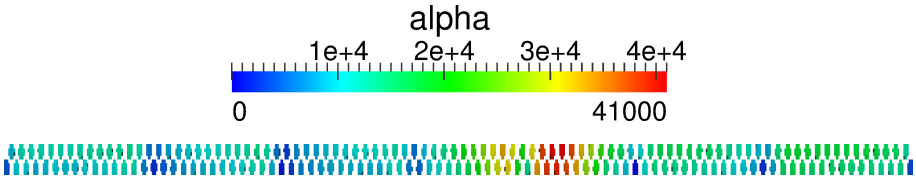

Fig. 7.23.: Porosity distribution on holes after topology optimization.

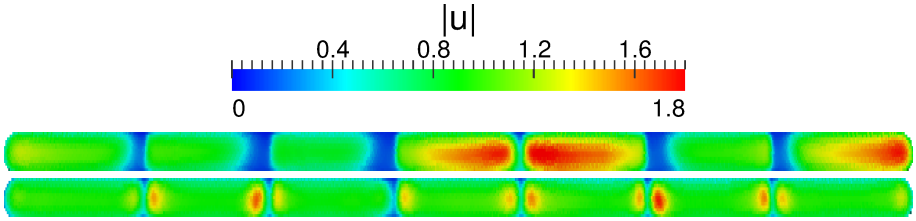

Fig. 7.24.: Velocity magnitude at Ω_{obj} before (top) and after (bottom) the optimization.

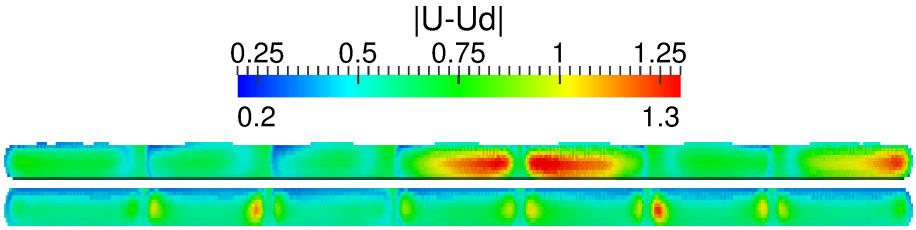

Fig. 7.25.: Difference to $\underline{u}_d$ at Ω_{obj} before (top) and after (bottom) the optimization.

Figure 7.24 and Figure 7.25 clearly display the improved cost functional for the modified topology. While the velocity magnitude is large at several parts of the outlet for the initial design (Figure 7.24, top), with a large distance to the desired velocity (Figure 7.25, top), it is much more homogeneous for the optimized topology (Figure 7.24, bottom) with only few spots where large velocity values are present. Correspondingly, the difference to the desired velocity improves significantly along the outlet for the modified topology (see Figure 7.25, bottom).
In the next step the L^1-regularization (4.124), introduced in Section 4.4, is added to the cost functional to penalize the amount of control. A value for ϵ, the weighting factor for the regularization term (4.124), is estimated. It is aimed to scale the regularization term such that it has the same order of magnitude as the cost functional. The maximal value for the cost functional uniformity of velocity is computed at the outlet from primal simulation data. It takes its maximum at $\frac{1}{2}(u - \underline{u}_d)^2 = 0.92\,\frac{\mathrm{m}^2}{\mathrm{s}^2}$. The regularization term is maximal for $\alpha = \alpha_{max}$. Thus, the weighting factor is computed as

$$\epsilon = \frac{\int_{\Omega_{obj}} 0.92 d\Omega}{\int_{\Omega_{dsg}} \alpha_{max} d\Omega} = 7 \cdot 10^{-6}\,, \tag{7.14}$$

with $V^{(\Omega_{obj})} = 2.43 \cdot 10^{-5}\,\mathrm{m}^3$ and $V^{(\Omega_{dsg})} = 3.15 \cdot 10^{-6}\,\mathrm{m}^3$. The parameter μ marks the accuracy and is chosen to be $\mu = 0$, such that the approximated Huber term is equal to the L^1-norm. In [19] it is shown that the results obtained by using the Huber approximation are similar. The optimization is performed for $\epsilon = 10^{-6}$ and $\epsilon = 10^{-5}$ with a step size of $\lambda = 10^{13}$, and $\epsilon = 5 \cdot 10^{-4}$ with a step size of $\lambda = 10^{14}$. The step size is increased for a larger ϵ, as a large regularization term weakens the sensitivity and a larger step size accelerates the optimization. Figure 7.26 shows the porosity distribution for different values of ϵ and Figure 7.27 the related difference to the desired velocity at the outlet.

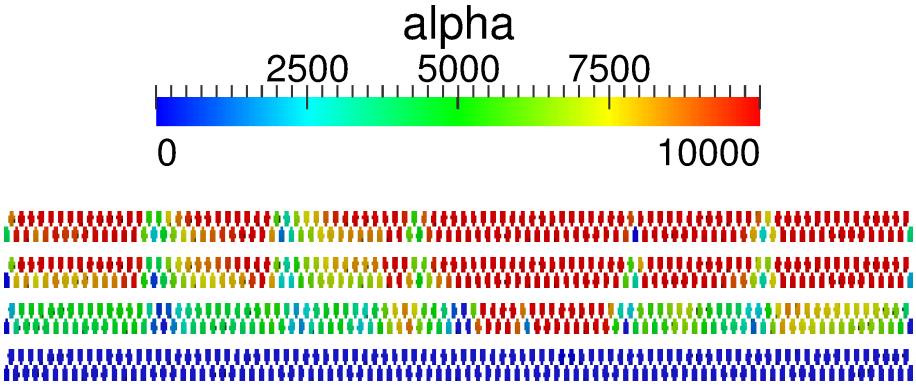

Fig. 7.26.: Porosity distribution for $\epsilon = 0$, $\epsilon = 10^{-6}$, $\epsilon = 10^{-5}$ and $\epsilon = 5 \cdot 10^{-4}$ (from top to bottom).

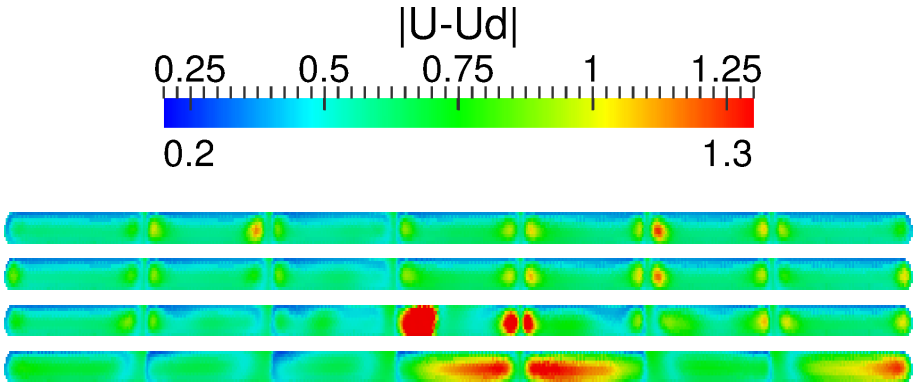

Fig. 7.27.: Difference to desired velocity for $\epsilon = 0$, $\epsilon = 10^{-6}$, $\epsilon = 10^{-5}$ and $\epsilon = 5 \cdot 10^{-4}$ (from top to bottom).

With increasing weighting factor ϵ the distribution becomes sparser (see Figure 7.26). For $\epsilon = 5 \cdot 10^{-4}$ almost no porosity is present. For a small value of $\epsilon = 10^{-6}$ the porosity distribution and corresponding distance to the desired velocity is similar to $\epsilon = 0$ (see Figure 7.26 and 7.27), leading to big portions of the holes with large porosity values and, concurrently, to significant improvements concerning the distance to the desired velocity. For $\epsilon = 10^{-5}$, the amount of porosity has decreased (Figure 7.26), still, a significant improvement of the velocity distance is present (Figure 7.27). In Table 7.9 the results are sketched for different values of ϵ.

Table 7.9.: Optimization with various parameters.

Initial design	$0.28849 \frac{\mathrm{m}^2}{\mathrm{s}^2}$		
	Relative cost functional value J/J_0	Improvement	α_{mean} in $\frac{\mathrm{kg}}{\mathrm{m}^3\mathrm{s}}$
$\epsilon = 0$	0.54	46 %	56.75
$\epsilon = 1 \cdot 10^{-6}$	0.55	45 %	48.21
$\epsilon = 1 \cdot 10^{-5}$	0.74	26 %	24.10
$\epsilon = 5 \cdot 10{-}4$	0.9992	<0.1 %	0.0039

Analogously to the visual interpretation of Figure 7.26 and 7.27, the amount of porosity reduces with rising regularization weighting factor. For $\epsilon = 10^{-6}$ the results only slightly distinguish from $\epsilon = 0$. For $\epsilon = 10^{-5}$, the amount of porosity is halved (from $\alpha_{mean} = 48 \frac{\mathrm{kg}}{\mathrm{m}^3\mathrm{s}}$ for $\epsilon = 10^{-6}$ to $\alpha_{mean} = 24 \frac{\mathrm{kg}}{\mathrm{m}^3\mathrm{s}}$ for $\epsilon = 10^{-5}$), while the improvement reduces by less than a factor of two (from 45 % for $\epsilon = 10^{-6}$ to 26 % for $\epsilon = 10^{-5}$). For the largest weighting

factor $\epsilon = 5 \cdot 10^{-4}$ neither a significant amount of porosity ($\alpha_{mean} = 0.0039 \frac{\text{kg}}{\text{m}^3\text{s}}$), nor a significant improvement is present ($< 0.1\,\%$).
As the results demonstrate, the choice of the weighting factor ϵ is crucial. A large weighting factor (here $\epsilon = 5 \cdot 10^{-4}$) leads to a significant decrease of the amount of control, whereas a small factor (here $\epsilon = 10^{-6}$) has almost no influence. Finding an ϵ which, on the one hand, supports the sparsity and, on the other hand, improves the cost functional by insertion of control at high impact regions, is a balancing act. In the considered case $\epsilon = 10^{-5}$ serves this purpose.
However, for the considered application, the determination of high impact regions is restricted. Increasing the regularization leads to a decrease of the degree of improvement in almost the same intensity as the amount of control. Furthermore, a digital distribution is not achieved by utilization of this approach. The regularization helps to reduce the amount of control but does in general not impede the the appearance of intermediate control values. For this goal, different approaches should be studied.

8. Conclusion and Outlook

The goal of this thesis was to investigate the applicability of adjoint methods to heating, ventilation and air-conditioning components. Are adjoint methods able to enhance the efficiency of HVAC components and to improve the comfort of aircraft cabins? The challenge consisted in combining mathematical correctness with a robust application to industrial reality and to adapt the adjoint method to the demands. Accordingly, suitable approaches have been derived, implemented, validated and applied to HVAC components

The adaptation of primal and adjoint Navier-Stokes-Fourier equations to the optimization of HVAC components applied to the derivation and implementation of appropriate cost functionals and associated boundary conditions. Verification of the sensitivity by comparison to finite differences showed a reasonable agreement. The gradient, the necessary means for the design update, has been computed by solution of the Laplace Beltrami equation. A verification study showed that the numerical solution of the Laplace Beltrami equation agrees with the exact solution for an analytic test case. The application to industrial HVAC components showed the improved properties of the gradient compared to the sensitivity, providing supplementary reasons for its usage. The investigation of specific problems was related to the efficient applicability of the adjoint method, concerning the step size computation and the adjustment to the demands for the optimization of HVAC components. In particular, an efficient method for the step size computation has been derived and implemented. The evaluation of the Armijo rule on a coarse mesh level led to a notable saving in computational effort. A mesh study showed that a coarsening up to the factor six still delivers reliable results. Concerning the demands arising from feasibility, several approaches have been derived and validated. A sparse distributed control, often preferred for the final topology, has been promoted by the insertion of an L^1-regularization term into the cost functional. As the L^1-regularization is not differentiable, the term has been optionally approximated by smooth Huber functions. Simple test cases served as validation for the approach. The improvement of the cost functional remained almost the same, although the amount of control was notably reduced. Another demand, that arose from reasons of feasibility, was the requirement of constant porosity values within one porous zone. For this purpose, the control space was reduced to the countable set of porous zones, leading to a modified sensitivity.

The focal point of this thesis was the transfer of mathematical concepts into the industrial practice, being on the interface between mathematics and engineering, combining theory and application. The developed adjoint framework has been applied to the HVAC components of aircrafts (mixing chamber, cabin air outlets), yielding notable improvements in few design updates. Thus, real world problems arising from industry with realistic physical conditions are possibly able to be considered by the presented adjoint approach. Conse-

quently, the earlier formulated question can be affirmed. It succeeded to adapt the adjoint theory such that the cabin comfort and efficiency of aircraft components can be enhanced therewith.
However, there is also space for improvement and expansion. Variations of turbulence properties, arising in the computation of the turbulent eddy viscosity, were neglected in the presented framework, thus, treated as frozen. To complete the variational approach, all physical properties should be varied, such as, for example, performed in [88]. Furthermore, in this thesis only steady state equations were considered. However, many physical properties are time-dependent. For this purpose, the derivation of the adjoint non-stationary equations is an option, as done, for example, in [12]. On the other hand, this approach leads to an enormous computational effort and is memory-intensive. Strategies like checkpointing are then required [24]. The application of suitable discretization schemes guarantee the duality between primal and continuous adjoint equations. In this thesis, neglecting the advection term, which is highly unstable, was performed for stability reasons. To perform the adjoint mode in a correct manner, the advection term should yet be included and discretized in the hybrid-adjoint manner [80]. By application of wall functions, different equations are used at the boundary. To obtain corresponding dual adjoint equations, an adjoint wall function should be derived by variation of the accounting equations at the wall. Concurrently, this approach leads to a high-Re sensitivity. Approaches for an adjoint logarithmic law of the wall and an extended thermal adjoint law of the wall exist, for example in [78], [28], [50]. Furthermore, to guarantee a uniform mesh quality after conducting the shape modification, strategies to preserve the mesh quality should be applied, such as in [46] or [77]. For an even more efficient optimization, the second derivative could be used for a Newton method. Approaches to compute the second derivative cheaply from the adjoint sensitivity are under consideration. A unification and automation of the process chain, consisting of solving primal and adjoint equations, computation of sensitivity and gradient and mesh-morphing for the shape optimization will increase user-friendliness and decrease error-proneness. Integration of the mesh-morphing into the solution software will enable one-shot shape updates, such as those performed in [62]. Consisting approaches to integrate the mesh-morphing into the OpenFOAM® framework apply, for example, to radial basis functions [37]. An open question is how one can realize a digital control distribution. The insertion of the L^1-regularization term reduces the amount of control but does not provide digitality, meaning the control variable to assume either minimum or maximum values. This feature is preferred in the topology optimization framework as a digital distribution is related to either solid or fluid structures which is properly realizable. Consideration of integer optimization approaches [54], penalty functions [5] or different norms for the regularization, such as total variation (TV) norm which is essentially the L^1 norm of the gradient and which is used for noise removal in image restoration [69] are worth considering in future research.

A. Functional Analysis

Norm, Banach Space

Let X be a real vector space. A mapping $||\cdot|| : X \to [0, \infty)$ is a *norm* on X, if

- $||\phi|| = 0 \Leftrightarrow \phi = 0$,
- $||c \cdot \phi|| = |c| \cdot ||\phi|| \;\; \forall \phi \in X, c \in \mathbb{R}$,
- $||\phi + \varphi|| \leq ||\phi|| + ||\varphi|| \;\; \forall \phi, \varphi \in X$.

A normed, real vector space X is called *Banach space*, if it is complete, i.e. if any Cauchy sequence (ϕ_n) has a limit $\phi \in X$ [33].

Linear Operators

Let X, Y be normed, real vector spaces with norms $||\cdot||_X$, $||\cdot||_Y$.
A mapping $M : X \to Y$ is called *linear operator*, if it satisfies

$$M(b\phi + c\varphi) = bM\phi + cM\varphi \;\forall \phi, \varphi \in X, \;\; b, c \in \mathbb{R}.$$

By $\mathcal{L}(X, Y)$ one denotes the space of all linear operators $M : X \to Y$ that are bounded, in the sense that

$$||M||_{X,Y} := \sup_{||\phi||_X = 1} ||M\phi||_Y < \infty \, .$$

Dual Space

Let X be a Banach space. The space $X^* := \mathcal{L}(X, Y)$ of bounded, linear operators on X is called *dual space* of X and is a Banach space with the operator norm. For $\phi^* \in X^*$, $\phi \in X$ it is written $< \phi^*, \phi >_{X^*,X} := \phi^*(\phi)$. $< \cdot, \cdot >_{X^*,X}$ is called *dual pairing* of X^* and X.

Dual Operator

Let X, Y be Banach spaces. Then, for an operator $M \in \mathcal{L}(X,Y)$, the *dual operator* $M^* \in \mathcal{L}(Y^*, X^*)$ is defined by its property

$$< M^*\phi, \varphi >_{X^*,X} = < \phi, M\varphi >_{Y^*,Y} \quad \forall \phi \in Y^*, \varphi \in X\,.$$

Inner product, Hilbert Space

Let X be a real vector space. A mapping $(\cdot,\cdot) : X \times X \to \mathbb{R}$ is called *inner product* on X, if

- For every $\phi \in X$ the mapping $\varphi \in X \to (\varphi, \phi)$ is linear,
- $(\phi, \varphi)_X = (\varphi, \phi)_X \ \forall \phi\,, \varphi \in X\,,$
- $(\phi, \phi)_X \geq 0 \ \forall \phi \in X\,,$
- $(\phi, \phi)_X = 0 \Leftrightarrow \phi = 0\,.$

The norm is defined as $||\cdot||_X = \sqrt{(\cdot,\cdot)_X}$. If X is a Banach space with inner product $(\cdot,\cdot)$ and induced norm $||\cdot||_X$, then it is called *Hilbert space*.

Directional Derivative

Let $J : U \subset X \to Y$ be an operator with Banach spaces X, Y and $U \neq \emptyset$ open.
J is called *directionally differentiable* at $\phi \in U$, if the limit

$$dJ(\phi, \varphi) := \lim_{t \to 0^+} \frac{J(\phi + t\varphi) - J(\phi)}{t} \in Y$$

exists for all $\varphi \in X$. In this case, $dJ(\phi, \varphi)$ is called *directional derivative* of J in the direction φ.

Fréchet Differentiable

Let $J : U \subset X \to Y$ be an operator with Banach spaces X, Y and $U \neq \emptyset$ open. A function J is called *Fréchet differentiable* at $\phi \in U$, if J directionally differentiable at ϕ and if the directional derivative

$$J'(\phi) : X \ni \varphi \to dJ(\phi, \varphi) \in Y$$

is bounded and linear, i.e. $J'(\phi) \in \mathcal{L}(X,Y)$ and if the following approximation holds

$$||J(\phi + \varphi) - J(\phi) - J'(\phi)\varphi||_Y = \mathcal{O}(||\varphi||_X) \ \text{ for } \ ||\varphi||_X \longrightarrow 0\,.$$

If $J : X \times Y \to Z$ is Fréchet differentiable at (φ, ϕ), then $J(\cdot, \phi)$ and $J(\varphi, \cdot)$ are Fréchet differentiable at φ and ϕ, respectively. These derivatives are called partial derivatives and denoted by $J_\varphi(\varphi, \phi)$ and $J_\phi(\varphi, \phi)$, respectively.

Riesz Representation Theorem

Let X be a Hilbert space. Then, for any $\phi^* \in X^*$, there exists a unique element $\varphi \in X$, such that

$$< \phi^*, \phi >_{X^*,X} = (\varphi, \phi)_X \ \forall \phi \in X$$

and

$$||\phi^*||_{X^*} = ||\varphi||_X$$

hold. $\varphi \in X$ is called the *Riesz representative* of $\phi^* \in X^*$. With this theorem, X can be identified with its dual space X^*

$$\begin{aligned} \mathfrak{R} : X^* &\to X \\ \phi^* &\to \mathfrak{R}(\phi^*) := \varphi. \end{aligned}$$

And the mapping $\mathfrak{R}$ is an isomorphism, which is called *Riesz isomorphism.*

Lebesgue Spaces

The *Lebesgue space* is defined as

$$L^p(\Omega) = \{\phi : \Omega \to \mathbb{R} \text{ Lebesgue measurable} : \ ||\phi||_{L^p(\Omega)} < \infty\}.$$

The norm $||\phi||_{L^p(\Omega)}$ is defined as

$$||\phi||_{L^p(\Omega)} := \left(\int_\Omega |\phi(x)|^p \, d\Omega \right)^{\frac{1}{p}}.$$

Finally, a subset of $L^p(\Omega)$ is defined,

$$\mathcal{L}^p_{loc}(\Omega) := \{\phi : \Omega \to \mathbb{R} \text{ Lebesgue measurable} : \ \phi \in \mathcal{L}^p(\Omega_c) \ \forall \Omega_c \subset \Omega \text{ compact}\}.$$

For the definition of *Lebesgue measurable*, please refer to [32].

Multiindex

For a *multiindex* $c = (c_1, \cdots, c_n) \in \mathbb{N}_0^n$, the order is defined by $|c| = \sum_i c_i$ and the c-th partial derivative at x is associated with

$$D^c\phi(x) := \frac{\partial^{|c|}\phi}{\partial {x_1}^{c_1} \cdots \partial {x_n}^{c_n}} .$$

Weak Derivatives

For a k-times continuously differentiable function $\phi \in \mathcal{C}^k(\overline{\Omega})$ and any multiindex $c \in \mathbb{N}_0^n$, $|c| \leq k$, holds the identity (due to $|c|$-times integration by parts)

$$\int_\Omega D^c\phi\varphi \, d\Omega = (-1)^{|c|} \int_\Omega \phi D^c\varphi \, d\Omega \; \forall\varphi \in C_c^\infty(\Omega) .$$

If there exists a function $\psi \in L^1_{loc}(\Omega)$ for $\phi \in L^1_{loc}(\Omega)$, such that

$$\int_\Omega \psi\varphi \, d\Omega = (-1)^{|c|} \int_\Omega \phi D^c\varphi \, d\Omega \; \forall\varphi \in C_c^\infty(\Omega) ,$$

then $D^c\phi := \psi$ is called the *c-th weak partial derivative* of ϕ. Here, the function space $C_c^\infty(\Omega)$ denotes the set of smooth functions $C^\infty(\overline{\Omega})$, which have a compact support

$$C_c^\infty := \{\phi \in C^\infty(\overline{\Omega}) : \mathrm{supp}(\phi) \subset \Omega \text{ compact}\}.$$

Sobolev Space

Let $\Omega \subset \mathbb{R}^n$ be open. The *Sobolev space* $H^1(\Omega)$ is defined by

$$H^1(\Omega) := \{\phi \in L^2(\Omega) : \phi \text{ has weak derivative } D^1\phi \in L^2(\Omega) \} ,$$

equipped with the norm

$$||\phi||_{H^1(\Omega)} := \left(\sum_{|c|\leq 1} ||D^c\phi||^2_{L^2} \right)^{\frac{1}{2}} .$$

The scalar product is, accordingly,

$$(\phi, \varphi)_{H^1(\Omega)} = \sum_{|c|\leq 1} ||D^c\phi||_{L^2} \; ||D^c\varphi||_{L^2} = \int_\Omega \phi\varphi \, d\Omega + \int_\Omega \nabla\phi\nabla\varphi \, d\Omega .$$

$H^1(\Omega)$ is a subspace of functions $\phi \in L^2(\Omega)$, for which the first weak derivative $D^1\phi$ is in $L^2(\Omega)$. If the function space is defined on Γ instead of Ω, one obtains, accordingly,

$$H^1(\Gamma) := \{\phi \in L^2(\Gamma) : \phi \text{ has weak a derivative } D^1\phi \in L^2(\Gamma)\}\,,$$

equipped with the norm

$$||\phi||_{H^1(\Gamma)} := \left(\sum_{|c|\leq 1} ||D^c\phi||^2_{L^2}\right)^{\frac{1}{2}}\,,$$

and scalar product

$$\begin{aligned}(\phi,\varphi)_{H^1(\Gamma)} &= \sum_{|c|\leq 1} ||D^c\phi||^2_{L^2}\,||D^c\varphi||^2_{L^2} \\ &= \int_\Gamma \phi\varphi\, d\Gamma + \int_\Gamma \nabla\phi\nabla\varphi\, d\Gamma = \int_\Gamma \phi\varphi\, d\Gamma + \int_\Gamma \nabla_\Gamma\phi\nabla_\Gamma\varphi\, d\Gamma\,, \qquad \text{(A.1)}\end{aligned}$$

where ∇_Γ denotes the tangential gradient

$$\nabla_\Gamma\phi = \nabla\phi - (\nabla\phi\cdot n)n\,.$$

Equation (A.1) holds, as the normal component of the gradient vanishes.

B. Integration by Parts

B.1. Adjoint RANS Equations

For the convective part in Equation (4.4), the product rule and the continuity equation (3.9) lead to

$$\begin{aligned}\int_\Omega \hat{u}_i \rho \delta \frac{\partial u_i u_j}{\partial x_j} d\Omega &= \int_\Omega \left[\hat{u}_i \rho \delta \left(u_i \frac{\partial u_j}{\partial x_j} \right) + \hat{u}_i \rho \delta \left(\frac{\partial u_i}{\partial x_j} u_j \right) \right] d\Omega \\ &= \int_\Omega \left[\hat{u}_i \rho \frac{\partial \delta u_i}{\partial x_j} u_j + \hat{u}_i \rho \frac{\partial u_i}{\partial x_j} \delta u_j \right] d\Omega \,,\end{aligned} \tag{B.1}$$

and, by using integration by parts, the integrands on the right-hand side of Equation (B.1) transform to

$$\begin{aligned}\int_\Omega \hat{u}_i \rho \frac{\partial \delta u_i}{\partial x_j} u_j d\Omega &= \oint_\Gamma \hat{u}_i \rho \delta u_i u_j n_j d\Gamma - \int_\Omega \rho \delta u_i \frac{\partial \hat{u}_i u_j}{\partial x_j} d\Omega \\ &= \oint_\Gamma \hat{u}_i \rho \delta u_i u_j n_j d\Gamma - \int_\Omega \rho \delta u_i \frac{\partial \hat{u}_i}{\partial x_j} u_j d\Omega - \underbrace{\int_\Omega \rho \delta u_i \hat{u}_i \frac{\partial u_j}{\partial x_j} d\Omega}_{=0} \,,\end{aligned} \tag{B.2}$$

$$\begin{aligned}\int_\Omega \hat{u}_i \rho \frac{\partial u_i}{\partial x_j} \delta u_j d\Omega &= \oint_\Gamma \hat{u}_i \rho u_i \delta u_j n_j d\Gamma - \int_\Omega \rho u_i \frac{\partial \hat{u}_i \delta u_j}{\partial x_j} d\Omega \\ &= \oint_\Gamma \hat{u}_i \rho u_i \delta u_j n_j d\Gamma - \int_\Omega \rho u_i \frac{\partial \hat{u}_i}{\partial x_j} \delta u_j d\Omega - \underbrace{\int_\Omega \rho u_i \hat{u}_i \frac{\partial \delta u_j}{\partial x_j} d\Omega}_{=0} \,,\end{aligned} \tag{B.3}$$

due to the continuity equation, also satisfied for the local variation of the velocity, i.e. $\frac{\partial \delta u_j}{\partial x_j} = 0$. Therefore, for the volume integrals of Equation (B.2) and (B.3) one obtains

$$-\int_\Omega \rho \delta u_i \frac{\partial \hat{u}_i}{\partial x_j} u_j d\Omega - \int_\Omega \rho u_i \frac{\partial \hat{u}_i}{\partial x_j} \delta u_j d\Omega = \int_\Omega -2 \rho u_j \hat{S}_{ij} \delta u_i d\Omega \,. \tag{B.4}$$

Here, $\hat{S_{ij}}$ denotes the adjoint complement to the symmetric rate-of-strain tensor, S_{ij}.
For the pressure term of Equation (4.4) holds

$$\int_\Omega \hat{u}_i \frac{\partial}{\partial x_j} \left(\delta_{ij} \delta p \right) d\Omega = \oint_\Gamma \hat{u}_i \delta p n_i d\Gamma - \int_\Omega \frac{\partial \hat{u}_i}{\partial x_i} \delta p \, d\Omega \,. \tag{B.5}$$

For the viscous term in Equation (4.4) it holds

$$\begin{aligned}&\int_\Omega -\hat{u}_i \frac{\partial}{\partial x_j}\mu_e \left(\frac{\partial \delta u_i}{\partial x_j}+\frac{\partial \delta u_j}{\partial x_i}\right) d\Omega \\ &= \oint_\Gamma -\hat{u}_i \mu_e \left(\frac{\partial \delta u_i}{\partial x_j}+\frac{\partial \delta u_j}{\partial x_i}\right) n_j d\Gamma + \int_\Omega \frac{\partial \hat{u}_i}{\partial x_j}\mu_e \left(\frac{\partial \delta u_i}{\partial x_j}+\frac{\partial \delta u_j}{\partial x_i}\right) d\Omega\,.\end{aligned} \tag{B.6}$$

For this term, the frozen turbulence approach has been used, i.e. $\delta\mu_e = 0$. Again, the second integral of Equation (B.6) is transformed via integration by parts, such that it follows

$$\begin{aligned}&\int_\Omega \frac{\partial \hat{u}_i}{\partial x_j}\mu_e \left(\frac{\partial \delta u_i}{\partial x_j}+\frac{\partial \delta u_j}{\partial x_i}\right) d\Omega \\ &= \int_\Omega \frac{\partial \hat{u}_i}{\partial x_j}\mu_e \frac{\partial \delta u_i}{\partial x_j} d\Omega + \int_\Omega \frac{\partial \hat{u}_i}{\partial x_j}\mu_e \frac{\partial \delta u_j}{\partial x_i} d\Omega \\ &= \oint_\Gamma \frac{\partial \hat{u}_i}{\partial x_j}\mu_e \delta u_i n_j d\Gamma - \int_\Omega \frac{\partial}{\partial x_j}\left(\frac{\partial \hat{u}_i}{\partial x_j}\mu_e\right)\delta u_i d\Omega \\ &+ \oint_\Gamma \frac{\partial \hat{u}_i}{\partial x_j}\mu_e \delta u_j n_i d\Gamma - \int_\Omega \frac{\partial}{\partial x_i}\left(\frac{\partial \hat{u}_i}{\partial x_j}\mu_e\right)\delta u_j d\Omega \\ &= \oint_\Gamma 2\mu_e \delta u_i \hat{S_{ij}} n_j d\Gamma - \int_\Omega \frac{\partial}{\partial x_j}\left(2\mu_e \hat{S}_{ij}\right)\delta u_i d\Omega\,.\end{aligned} \tag{B.7}$$

For the continuity equation in Equation (4.4) it holds

$$\int_\Omega -\hat{p}\frac{\partial \delta u_i}{\partial x_i} d\Omega = \oint_\Gamma -\hat{p}\delta u_i n_i d\Gamma + \int_\Omega \frac{\partial \hat{p}}{\partial x_i}\delta u_i d\Omega\,. \tag{B.8}$$

For the local variation of the cost functional in Equation (4.4) it follows

$$\delta_u J = \int_\Omega \delta_u j_\Omega d\Omega + \int_\Gamma \delta_u j_\Gamma d\Gamma\,, \tag{B.9}$$

$$\delta_p J = \int_\Omega \delta_p j_\Omega d\Omega + \int_\Gamma \delta_p j_\Gamma d\Gamma\,, \tag{B.10}$$

where j_Ω and j_Γ denote the cost functional integrands on the domain Ω and on the boundary Γ, respectively.
Elaboration on the terms of the boundary conditions (4.12) involving the symmetric rate-of-strain tensor, yields

$$\begin{aligned}&\oint_\Gamma \left(\delta u_j 2\mu_e \hat{S}_{ij} n_i - \hat{u}_j \mu_e \left(\frac{\partial \delta u_i}{\partial x_j}+\frac{\partial \delta u_j}{\partial x_i}\right) n_i\right) d\Gamma \\ &= \oint_\Gamma \mu_e n_i \left(\frac{\partial \hat{u}_j}{\partial x_i}\delta u_j - \frac{\partial \delta u_j}{\partial x_i}\hat{u}_j\right) d\Gamma + \oint_\Gamma \mu_e n_i \left(\frac{\partial \hat{u}_i}{\partial x_j}\delta u_j - \frac{\partial \delta u_i}{\partial x_j}\hat{u}_j\right) d\Gamma\,.\end{aligned} \tag{B.11}$$

For divergence-less fields δu_i and $\hat{u}_i$ and under the assumption $\nabla \mu_e = 0$, integration by parts for the second integral leads to

$$\begin{aligned}
&\oint_\Gamma \mu_e n_i \left(\frac{\partial \hat{u}_i}{\partial x_j} \delta u_j - \frac{\partial \delta u_i}{\partial x_j} \hat{u}_j \right) d\Gamma \\
&= \oint_\Gamma \mu_e \left(\delta u_j \frac{\partial \hat{u}_n}{\partial x_j} \right) d\Gamma - \oint_\Gamma \mu_e \left(\frac{\partial \delta u_n}{\partial x_j} \hat{u}_j \right) d\Gamma \\
&= \left[\mu_e \delta u_j \hat{u}_n n_j \right]_\Gamma - \oint_\Gamma \mu_e \hat{u}_n \underbrace{\frac{\partial \delta u_j}{\partial x_j}}_{=0} d\Gamma - \left[\mu_e \delta u_n \hat{u}_j n_j \right]_\Gamma + \oint_\Gamma \mu_e \delta u_n \underbrace{\frac{\partial \hat{u}_j}{\partial x_j}}_{=0} d\Gamma \\
&= \left[\mu_e \delta u_n \hat{u}_n \right]_\Gamma - \left[\mu_e \delta u_n \hat{u}_n \right]_\Gamma d\Gamma = 0 \,.
\end{aligned} \tag{B.12}$$

Therefore, it holds for the terms of the boundary conditions (4.13), involving the symmetric rate-of-strain tensor

$$\oint_\Gamma \left(\delta u_j 2 \mu_e \hat{S}_{ij} n_i - \hat{u}_j \mu_e \left(\frac{\partial \delta u_i}{\partial x_j} + \frac{\partial \delta u_j}{\partial x_i} \right) n_i \right) d\Gamma = \oint_\Gamma \mu_e n_i \left(\frac{\partial \hat{u}_j}{\partial x_i} \delta u_j - \frac{\partial \delta u_j}{\partial x_i} \hat{u}_j \right) d\Gamma \,. \tag{B.13}$$

B.2. Adjoint RANS-F Equations

The variation of the last term of Equation (4.61) results in

$$- \int_\Omega \hat{u}_i \delta \left(\rho_{ref} \cdot (1 - \beta_T (T - T_{ref})) \cdot g_i \right) d\Omega = \int_\Omega \hat{u}_i \cdot \rho_{ref} \cdot \beta_T \cdot \delta T \cdot g_i \; d\Omega \,, \tag{B.14}$$

including a local variation of the temperature. The variation of the residual internal energy equation (4.63) leads to

$$\int_\Omega \hat{T} \delta H d\Omega = \int_\Omega \hat{T} \left[\delta \left(\rho \frac{\partial}{\partial x_j} (u_j T) \right) - \delta \left(\frac{\partial}{\partial x_j} \left[\kappa_e \frac{\partial T}{\partial x_j} \right] \right) - \delta \left(\frac{2 \mu_e}{c_v} S_{ij} \frac{\partial u_i}{\partial x_j} \right) \right] d\Omega \,. \tag{B.15}$$

For the first term of (B.15) holds

$$\begin{aligned}
\int_\Omega \hat{T} \delta \left(\rho \frac{\partial}{\partial x_j} (u_j T) \right) d\Omega &= \int_\Omega \left(\hat{T} \rho \delta u_j \frac{\partial T}{\partial x_j} + \hat{T} \rho u_j \frac{\partial \delta T}{\partial x_j} \right) d\Omega \\
&= \int_\Omega \hat{T} \rho \delta u_j \frac{\partial T}{\partial x_j} d\Omega + \oint_\Gamma \hat{T} \rho u_j \delta T n_j d\Gamma - \int_\Omega \rho u_j \delta T \frac{\partial \hat{T}}{\partial x_j} d\Omega \,.
\end{aligned} \tag{B.16}$$

Note that the first term includes the local variation of the velocity and, accordingly, contributes to the velocity equation. For the second term of (B.15) integration by parts yields

$$-\int_\Omega \hat{T}\delta\left(\frac{\partial}{\partial x_j}\left[\kappa_e\frac{\partial T}{\partial x_j}\right]\right)d\Omega = -\int_\Omega \delta T\frac{\partial}{\partial x_j}\left[\kappa_e\frac{\partial \hat{T}}{\partial x_j}\right]d\Omega - \oint_\Gamma \kappa_e\left(\hat{T}\frac{\partial \delta T}{\partial x_j} - \delta T\frac{\partial \hat{T}}{\partial x_j}\right)n_j d\Gamma\,. \tag{B.17}$$

Again, the frozen turbulence has been used, i.e. $\delta\kappa_e = 0$. Elaboration on the third term of (B.15) results in

$$\begin{aligned}
&-\int_\Omega \hat{T}\delta\left(\frac{2\mu_e}{c_v}S_{ij}\frac{\partial u_i}{\partial x_j}\right)d\Omega \\
&= -\frac{\mu_e}{c_v}\int_\Omega \hat{T}\left(\frac{\partial u_i}{\partial x_j}\frac{\partial \delta u_i}{\partial x_j} + \frac{\partial u_j}{\partial x_i}\frac{\partial \delta u_i}{\partial x_j} + \frac{\partial u_i}{\partial x_j}\frac{\partial \delta u_i}{\partial x_j} + \frac{\partial u_i}{\partial x_j}\frac{\partial \delta u_j}{\partial x_i}\right)d\Omega \\
&= -\frac{2\mu_e}{c_v}\int_\Omega \hat{T}\left(\frac{\partial u_i}{\partial x_j}\frac{\partial \delta u_i}{\partial x_j} + \frac{\partial u_j}{\partial x_i}\frac{\partial \delta u_i}{\partial x_j}\right)d\Omega\,.
\end{aligned} \tag{B.18}$$

For the first term of (B.18) it holds

$$\begin{aligned}
&-\frac{2\mu_e}{c_v}\int_\Omega \hat{T}\frac{\partial u_i}{\partial x_j}\frac{\partial \delta u_i}{\partial x_j}d\Omega \\
&= -\oint_\Gamma \frac{2\mu_e}{c_v}\hat{T}\frac{\partial u_i}{\partial x_j}\delta u_i\, n_j d\Gamma + \int_\Omega \frac{2\mu_e}{c_v}\frac{\partial}{\partial x_j}\left(\hat{T}\frac{\partial u_i}{\partial x_j}\right)\delta u_i d\Omega\,.
\end{aligned} \tag{B.19}$$

For the second term of (B.18), accordingly

$$\begin{aligned}
&-\frac{2\mu_e}{c_v}\int_\Omega \hat{T}\frac{\partial u_j}{\partial x_i}\frac{\partial \delta u_i}{\partial x_j}d\Omega \\
&= -\oint_\Gamma \frac{2\mu_e}{c_v}\hat{T}\frac{\partial u_j}{\partial x_i}\delta u_i n_j d\Gamma + \int_\Omega \frac{2\mu_e}{c_v}\frac{\partial}{\partial x_j}\left(\hat{T}\frac{\partial u_j}{\partial x_i}\right)\delta u_i d\Omega\,.
\end{aligned} \tag{B.20}$$

Finally, the third term of (B.15) transforms to

$$\begin{aligned}
&-\int_\Omega \hat{T}\delta\left(\frac{2\mu_e}{c_v}S_{ij}\frac{\partial u_i}{\partial x_j}\right)d\Omega \\
&= -\oint_\Gamma \frac{2\mu_e}{c_v}\hat{T}\left(\frac{\partial u_i}{\partial x_j} + \frac{\partial u_j}{\partial x_i}\right)\delta u_i n_j d\Gamma + \int_\Omega \frac{2\mu_e}{c_v}\frac{\partial}{\partial x_j}\left[\hat{T}\left(\frac{\partial u_i}{\partial x_j} + \frac{\partial u_j}{\partial x_i}\right)\right]\delta u_i d\Omega\,.
\end{aligned} \tag{B.21}$$

Bibliography

[1] H. W. Alt. *Lineare Funktionalanalysis.* Springer, 6th edition, 2012.

[2] L. Armijo. Minimization of functions having Lipschitz continuous first partial derivatives. *Pacific Journal of Mathematics*, 16(1):1–3, November 1966.

[3] M. P. Bendsøe and O. Sigmund. *Topology optimization: Theory, Methods and Applications.* Springer, 2nd edition, 2004.

[4] BETA CAE Systems. *ANSA v.13.2.1 User's Guide*, 2011.

[5] T. Borrvall and J. Petersson. Topology optimization using regularized intermediate density control. *Computer Methods in Applied Mechanics and Engineering*, 190(37–38):4911–4928, June 2001.

[6] T. Borrvall and J. Petersson. Topology optimization of fluids in Stokes flow. *International Journal for Numerical Methods in Fluids*, 41(1):77–107, January 2003.

[7] J. Boussinesq. *Essai sur la théorie des eaux courantes.* Imprimerie Nationale, 1877.

[8] S. Boyd and L. Vandenberghe. *Convex Optimization.* Cambridge University Press, 7th edition, 2009.

[9] J. Brezillon and R. P. Dwight. Effect of Approximations of the Discrete Adjoint on Gradient-Based Optimization. *American Institute of Aeronautics and Astronautics Journal*, 44(12):3022–3031, December 2006.

[10] A. E. Bryson and Y.-C. Ho. *Applied Optimal Control: Optimization Estimation and Control.* Routledge, revised edition, 1975.

[11] A. Carnarius, F. Thiele, E. Özkaya, and N. R. Gauger. Adjoint Approaches For Optimal Flow Control. In *AIAA 2010-5088, 5th AIAA Flow Control Conference*, Chicago, USA, July 2010.

[12] A. Carnarius, F. Thiele, E. Özkaya, A. Nemili, and N. R. Gauger. Optimal Control of Unsteady Flows Using a Discrete and a Continuous Adjoint Approach. *System Modeling and Optimization. CSMO 2011. IFIP Advances in Information and Communication Technology*, 391:318–327, 2013.

[13] H. Darcy. *Les Fontaines Publiques de La Ville de Dijon.* 1856.

[14] E. de Villiers and C. Othmer. Multi-Objective Adjoint Optimization of Intake Port Geometry. In *SAE 2012 World Congress & Exhibition*, Detroit, USA, April 2012.

[15] FeatFlow, Technische Universität Dortmund, Angewandte Mathematik und Numerik. *DFG flow around cylinder benchmark 2D-1, laminar case Re=20,* `http://www.featflow.de/en/benchmarks/cfdbenchmarking/flow/dfg_benchmark1_re20.html`, 2007 (accessed November 24, 2017).

[16] J. H. Ferziger and M. Perić. *Computational Methods for Fluid Dynamics.* Springer, 3rd edition, 2002.

[17] E. Furbo. Evaluation of RANS turbulence models for flow problems with significant impact of boundary layers. Examensarbete, Uppsala Universitet, 2010.

[18] A. Gerdes, M. Hinze, and T. Rung. An efficient line search technique and its application to adjoint topology optimisation. *Proceedings in Applied Mathematics and Mechanics*, 14(1):719–720, December 2014.

[19] A. Gerdes, M. Hinze, and T. Rung. Enhancement of adjoint topology optimization by approximated L^1-regularization for promotion of sparse distributed control. *Proceedings in Applied Mathematics and Mechanics*, 16(1):637–638, October 2016.

[20] R. Giering and T. Kaminski. Recipes for Adjoint Code Construction. *ACM Transactions on Mathematical Software*, 24(4):437–474, December 1998.

[21] M. B. Giles, M. C. Duta, J.-D. Müller, and N. A. Pierce. Algorithm Development for Discrete Adjoint Methods. *American Institute of Aeronautics and Astronautics Journal*, 41(2):198–205, February 2003.

[22] M. B. Giles and N. A. Pierce. An Introduction to the Adjoint Approach to Design. *Flow, Turbulence and Combustion*, 65(3–4):393–415, December 2000.

[23] C. J. Greenshields. *OpenFOAM, The Open Source CFD Toolbox, Programmer's Guide, Version 3.0.1.* CFD Direct Ltd, 2015.

[24] A. Griewank and A. Walther. Algorithm 799: Revolve: An Implementation of Checkpointing for the Reverse or Adjoint Mode of Computational Differentiation. *ACM Transactions on Mathematical Software*, 26(1):19–45, March 2000.

[25] A. Griewank and A. Walther. *Evaluating Derivatives: Principles and Techniques of Algorithmic Differentiation.* Society for Industrial and Applied Mathematics, 2nd edition, 2008.

[26] S. Günther, N. R. Gauger, and Q. Wang. Simultaneous single-step one-shot optimization with unsteady PDEs. *Journal of Computational and Applied Mathematics*, 294:12–22, March 2016.

[27] E. Helgason. *Development of adjoint-based optimization methods for ducted flows in vehicles.* PhD thesis, Chalmers University of Technology, 2015.

[28] J. P. Heners. Entwicklung und Validierung adjungierter logarithmischer Wandgesetze für Impulsgrenzschichten. B.S. thesis, Technische Universität Hamburg-Harburg, 2012.

[29] J. P. Heners. Implementierung und Validierung des Laplace-Beltrami-Operators in OpenFOAM. Projektarbeit, Universität Hamburg, 2013.

[30] H. Herwig. *Strömungsmechanik A–Z.* Vieweg+Teubner Verlag, 2004.

[31] M. Hinze. *Optimal and instantaneous control of the instationary Navier-Stokes equations.* Habilitation thesis, Technische Universität Dresden, 2002.

[32] M. Hinze, R. Pinnau, M. Ulbrich, and S. Ulbrich. Optimization with PDE Constraints. *Mathematical Modelling: Theory and Applications,* Volume 23, 2009.

[33] H. S. Holdgrün. *Analysis I: Differential- und Integralrechnung einer Variablen.* Leins Verlag, 1998.

[34] J. Huber. Robust estimation of a location parameter. *The Annals of Mathematical Statistics*, 35(1):73–101, March 1964.

[35] I. E. Idelchik. *Handbook of Hydraulic Resistance.* Jaico Publishing House, 3rd edition, 2005.

[36] R. I. Issa. Solution of the implicitly discretized fluid flow equations by operator-splitting. *Journal of Computational Physics*, 62(1):40–65, January 1986.

[37] D. Jakubek, S. Herzog, and C. Wagner. Adjoint-based shape optimization of high-speed trains. In *4th International Conference of Engineering Optimization*, Lisbon, Portugal, September 2014.

[38] D. Jakubek and C. Wagner. Shape Optimization of Train Head Cars using Adjoint-based Computational Fluid Dynamics. *International Journal of Railway Technology*, 1(2):67–88, 2013.

[39] A. Jameson. Aerodynamic Design via Control Theory. *Journal of Scientific Computing*, 3(3):1–17, September 1988.

[40] A. Jameson. Advances in Aerodynamic Shape Optimization. In *Computational Fluid Dynamics 2004, Proceedings of the Third International Conference on Computational Fluid Dynamics*, pages 687–698, Toronto, Canada, July 2004.

[41] A. Jameson and S. Kim. Reduction of the Adjoint Gradient Formula in the Continuous Limit. In *AIAA 2003-40, 41st AIAA Aerospace Sciences Meeting and Exhibit*, Reno, USA, January 2003.

[42] A. Jameson and S. K. Nadarajah. A Comparison of the Continuous and Discrete Adjoint Approach to Automatic Aerodynamic Optimization. In *AIAA-2000-0667, 38th AIAA Aerospace Sciences Meeting and Exhibit*, Reno, USA, January 2000.

[43] A. Jameson and S. K. Nadarajah. Studies of the Continuous and Discrete Adjoint Approaches to Viscous Automatic Aerodynamic Shape Optimization. In *AIAA-2001-2530, 15th AIAA Computational Fluid Dynamics Conference*, Anaheim, USA, June 2001.

[44] A. Jameson, N. A. Pierce, and L. Martinelli. Optimum aerodynamic design using the Navier-Stokes equations. In *AIAA 97-0101, 35th AIAA Aerospace Sciences Meeting and Exhibit*, Reno, USA, January 1997.

[45] H. Jasak. *Error Analysis and Estimation for the Finite Volume Method with Applications to Fluid Flows.* PhD thesis, Imperial College London, 1996.

[46] J. Kröger and T. Rung. CAD-free hydrodynamic optimisation using consistent kernel-based sensitivity filtering. *Ship Technology Research*, 62(3):111–130, 2015.

[47] B. E. Launder and D. B. Spalding. The numerical computation of turbulent flows. *Computer Methods in Applied Mechanics and Engineering*, 3(2):269–289, March 1974.

[48] A. Lincke, G. Lauenroth, T. Rung, and C. Wagner. Fluid-Dynamic Optimization of the Cabin Air Outlet Do728-KLA with Adjoint Sensitivity Analysis. *New Results in Numerical and Experimental Fluid Mechanics IX, Notes on Numerical Fluid Mechanics and Multidisciplinary Design*, 124:75–82, January 2014.

[49] A. Lincke and T. Rung. Adjoint-Based Sensitivity Analysis for Buoyancy-Driven Incompressible Navier-Stokes Equations with Heat Transfer. In *Proceedings of the Eighth International Conference on Engineering Computational Technology,* Paper 100, Dubrovnik, Croatia, September 2012.

[50] A. Lincke, A. Stück, and T. Rung. Derivation of an adjoint high-Reynolds number model for thermally driven flows. *Proceedings in Applied Mathematics and Mechanics*, 12(1):681–682, December 2012.

[51] J. Lions. *Optimal Control of Systems Governed by Partial Differential Equations.* Springer, 1971.

[52] G. Liu, M. Geier, Z. Liu, M. Krafczyk, and T. Chen. Discrete adjoint sensitivity analysis for fluid flow topology optimization based on the generalized lattice Boltzmann method. *Computers & Mathematics with Applications*, 68(10):1374–1392, November 2014.

[53] X. Luo. Identifikation von Wärmequellen in konvektiv getriebenen Strömungen. Diplomarbeit, Universität Hamburg, 2011.

[54] R. K. Martin. *Large Scale Linear and Integer Optimization: A Unified Approach.* Springer, 1999.

[55] A. Meister. *Numerik linearer Gleichungssysteme.* Vieweg+Teubner Verlag, 3rd edition, 2008.

[56] F. R. Menter and T. Esch. Elements of Industrial Heat Transfer Predictions. In *16th Brazilian Congress of Mechanical Engineering, Proceedings of COBEM 2001, Invited Lectures*, volume 20, pages 117–127, 2001.

[57] K. Morimoto, Y. Suzuki, and N. Kasagi. Adjoint Analysis of Heat and Fluid Flow Toward Optimal Shape Design of Recuperators. *Thermal Science & Engineering*, 13(4), July 2005.

[58] G. Nabh. *On High Order Methods for the Stationary Incompressible Navier-Stokes Equations.* Interdisziplinäres Zentrum für Wissenschaftliches Rechnen der Universität Heidelberg, SFB 359, Reaktive Strömungen, Diffusion und Transport. IWR, 1998.

[59] P. Naphon and J. Suwagrai. Effect of curvature ratios on the heat transfer and flow developments in the horizontal spirally coiled tubes. *International Journal of Heat and Mass Transfer*, 50(3–4):444–451, February 2007.

[60] C. Othmer. A continuous adjoint formulation for the computation of topological and surface sensitivities of ducted flows. *International Journal for Numerical Methods in Fluids*, 58(8):861–877, March 2008.

[61] C. Othmer, T. Kaminski, and R. Giering. Computation of topological sensitivities in fluid dynamics: Cost function versatility. In *ECCOMAS CFD 2006: Proceedings of the European Conference on Computational Fluid Dynamics*, Egmond aan Zee, The Netherlands, January 2006.

[62] C. Othmer, E. M. Papoutsis-Kiachagias, and K. Haliskos. CFD optimization via sensitivity-based shape morphing. In *4th ANSA & μETA International Conference*, Thessaloniki, Greece, June 2011.

[63] E. M. Papoutsis-Kiachagias, E. A. Kontoleontos, A. S. Zymaris, D. I. Papadimitriou, and K. C. Giannakoglou. Constrained topology optimization for laminar and turbulent flows, including heat transfer. In *Evolutionary and Deterministic Methods for Design, Optimization and Control*, Capua, Italy, 2011.

[64] S. V. Patankar. *Numerical Heat Transfer and Fluid Flow.* Taylor & Francis, 1980.

[65] S. V. Patankar and D. B. Spalding. A calculation procedure for heat, mass and momentum transfer in three-dimensional parabolic flows. *International Journal of Heat and Mass Transfer*, 15(10):1787–1806, October 1972.

[66] O. Pironneau. On optimum profiles in Stokes flow. *Journal of Fluid Mechanics*, 59(1):117–128, June 1973.

[67] S. B. Pope. *Turbulent Flows*. Cambridge University Press, 2000.

[68] M. Raffel, C. Willert, S. Wereley, and J. Kompenhans. *Particle Image Velocimetry*. Springer, 2nd edition, 2007.

[69] L. I. Rudin, S. Osher, and E. Fatemi. Nonlinear total variation based noise removal algorithms. *Physica D: Nonlinear Phenomena*, 60(1–4):259–268, November 1992.

[70] T. Rung. Statistische Turbulenzmodellierung. Hermann-Föttinger-Institut für Strömungsmechanik, Technische Universität Berlin, 2001.

[71] T. Rung. Skriptum zur Vorlesung Numerische Methoden der Thermofluiddynamik 2 (CFD2), Grundlagen der Finite-Volumen Approximation. Technische Universität Hamburg-Harburg, Institut für Fluiddynamik und Schiffstheorie, October 2008.

[72] M. Schäfer, S. Turek, F. Durst, E. Krause, and R. Rannacher. Benchmark Computations of Laminar Flow Around a Cylinder. *Flow Simulation with High-Performance Computers II, Notes on Numerical Fluid Mechanics*, 48:547–566, 1996.

[73] S. Schmidt, C. Ilic, N. Gauger, and V. Schulz. Shape Gradients and their Smoothness for Practical Aerodynamic Design Optimization. Preprint-Number SPP1253-10-03, April 2008.

[74] O. Soto and R. Löhner. On the Computation of Flow Sensitivities From Boundary Integrals. In *AIAA-2004-0112, 42nd AIAA Aerospace Sciences Meeting and Exhibit*, Reno, USA, January 2004.

[75] J. Springer. Vergleichende Analyse numerischer Methoden zur Lösung der inkompressiblen Navier-Stokes Gleichungen in OpenFOAM, Comet und FreSCo. Diplomarbeit, Universität Ulm, 2009.

[76] G. Stadler. Elliptic optimal control problems with L^1-control cost and applications for the placement of control devices. *Computational Optimization and Applications*, 44:159–181, November 2009.

[77] E. Stavropoulou, M. Hojjat, and K.-U. Bletzinger. In-plane mesh regularization for node-based shape optimization problems. *Computer Methods in Applied Mechanics and Engineering*, 275:39–54, June 2014.

[78] A. Stück. *Adjoint Navier-Stokes Methods for Hydrodynamic Shape Optimisation*. PhD thesis, Technische Universität Hamburg-Harburg, 2011.

[79] A. Stück, J. Kröger, and T. Rung. Adjoint-based Hull Design for Wake Optimisation. *Ship Technology Research*, 58(1):34–44, January 2015.

[80] A. Stück and T. Rung. Adjoint RANS with filtered shape derivatives for hydrodynamic optimisation. *Computers & Fluids*, 47(1):22–32, August 2011.

[81] A. Stück and T. Rung. Filtered Gradients for Adjoint-based Shape Optimisation. In *AIAA 2011-3072, 20th American Institute of Aeronautics and Astronautics Computational Fluid Dynamics Conference*, Honolulu, USA, June 2011.

[82] A. Stück and T. Rung. Adjoint complement to viscous finite-volume pressure-correction methods. *Journal of Computational Physics*, 248:402–419, September 2013.

[83] H. J. Sussmann and J. C. Willems. 300 Years of Optimal Control: From the Brachystochrone to the Maximum Principle. *IEEE control systems*, 17(3):32–44, July 1997.

[84] S. Ta'asan. One Shot Methods for Optimal Control of Distributed Parameter Systems I: Finite Dimensional Control. *NASA Contractor Report 187497, ICASE Report No. 91-2*, January 1991.

[85] M. Ulbrich and S. Ulbrich. *Nichtlineare Optimierung.* Birkhäuser, 2012.

[86] H. Veelken. Direct integration of continuous sensitivity distributions in the shape optimization process. Diplomarbeit, Universität Hamburg, 2011.

[87] S. Ziegenbalg. *Kontrolle freier Ränder bei der Erstarrung von Kristallschmelzen.* PhD thesis, Technische Universität Dresden, 2008.

[88] A. S. Zymaris, D. I. Papadimitriou, K. C. Giannakoglou, and C. Othmer. Continuous adjoint approach to the Spalart-Allmaras turbulence model for incompressible flows. *Computers & Fluids*, 38(8):1528–1538, September 2009.